

博士論文

**Development and Characterization of  
Ruthenium Based Anodes for  
Direct Methane Low Temperature  
Thin Film Solid Oxide Fuel Cells**

(メタン直接改質低温薄膜固体酸化物形燃料電池の  
ルテニウム系燃料極開発とその特性評価)

**Yuto Takagi**

高木 裕登



## CONTENTS

<b>Chapter 1: Introduction</b>	<b>1</b>
1.1 <i>Introduction to Solid Oxide Fuel Cells</i>	1
1.2 <i>Direct Hydrocarbon Operation of Solid Oxide Fuel Cells</i>	5
1.3 <i>Introduction to Thin Film Micro-Solid Oxide Fuel Cells</i>	11
1.4 <i>Composite Anodes for Solid Oxide Fuel Cells</i>	19
1.5 <i>The Aim of this Work</i>	22
<b>Chapter 2: Fabrication Processes of Micro-Solid Oxide Fuel Cells</b>	<b>27</b>
2.1 <i>Introduction to Micro-Solid Oxide Fuel Cell Fabrication</i>	27
2.2 <i>Fabrication Processes of Micro-Solid Oxide Fuel Cell Platform</i>	30
2.3 <i>Critical Processes in Scope of Applying Ruthenium Based Anodes on Micro-Solid Oxide Fuel Cells</i>	34
2.4 <i>Performance Measurement of the Fuel Cells</i>	37
<b>Chapter 3: Thermal-Electrochemical Multi-Physics Simulation on Micro-Solid Oxide Fuel Cells</b>	<b>41</b>
3.1 <i>Introduction</i>	41
3.2 <i>Model Structure</i>	41
3.3 <i>Results and Discussion</i>	49
3.4 <i>Conclusions</i>	58

<b>Chapter 4: Characterization of Nano-Porous Ruthenium Thin Films for</b>	
<b>Micro-Solid Oxide Fuel Cell Anodes</b>	<b>61</b>
4.1 Introduction	61
4.2 Experimental Details	61
4.3 Results and Discussion	63
4.4 Conclusions	82
<b>Chapter 5: Micro-Solid Oxide Fuel Cells with Nano-Porous Ruthenium</b>	
<b>Anodes for Direct Methane Operation</b>	<b>82</b>
5.1 Introduction	83
5.2 Experimental Details	83
5.3 Results and Discussion	85
5.4 Conclusions	128
<b>Chapter 6: Characterization of Ruthenium – Gadolinia-Doped Ceria</b>	
<b>Nano-Composite Thin Films for Micro-Solid Oxide Fuel Cell Anodes</b>	<b>129</b>
6.1 Introduction	129
6.2 Experimental Details	129
6.3 Results and Discussion	133
6.4 Conclusions	151

<b>Chapter 7: Micro-Solid Oxide Fuel Cells with Ruthenium – Gadolinia-Doped Ceria Nano-Composite Anodes</b>	<b>153</b>
7.1 <i>Introduction</i>	153
7.2 <i>Experimental Details</i>	153
7.3 <i>Results and Discussion</i>	154
7.4 <i>Conclusions</i>	171
<b>Chapter 8: Conclusions</b>	<b>173</b>
<b>References</b>	<b>183</b>
<b>Acknowledgements</b>	<b>196</b>



# **Chapter 1: Introduction**

## **1.1 Introduction to Solid Oxide Fuel Cells**

### **1.1.1 Solid oxide fuel cell as a clean energy device**

Solid oxide fuel cells (SOFCs) are known for their high power densities and conversion efficiencies, and their development is an area of great technological interest [1-4]. SOFCs have a particularly wide range of applications ranging from centralized megawatt scale power plants through to local domestic generations on the 1 kW scale. There are even some SOFC ‘palm-power’ applications being considered in the 10 W range. Fuel cells are not subject to the Carnot-cycle limitations, and unlike gas-turbines, exhibit their highest efficiencies at low loads. One of the limitations of current fuel cell technologies is the requirement that the fuel should be hydrogen. The linking of fuel cells as an energy conversion device and hydrogen as an energy carrier has emphasized investment in polymer electrolyte membrane fuel cells (PEMFCs) as a part of a larger ‘hydrogen economy’. PEMFCs have an advantage of being able to operate from room temperature, but essentially only accept hydrogen as the fuel. The introduction of ‘hydrogen economy’ might seem an attractive scenario for low environmental impact society, however, its implementation is beset with formidable technical and economic difficulties. Unless there is a breakthrough in production, transportation and storage of hydrogen, this concept will remain an unlikely scenario. Despite the fact that the best performance of fuel cells is often achieved when running on hydrogen, practical applications may likely require utilization of more readily available hydrocarbon fuels such as methane or propane, to ensure that the technology is able to penetrate the relevant major markets [5-8]. In contrast to PEMFCs, SOFCs can in principle oxidize any fuel from hydrogen to even carbon because oxygen ions are transported through the electrolyte from the cathode to the anode compartment. The fuel processing reaction can be accomplished within the stack, which

enables innovative thermal integration design features to provide high system efficiencies. As such, SOFCs offer a great promise as a clean process for directly converting chemical energy to electricity while providing significant environmental benefits. As a result of their high conversion efficiencies, the amount of CO<sub>2</sub> produced can be less than half per kWh compared to internal combustion engines. Moreover, SOFC operation on biofuels is the most energy efficient means to utilize local grown carbon neutral fuels. Methane is one of the most abundant hydrocarbon fuels being a major component in natural gas, and is also abundantly included in biogas and sewage gas [9].

### **1.1.2 Operating principles of solid oxide fuel cells and polymer electrolyte membrane fuel cells**

The operating principle of an SOFC running on methane is shown schematically in **Fig. 1.1 (a)**. For simplicity sake, full oxidation of methane is assumed which may not be the case in real operation conditions. SOFC consists of three major components; a cathode electrode, an anode electrode, and an oxygen ion (O<sup>2-</sup>) conducting solid electrolyte. Under operation, molecular oxygen is reduced to oxygen ions at the cathode using electrons supplied from an external circuit.



The electrolyte must be dense to separate fuel and air compartments of the cell, and retain its high ionic conductivity and low electronic conductivity over a wide range of oxygen partial pressures. Driven by the difference in oxygen chemical potential between fuel and air compartments of the cell, oxygen ions travel through the electrolyte to the anode where the fuel (in this case, methane) is oxidized yielding heat, water vapor, carbon dioxide and electrons.



At the present time, the most well established material for a SOFC anode is nickel - yttria-

stabilized-zirconia (Ni-YSZ) composites. Ni in these cermet anodes provides electronic conductivity and catalytic activity, while YSZ provides ionic conductivity to allow  $O^{2-}$  to diffuse into the anode and a structural support to prevent Ni sintering. Electrons released by this reaction flow through the external circuit to the cathode, producing electrical energy by means of external load and complete the overall reaction. Although full oxidation of methane is assumed in equation (1.2), it should be noted that direct electrochemical oxidation of methane is not likely to occur in one step [8, 10], where details will be discussed in subsection 1.2.1.

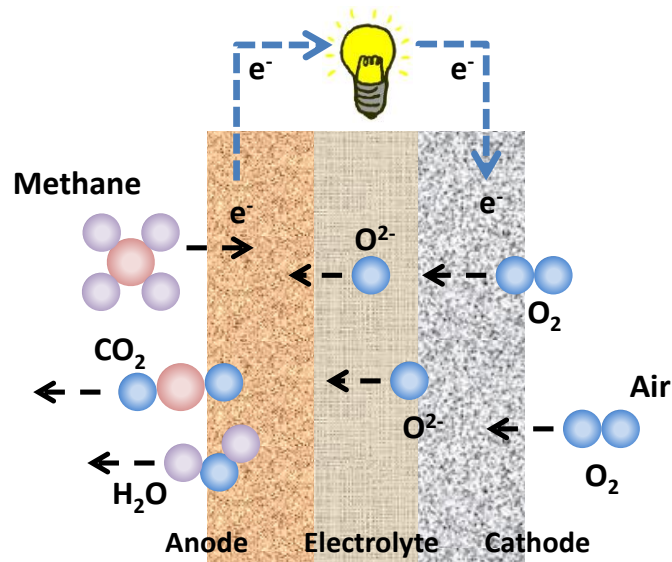
Operating principle of a PEMFC is shown schematically in **Fig. 1.1 (b)**. Instead of oxygen ions traveling from the cathode to the anode as in the case of SOFCs, protons travel from the anode to the cathode through proton conducting electrolytes. In order to maintain sufficient proton conductivity, the water content in the polymer electrolyte membrane needs to be carefully controlled by an appropriate ‘water management’ technology. Molecular hydrogen is oxidized to protons at the anode compartment releasing electrons to the external circuit.



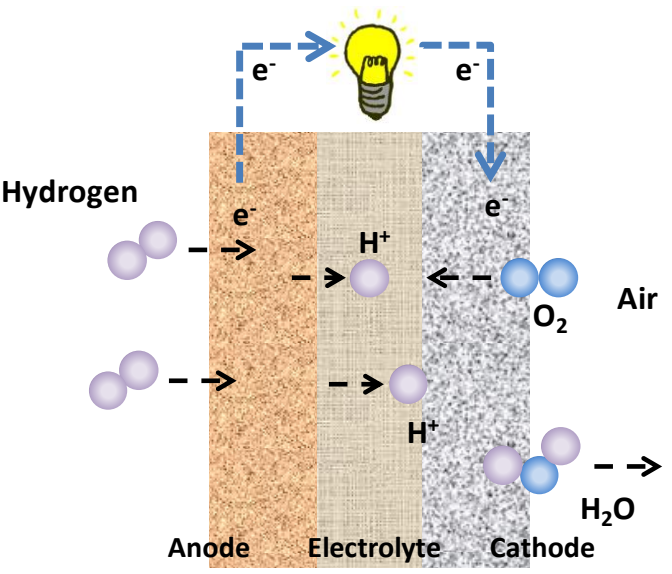
At the cathode, protons react with oxygen molecules from ambient air and electrons from the external circuit producing water.



Note that reaction products are formed at the cathode for PEMFCs, where they are formed at the anode for SOFCs. PEMFCs require relatively pure hydrogen with very low impurities (e.g. CO) to be supplied to the anode as the impurities may poison the precious metal catalysts and deteriorate the fuel cell performance. Thus, the use of hydrocarbon fuels requires an external fuel processor with an ability of extensive CO removal down to lower ppm level. Another drawback of low temperature PEMFCs is that they require extensive amount of platinum based catalysts for both anode and cathode electrodes.



(a)



(b)

**Fig. 1.1** Schematic of fuel cell operating principle, (a) SOFC operating on methane assuming full oxidation, and (b) PEMFC operating on hydrogen.

## 1.2 Direct Hydrocarbon Operation of Solid Oxide Fuel Cells

### 1.2.1 Alternative anodes for direct hydrocarbon operation

For high temperature SOFCs operated in 700~1000 °C range, partial external steam reforming is currently the most widely used approach to utilize hydrocarbons. Selected hydrocarbon fuels can be introduced directly into the SOFC anode compartment with steam for internal reforming, and can help to remove some of the heat generated by cell inefficiencies. However, due to the strong endothermic nature, internal steam reforming can also make it difficult to maximize the system performance because of cold spots in the cell, which in turn lead to lower performance of certain parts of the anode. This may also result in enhanced temperature gradients within cell compartments and cause undesirable internal stresses and related difficulties in the thermal management of the stack [11].

Direct hydrocarbon fueled SOFCs without pre-mixture of steam would eliminate the need of a reformer and a humidifier, and would substantially simplify system complexity and reduce overall cost (as shown in **Fig. 1.2**). At present, reformer, humidifier and related water management system is taking up a significant portion of the SOFC system volume and cost. The most critical issue for SOFC operating on hydrocarbon fuels without reforming is the need of anodes that do not catalyze carbon formation due to fuel cracking at operating temperatures [6, 12, 13]. Conventional Ni based anodes easily catalyzes carbon formation and do not appear to be suitable for direct hydrocarbon utilization. Several researchers have made progress on mitigating this issue while maintaining a reasonable performance of SOFCs, in recent years by using anodes alternative to conventional Ni-YSZ cermets [1-5, 8, 14-20]. For example, Park et al. [8] reported direct electrochemical oxidation of various hydrocarbons with copper-ceria composite anodes at 700~800 °C. At 700 °C, reasonable power density of 0.12 W cm<sup>-2</sup> was achieved with dry n-butane as the fuel. Gas chromatography analysis of the anode effluent showed that final products of the fuel oxidation were CO<sub>2</sub> and water, suggesting that n-butane

was completely oxidized through the anode reaction. Particularly methane-fueled SOFCs have received considerable attention in the scientific community due to its abundance and accessibility [3, 21-24]. Chen et al. [21] showed an open circuit voltage (OCV) of 0.8 V and a power density of 60 mW cm<sup>-2</sup> at 750 °C with 3 % humidified methane as fuel with a redox stable perovskite La<sub>0.75</sub>Sr<sub>0.25</sub>Cr<sub>0.5</sub>Mn<sub>0.5</sub>O<sub>3</sub> (LSCM) – gadolinia doped ceria (CGO) anode. The OCV increased to above 0.9 V at 850 °C, indicating that humidified methane is not reaching its equilibrium state on the LSCM-CGO anode at this temperature due to the low catalytic activity of the anode towards methane oxidation. Wang et al. [24] reported an OCV of 0.8 V and power density of 460 mW cm<sup>-2</sup> at 650 °C with Ru – samaria doped ceria (SDC) catalytic layer on top of Ni-SDC anode. Three % humidified methane was supplied as the fuel. It is likely that some methane was first oxidized to CO<sub>2</sub> and water under the electrocatalysis by the mesoporous SDC. Available additional methane was then internally reformed with the created water and CO<sub>2</sub> under the catalysis of Ru to form syngas (CO+H<sub>2</sub>), which acted as the fuel for the following electrocatalytic oxidation. This concept that reforming can still occur even with dry fuel sources is generally named gradual internal reforming, and is considered as an important mechanism towards direct utilization of hydrocarbons in SOFC anodes (as shown in **Fig. 1.3** from [25]). Hibino et al. [14] also demonstrated a direct methane-fueled SOFC with performance of 750 mW cm<sup>-2</sup> at 600 °C by utilizing Ni-CGO-Ru anodes. This peak power density was comparable to that of 769 mW cm<sup>-2</sup> with hydrogen fuel. The role of the Ru catalyst in the anode reaction was explained to promote the reforming reaction of unreacted hydrocarbons with produced steam and CO<sub>2</sub>, which avoids interference from steam and CO<sub>2</sub> in the gas phase diffusion of the fuels. **Table 1.1** summarizes some of the recent efforts on direct hydrocarbon operated SOFCs, including the works described above.

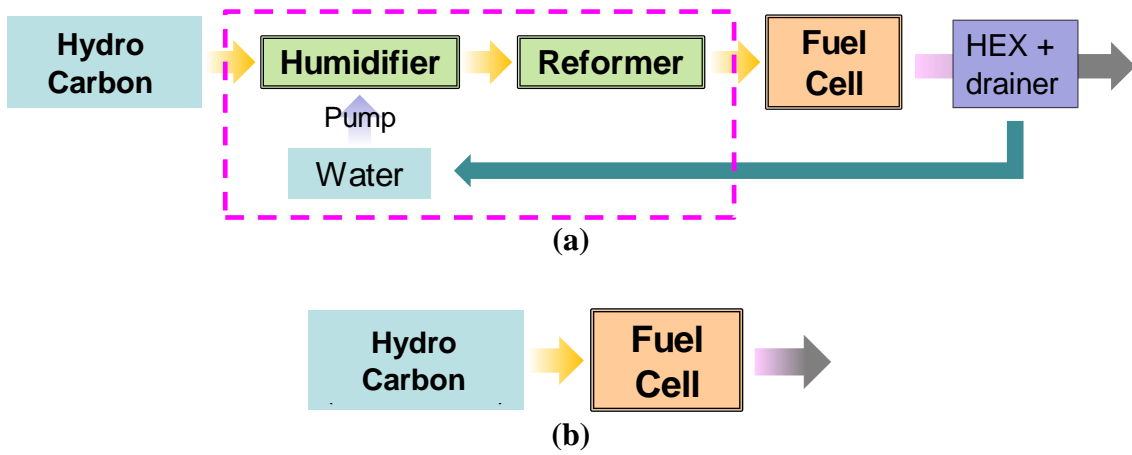


**Fig. 1.2** Schematic of SOFC system flow, (a) with an external reformer and related water management system, and (b) with direct hydrocarbon supply.

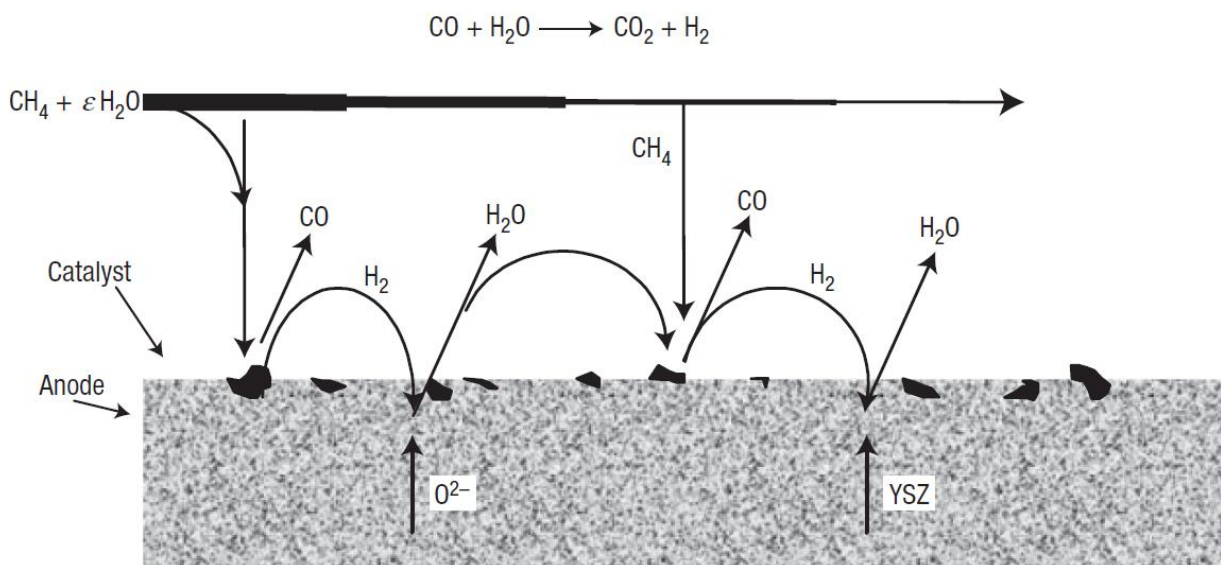


**Fig. 1.3** Schematic of the series of processes that lead to the gradual internal methane reforming, where relative humidity  $\epsilon$  is significantly less than 2 (from [25]).

**Table 1.1** Recent efforts on development of direct hydrocarbon operated SOFCs.

Year	2000	2003	2003	2007	2007	2011
Cell configuration	Planar	Planar	Planar	Planar	Planar	Tubular
Cell temperature °C	700	700	600	750	650	554
Power density $\text{mW cm}^{-2}$	120	280	750	60	460	450
Fuel	Dry n-butane	Dry $\text{CH}_4$	$\text{CH}_4 / 3\% \text{H}_2\text{O}$	$\text{CH}_4 / 3\% \text{H}_2\text{O}$	$\text{CH}_4 / 3\% \text{H}_2\text{O}$	Humidified $\text{CH}_4$ (S/C=4)
Anode composition	Cu-CeO <sub>2</sub> -YSZ	Pd + Cu-CeO <sub>2</sub> -YSZ	Ni-CGO-Ru	LSCM-CGO	Ru-SDC / Ni-SDC	Ni-CGO-CeO <sub>2</sub>
Authors	Park et al.[8]	McIntosh et al. [4]	Hibino et al. [3]	Chen et al. [21]	Wang et al. [24]	Suzuki et al. [16]

### 1.2.2 Ruthenium as an anode material for direct hydrocarbon utilization

In this work, Ru has been investigated as an anode catalyst for direct methane utilization. Other transition metals such as platinum (Pt), palladium (Pd) and Ni are also active for methane oxidation, however Ru is expected to have a better microstructural stability under SOFC operation conditions because of its high melting point compared to Pt, Pd and Ni (Ru: 2334 °C; Pt: 1768 °C; Pd: 1555 °C; Ni: 1455 °C). Moreover, Ru has been recognized as an excellent catalyst for wide range of hydrocarbon utilization, such as steam reforming [26-29], dry reforming with CO<sub>2</sub> [27, 30-32] and partial oxidation of methane [33-36], and has been utilized for direct hydrocarbon oxidation in SOFCs [3, 37-39]. Catalytic activity of Ru towards methane reforming is known to be active at temperatures as low as 300 °C [40]. **Figure 1.4** schematically provides possible reactions paths for methane oxidation over Ru based anodes in SOFCs that have been discussed in literature [3, 26, 27, 30, 32, 41]. One of the major reaction paths of methane oxidation on Ru based anodes is, **(a)** partial oxidation combined with reforming and electrochemical oxidation of the intermediates. Partial oxidation and steam or dry reforming of methane produces intermediate reactants such as H<sub>2</sub> and CO. These can be oxidized to generate H<sub>2</sub>O and CO<sub>2</sub> which further aids methane reforming. Within this scheme, the overall reaction cycles are locally coupled and accelerated [41]. Another possible reaction path is, **(b)** a process that involves C-H bond cracking followed by electrochemical oxidation of the products. However, Ru is known to be rather inactive to methane cracking compared to Pd, Ni and other known metal based catalysts [42]. Ru is especially active to dry and wet reforming of hydrocarbons and highly tolerant to carbon deposition [27] and thus, appears to be a promising anode material for direct hydrocarbon utilization in low temperature SOFCs.

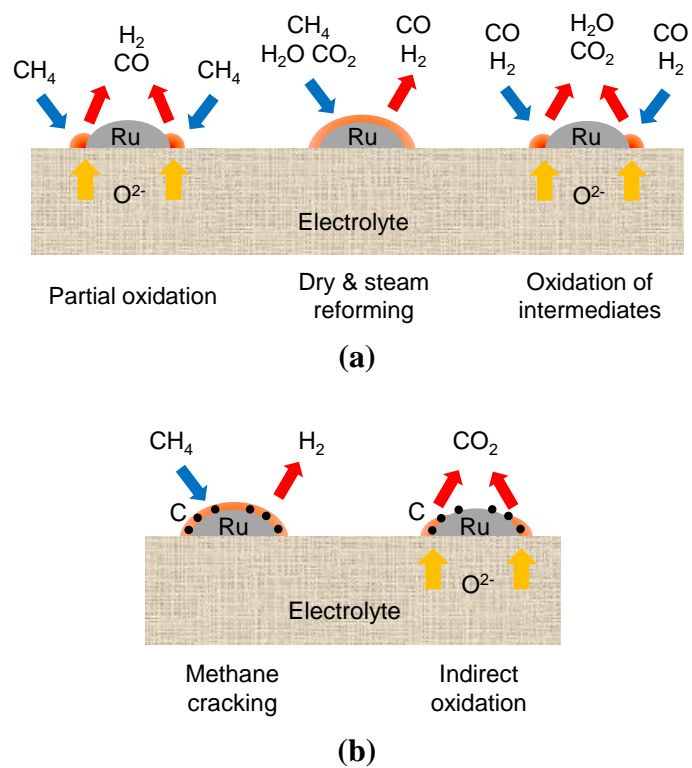


**Fig. 1.4** Possible reaction paths of methane over Ru anodes, **(a)** partial oxidation of methane, and dry and steam reforming followed by oxidation of intermediate reactants, and **(b)** methane cracking followed by indirect oxidation.

### 1.3 Introduction to Thin Film Micro-Solid Oxide Fuel Cells

#### 1.3.1 Lowering the operation temperature of solid oxide fuel cells

Current SOFC technology mostly requires operation in the temperature regime of  $\sim 800$  °C to avoid unacceptably high polarization losses. These high temperature demand specialized expensive materials for the fuel cell interconnects, seals and insulation resulting in higher system cost, as well as slow start-up and significant energy consumption to heat up to the operating temperature. These factors dramatically limit the applicability especially in portable power and transportation markets. Reducing fuel cell operation temperature to intermediate  $\sim$  low temperature range would allow a wider range of material choices, rapid start-ups and shutdowns, and reduced energy consumption at start-ups. Moreover, it has been pointed out that operation above 700 °C with hydrocarbon fuels potentially results in problematic carbon coking from thermodynamics stand point [23]. Decreasing the temperature may however result in a decrease of the performance, due to an increase in area-specific resistivity (ASR) of the cell. Besides the contribution of kinetic losses from the electrochemical reactions occurring at the anode and cathode electrodes, Ohmic losses related to oxygen ion transport through the electrolyte may become significant [43]. Improvement in fuel cell performance at low temperature regime can be achieved by multiple routes. In order to lower the Ohmic loss through the electrolyte, the thickness can be reduced down to tens of micrometers in electrode-supported cell configuration [18, 43-46]. If we assume that the electrolyte component should not contribute more than  $0.15 \Omega \text{ cm}^2$  to the total ASR, then the electrolyte thickness needs to be below 15  $\mu\text{m}$  at 700 °C with YSZ electrolytes (as shown in **Fig. 1.5** from [18]). The use of even thinner electrolytes would allow the operating temperature to be lowered furthermore, and with 1  $\mu\text{m}$  thick YSZ electrolytes the operation temperature can be lowered to 500 °C range. Another approach is to develop new electrolyte materials with higher ionic conductivity compared to conventional zirconia based electrolytes, in order to reduce Ohmic resistance with

similar electrolyte thicknesses. For example, Ishihara et al. [47, 48] have developed  $\text{LaGaO}_3$  based perovskite oxide ion conductor that shows almost an order higher conductivity compared to conventional YSZ. It is claimed that this electrolyte material ( $\text{La}_{0.9}\text{Sr}_{0.1}\text{Ga}_{1-x}\text{Mg}_x\text{O}_3$ ) is stable over a wide range of oxygen partial pressure, and exhibits oxide ion conductivity from  $p\text{O}_2 = 10^{-20}$  to 1 atm. Operation in fuel cell configuration has also been demonstrated showing promising power density of  $0.1 \text{ W cm}^{-2}$  at  $600 \text{ }^\circ\text{C}$ . Another interesting electrolyte material, doped bismuth oxides ( $\text{Bi}_2\text{O}_3$ ) are known for their high ionic conductivity but they have a problem of chemical instability under reducing condition where bismuth is reduced to its metal form [49]. In order to avoid this instability, Wachsman's group have demonstrated a bilayer structured electrolyte of erbium oxide doped  $\text{Bi}_2\text{O}_3$  and dense CGO, with a bismuth ruthenate –  $\text{Bi}_2\text{O}_3$  composite cathode and demonstrated peak power density of  $2 \text{ W cm}^{-2}$  at  $650 \text{ }^\circ\text{C}$  [50].

Besides the ASR from the electrolyte Ohmic resistance, non-ohmic electrode ASR can also be significant at intermediate to low temperatures [51]. With decreasing temperature, area specific electrode reaction rates decreases exponentially. In order to lower the electrode polarization losses, new materials with improved catalytic activity have been developed [7, 18, 43, 52], along with improving electrode microstructures which increases effective reaction area [5, 7, 18, 52, 53]. By shifting the effective dimension of the catalytic phase from micro ( $10^{-6}$ ) to nanometer ( $10^{-9}$ ) order, it would be possible to dramatically increase electrochemically active triple phase boundary (TPB) density and compensate for the reduced area specific electrode reaction rates [54]. Furthermore, by reducing the operation temperature these nanostructured electrodes gain stability against coarsening, which is a primary degradation mechanism for SOFC electrodes.

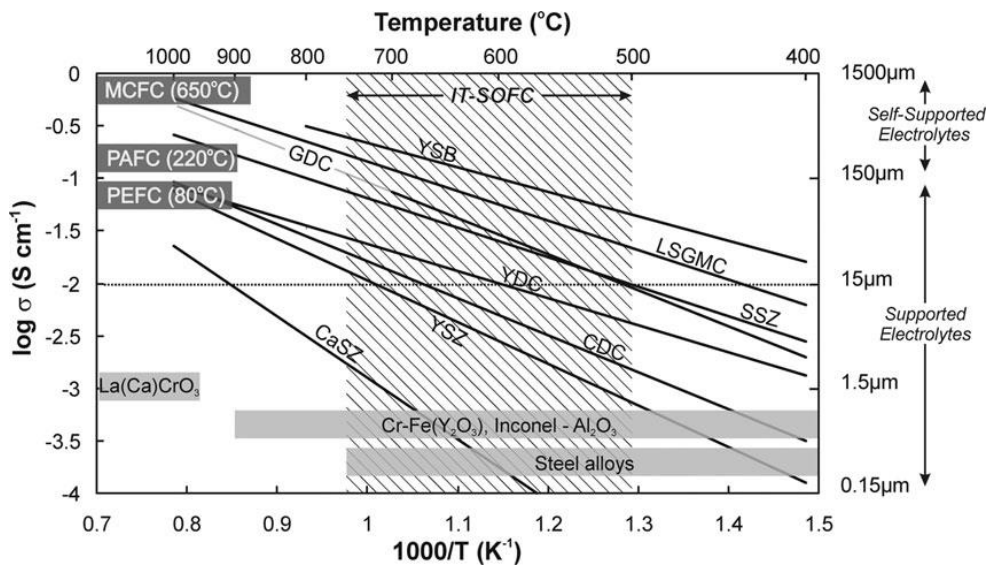


**Fig. 1.5** Specific ionic conductivity as a function of reciprocal temperature including conductivity of selected solid oxide fuel cell electrolytes and operational range of different interconnect materials [18].

### 1.3.2 Previous works on thin film micro-solid oxide fuel cells

Because direct conversion of chemical to electrical energy does not suffer from the Carnot efficiency restrictions of conventional thermal-mechanical energy production methods, in principle it is possible to scale down the size of the device without affecting the SOFC overall efficiency. A research effort at MIT showed the first example of using silicon processing technologies developed for microelectromechanical systems (MEMS) applied to the fabrication of self-supported SOFC electrolyte membranes [55]. As shown in the schematics in **Fig. 1.6**, the design is based on a conventional dual chamber configuration where a dense, self-supported electrolyte membrane separates the fuel and oxidant gases and also serves as a mechanical support for anode and cathode electrodes. The driving force of the electrochemical reaction is the oxygen partial pressure difference between the anode (low  $p_{O_2}$ ) and the cathode (high  $p_{O_2}$ ). Ultra-thin  $\mu$ SOFCs were fabricated at Stanford University using lithography and etching, made of a YSZ electrolyte film deposited by RF sputtering on a silicon wafer with porous Pt films both for anode and cathode prepared by DC sputtering [56]. The fuel cell power output using hydrogen as fuel with a 50 nm thick YSZ electrolyte was  $130 \text{ mW cm}^{-2}$  at  $350 \text{ }^\circ\text{C}$ . An addition of a supplementary CGO layer between the YSZ and cathode layers increased the power output to  $200 \text{ mW cm}^{-2}$  at  $350 \text{ }^\circ\text{C}$ . Further efforts in improving performance of  $\mu$ SOFCs have been given extensively over the past decade. For example, a group of Harvard University have demonstrated a peak power density of  $1.04 \text{ W cm}^{-2}$  and OCV of  $0.97 \text{ V}$  at  $500 \text{ }^\circ\text{C}$  by optimizing nano-porous Pt anode morphology in Pt/YSZ/Pt  $\mu$ SOFCs with 100 nm YSZ electrolyte [57]. Pt electrode thickness was optimized to maximize the TPB length, while YSZ electrolyte thickness was optimized to improve the fuel cell performance at elevated temperature. Su et al. [58] reported a maximum performance of  $861 \text{ mW cm}^{-2}$  and OCV of  $1.09 \text{ V}$  at  $450 \text{ }^\circ\text{C}$  by using 70 nm thick corrugated electrolyte membranes deposited by atomic layer deposition. The cell size was  $600 \text{ } \mu\text{m} \times 600 \text{ } \mu\text{m}$  with embedded cups of  $15 \text{ } \mu\text{m}$  diameter and 20

$\mu\text{m}$  depth, leading to 5-fold increase in the effective surface area.

Such small scale fuel cells also have relevance to applications in mobile energy and are emerging field of active research. The large energy densities of SOFCs and the versatility in fuel use, not limited to hydrogen, generates interest in the deployment of  $\mu\text{SOFCs}$  for mobile power generation in the lower 1~500 W range. Foreseeable applications include portable electronic devices (which are now powered by rechargeable batteries), vehicle power supplies, and auxiliary power units. **Figure 1.7** shows that  $\mu\text{SOFC}$  systems are predicted to have the highest energy density in terms of weight and size, compared to direct methanol fuel cell (DMFC) and PEMFC systems [46].  $\mu\text{SOFCs}$  are also predicted to achieve three to four times the energy density of lithium-ion or nickel-metal hydride batteries. This feature is crucial because of the ever increasing functionalities offered by modern portable electronic devices are rapidly increasing energy density requirements for the power sources to a level that cannot be sustained by current rechargeable battery technologies. Moreover, a micro-fabricated SOFCs could possibly be integrated onto a single chip with other electronic circuits, enabling low cost and compact electronic devices.

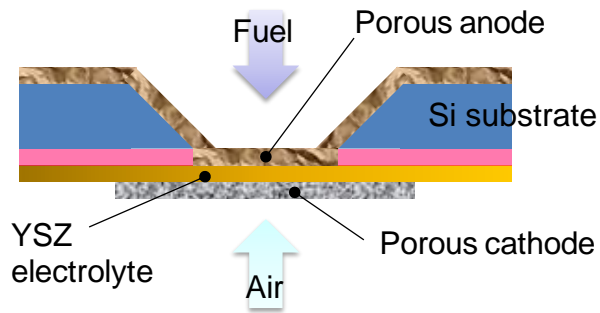


**Fig. 1.6** Schematic diagram of the design of a  $\mu$ SOFC based on a self-supported electrolyte membrane.

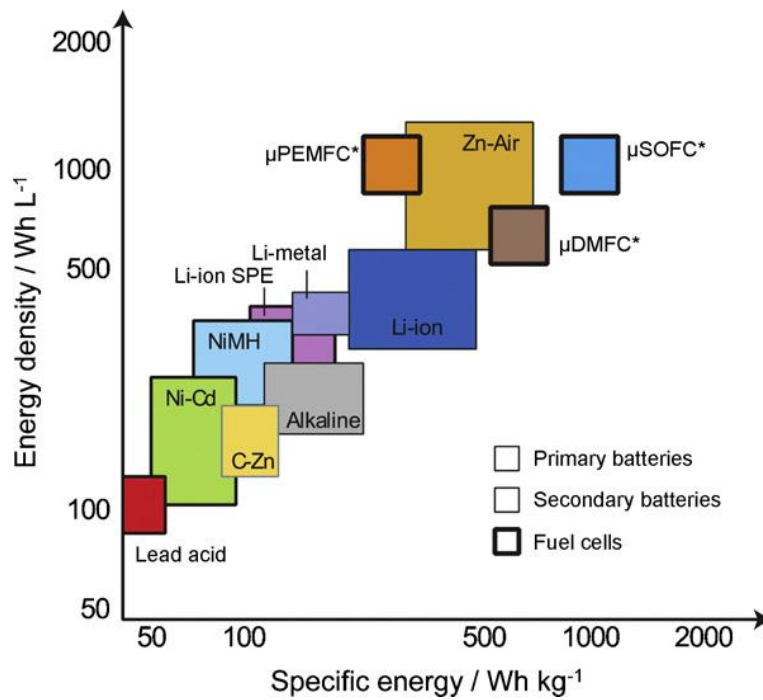


**Fig. 1.7** Estimated specific energy (per mass of device) and energy density (per volume of device) of several portable energy sources [46].

### 1.3.3 Hydrocarbon-fueled micro-solid oxide fuel cells

The aforementioned performance of  $\mu$ SOFCs in section 1.3.2 were mostly achieved by using hydrogen as the fuel, and operation, performance and properties of low temperature thin film  $\mu$ SOFCs using hydrocarbons as fuels have received less attention. Recently, a group of Harvard University demonstrated a peak power density of  $95 \text{ mW cm}^{-2}$  and OCV of  $0.85 \text{ V}$  at  $440 \text{ }^\circ\text{C}$  with a Pt anode  $\mu$ SOFC in weakly humidified methane, after optimizing the electrode morphology [57]. Pt is not an ideal catalyst for methane utilization, and the power density obtained was an order of magnitude lower than that with  $\text{H}_2$  fuel. The same group also demonstrated a peak power density of  $385 \text{ mW cm}^{-2}$  and OCV of  $0.77 \text{ V}$  at  $550 \text{ }^\circ\text{C}$  with Pd anode  $\mu$ SOFCs in weakly humidified methane, along with detailed studies on morphology and electrical conductivity on Pd thin films [15]. Pd catalysts exhibit excellent low temperature catalytic activity on methane reactions [59], however, the Pd anodes may face undesirable carbon deposition, which can potentially hinder overall cell performance. Indeed, growths of carbon fibers were observed on the Pd anode after methane operation of the  $\mu$ SOFC. **Table 1.2** summarizes selected recent works on thin film  $\mu$ SOFCs operated with hydrogen and methane as fuel.

**Table 1.2** Recent works on thin film  $\mu$ SOFCs operated with hydrogen or methane.

Year	2007	2008	2008	2011	2011	2011
Cell temperature °C	400	550	450	500	440	550
Power density $\text{mW cm}^{-2}$	400	152	861	1040	95	385
Open circuit voltage V	1.10	1.05	1.09	0.97	0.85	0.77
Fuel	H <sub>2</sub>	H <sub>2</sub>	H <sub>2</sub>	H <sub>2</sub>	CH <sub>4</sub> / 3%H <sub>2</sub> O	CH <sub>4</sub> / 3%H <sub>2</sub> O
Anode materials	Pt	Pt	Pt	Pt	Pt	Pd
Authors	Huang et al. [56]	Muecke et al. [60]	Su et al. [58]	Kerman et al. [57]	Kerman et al. [57]	Lai et al. [15]

## 1.4 Composite Anodes for Solid Oxide Fuel Cells

### 1.4.1 Nickle – yttria-stabilized-zirconia composite anodes in conventional solid oxide fuel cells

A dominant anode material for conventional high-temperature hydrogen fueled SOFCs has been Ni-YSZ cermets near half a century. A schematic view of Ni-YSZ cermets is depicted in **Fig. 1.8**. It consists of percolated YSZ and Ni three dimensional structure composing enhanced effective TPB lengths. In early SOFC developments, single phase materials such as iron oxides and Pt were investigated, but corrosion and resulting critical damage during operation was problematic. Transition metal anodes were not stable once the partial pressures of oxidation products in the anode exceed a critical value. Nickel is an excellent catalyst for hydrogen oxidation but has a significant thermal expansion mismatch compared to YSZ. Furthermore, at high temperatures Ni aggregates by grain growths obstructing the porosity of the anode, and reduces the TPB length required for electrochemical reactions. Ni-YSZ anode introduced by Spacil [61] made this composite a standard anode material in current SOFC technology. Two problems approached by introducing composite materials were, 1) mechanical stress between Ni anode and YSZ electrolyte during temperature changes induced by the large difference in thermal expansion coefficient, and 2) Ni aggregation during operation and resulting performance degradation of the cell. The main functionality of YSZ in the composite is essentially structural, to retain the dispersion of the metal particles and the porosity of the anode. Ni grains need to be electrically interconnected in order to be electrochemically active for fuel oxidation. The second important role of YSZ matrix is the oxide-ion conductivity to dimensionally expand electrochemically active area of the Ni catalysts by increasing active TPB length. A major disadvantage of Ni based anodes is their high activity towards hydrocarbon cracking. The rapid carbon deposition on Ni cermets indicates direct oxidation of hydrocarbons is not technically viable with Ni based anodes.

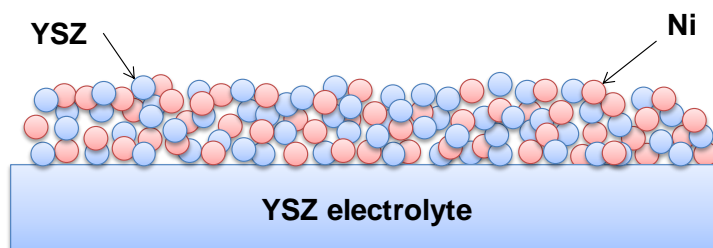


**Fig. 1.8** Schematic view of Ni-YSZ anodes on YSZ electrolytes.

#### 1.4.2 Nano-composite anodes for micro-solid oxide fuel cells

Although technical advantages of metal-ceramic composite as anode electrodes are widely accepted in conventional SOFCs, development of nano-composite electrodes for  $\mu$ SOFCs has gained relatively less attention. Analogous to their conventional counterparts, nano-composite electrodes are expected to restrain metal coarsening by confining metal grains in ceramic networks [62-66]. Past works on thin film composite electrodes were focused on Ni-ceramic composites, ceramic materials being either YSZ or gadolinia-doped ceria (CGO). One of the earliest results came from the group of Northwestern University. Wang et al. have fabricated Y-stabilized  $\text{Bi}_2\text{O}_3$  (YSB) / YSZ / Y-doped  $\text{CeO}_2$  (YDC) multi-layer thin-film electrolyte SOFCs using reactive magnetron sputtering [65]. A  $1\ \mu\text{m}$  thick Ag-YSZ cathode was first deposited on porous alumina substrate followed by a  $15\sim 20\ \mu\text{m}$  thick electrolyte. A  $1\sim 2.5\ \mu\text{m}$  thick NiO-YSZ thin film was deposited on the electrolyte as the anode electrode by reactive co-sputtering from Ni and Zr-Y metal targets. With the interfacial  $60\ \text{nm}$  thick YSB and  $100\ \text{nm}$  thick YDC layers, the fuel cell exhibited  $110\ \text{mW cm}^{-2}$  at  $750\ ^\circ\text{C}$  with hydrogen fuel. More recently, a group of Swiss Federal Institute of Technology (ETH) fabricated  $\sim 1\ \mu\text{m}$  thick nanoporous NiO-YSZ interlayer between NiO-YSZ anode support and  $1\ \mu\text{m}$  thick thin film YSZ electrolyte by pulsed laser deposition (PLD). Lanthanum strontium cobalt oxide (LSC) thin film was deposited on the electrolyte by PLD as the cathode electrode. With a  $200\ \text{nm}$  thick

CGO buffer layer between the cathode and the electrolyte, maximum power of 296 mW cm<sup>-2</sup> was obtained at 600 °C in hydrogen fuel [67, 68]. From the same ETH group, Muecke et al. investigated microstructures and electrochemical performance of Ni-CGO films prepared by spray pyrolysis and PLD on CGO pellets [69-71]. Performance was measured in a symmetrical Ni-CGO / CGO / Ni-CGO configuration in a single phase (hydrogen) atmosphere setup by impedance spectroscopy. The electrochemical performance improved with decreasing grain sizes for sprayed electrodes, where PLD electrodes showed slightly better performance compared to the sprayed electrodes. **Table 1.3** summarizes selected recent works on thin film nano-composite electrodes for thin film SOFCs.

**Table 1.3** Recent works on thin film nano-composite electrodes.

Year	1993	2004	2007	2008	2009
Electrode composition	NiO-YSZ Ag-YSZ	NiO-YSZ	Pt-YSZ	NiO-CGO	NiO-YSZ (interlayer)
Configuration	Cathode supported	Si substrate	YSZ substrate	YSZ/CGO substrate	Anode supported
Power density mW cm <sup>-2</sup>	<b>110</b>	-	EIS only	EIS only	<b>296</b>
Cell temperature °C	750	-	400	600	600
Fuel / Environment	H <sub>2</sub>	-	Air	H <sub>2</sub>	H <sub>2</sub>
Authors	Wang et al. [65]	La O et al. [72]	Hertz et al. [73]	Muecke et al. [69]	Noh et al. [67]

## 1.5 The Aim of this Work

The aim of this work is to explore performance and related characteristics of Ru based thin film anodes, namely nano-porous Ru thin film and Ru-CGO nano-composite thin film, for direct methane fueled  $\mu$ SOFCs operated at low temperature regime ( $\sim 500$  °C). Detailed material characterizations of Ru based thin films are investigated prior to applying them on  $\mu$ SOFCs, to understand thin film properties which of those are strongly relevant to the fuel cell performance. Subsequently,  $\mu$ SOFCs with Ru based anodes are fabricated by fine tuning the deposition parameters and their fuel cell performances are evaluated with methane fuels. Morphology and chemical state evolutions of the anodes are examined accordingly to investigate their stability under fuel cell operating conditions.

In chapter 2, microfabrication processes of thin film  $\mu$ SOFCs based on silicon technology is discussed in detail, starting from a 4 inch wafer to 10 x 10 mm Si chip with nine thin film self-supported  $\mu$ SOFCs embedded. Critical processes are defined and available control parameters will be discussed, especially in scope of applying Ru-CGO nano-composite thin film anodes on  $\mu$ SOFCs.

In chapter 3, thermal-electrochemical multi-physics one dimensional model is developed for a  $\mu$ SOFC platform, to gain a better understanding of operation conditions. Micro-SOFCs have ultra-thin electrolytes and electrodes, and thermal conditions under operation can be substantially different from those of conventional SOFCs. Various heat transfer mechanisms are considered such as surface radiation from the cathode, lateral conduction through electrolyte and electrodes bulk, and forced convection from the anode surface. Temperature dependent I-V characteristics, heat generations due to electrochemical overvoltage losses and Ohmic losses are considered. Temperature and current density distribution over the disc

geometry, and macroscopic heat balance is derived.

In chapter 4, characterization results of nano-porous Ru thin films will be presented, targeting utilization as anodes for direct methane supplied  $\mu$ SOFCs. Nano-porous Ru thin films were fabricated by DC sputtering from a Ru metal target. To the best of our knowledge, Ru has not yet been investigated as thin film  $\mu$ SOFC anodes; therefore, the primary emphasis in this chapter is on understanding microstructural and electrical characteristics of Ru thin films. The initial target is to understand following aspects of nano-porous Ru thin films;

- Control window of the Ru thin film deposition rate.
- In-plane electrical conductivity path formation: Dependence on film thicknesses and deposition conditions.
- Film porosity of the Ru thin film: Dependence on deposition conditions.
- Thin film morphology: Dependence on thicknesses and deposition conditions.
- Microstructural stability under elevated temperature: Morphology evolution, change in grain sizes and their interconnectivity under 500 °C annealing.
- Ru-YSZ Interface nanoscale morphology: As-deposited interfacial nano-structure and formation of triple phase boundaries under 500 °C annealing.

In chapter 5, nano-porous Ru thin film anodes are processed on  $\mu$ SOFC platforms following the insights learned in the previous chapter, and their fuel cell performances are evaluated. Three % humidified methane was used as the fuel. In addition, the evolution of Ru anode morphology under methane and hydrogen operation are compared and discussed.

Subsequently, fuel cell performance of the  $\mu$ SOFCs are investigated with variety of fuels, namely dry hydrogen, methane, natural gas and 3 % humidified natural gas. Dry fuels are preferred in real world applications because even humidification to room temperature dew

point will require an additional humidifier to the system. Following the fuel cell performance tests, extended performance stability of nano-porous Ru anode and Ru-CGO composite anode  $\mu$ SOFCs are investigated, where intermittent cell current oscillations were observed. The target of the study is to understand following aspects of the Ru anode  $\mu$ SOFC;

- ◆ Morphology of Ru anodes on  $\mu$ SOFC platform.
- ◆ Fuel cell performance with direct supply of 3 % humidified methane.
- ◆ Microscopic integrity of Ru anode  $\mu$ SOFCs.
- ◆ Ru anode nano-structural stability under fuel cell operation.
- ◆ Possible risk of carbon depositions.
- ◆ Fuel cell performance with various fuels, namely dry hydrogen, methane, natural gas and 3 % humidified natural gas.
- ◆ Behavior of fuel cell current under constant voltage operation: Characterize instability like behavior.
- ◆ Changes in surface oxidation states of Ru anodes: Dependence on fuel kinds.
- ◆ Reveal potential origin of the oscillation: Electrochemical activity change of Ru anodes related to surface oxidation, and recovery mechanism of the activity.

In chapter 6, basic characterization of Ru-CGO nano-composite thin films are presented, targeting utilization as anodes for direct methane supply  $\mu$ SOFCs. Ru-CGO nano-composite thin films were fabricated by co-sputtering from Ru metal and CGO ceramic targets. Following the results from chapter 4, we learned Ru is an excellent anode material for direct methane utilization, but its nano-structural stability under operating condition remained as a concern. Metal-ceramic cermets (typically, Ni-YSZ) are commonly used in conventional SOFC anodes in order to stabilize electrode microstructure. CGO has been chosen as the ceramic material to stabilize Ru metal nanostructure. Doped ceria displays mixed ionic and electronic conduction

at low oxygen partial pressure and is resistant to carbon deposition [9, 74-77]. It also possesses good catalytic activity for hydrogen and methane oxidation processes [9, 10, 37]. Before fabricating the nano-composite anode  $\mu$ SOFCs, detailed understanding of microstructural and electrical characteristics of CGO and Ru-CGO thin films was set as the target, details listed as follows;

- Control window of Ru-CGO co-deposition and thin film atomic compositions.
- Thin film morphology: Dependence on substrates and film compositions.
- Crystalline phases in nano-composite thin films: Dependence on film compositions and thermal annealing.
- In-plane electrical conductivity path formation: Dependence on film compositions and deposition conditions.
- Film porosity of Ru-CGO thin films: Dependence on deposition conditions.
- Microstructural stability under elevated temperature: Change in morphology, grain sizes and in-plane electrical conductivity after thermal annealing in comparison with porous Ru metal thin film.

In chapter 7, Ru-CGO nano-composite thin film anodes were fabricated on  $\mu$ SOFC platforms following insights obtained in the previous chapter. To the best of our knowledge, this is the first attempt to explore metal-ceramic composite thin film anodes for self-supported thin film SOFCs. Microscopic structural integrity was the first concern when applying this composite thin film as  $\mu$ SOFC anodes, due to differences in chemical and thermal expansion characteristics between the thin film anode and the YSZ electrolyte. Focused targets through material and process engineering of the Ru-CGO nano-composite anode  $\mu$ SOFCs were to understand following aspects;

- ◆ Morphology of Ru-CGO anodes in a  $\mu$ SOFC platform.

- ◆ Thermal-mechanical microscopic structural integrity of Ru-CGO anode  $\mu$ SOFCs.
- ◆ Fuel cell performance with direct supply of 3 % humidified methane.
- ◆ Ru-CGO anode microstructural stability under fuel cell operation conditions.

In chapter 8, experimental and theoretical research results described from chapter 2 to 7 are summarized and overall conclusions will be derived.

## Chapter 2: Fabrication Processes of Micro-Solid Oxide Fuel Cells

### 2.1 Introduction to Micro-Solid Oxide Fuel Cell Fabrication

Reducing electrolyte thickness and electrode effective dimensions down to sub-micrometer region have multiple effects. Fuel cell performance at low temperature regime can be largely improved, for example with the use of a 1  $\mu\text{m}$  thick 8 mol% YSZ electrolyte the fuel cell operation temperature can be lowered to  $\sim 500$   $^{\circ}\text{C}$  without substantially compromising the performance. Besides a reduction in electrolyte Ohmic resistance, shifting the effective dimension of electrodes from micrometer ( $10^{-6}$ ) to nanometer order ( $10^{-9}$ ) can dramatically increase triple phase boundary (TPB) density and improve effective exchange current density. Furthermore, by reducing the operation temperature these nanostructured electrodes gain stability against coarsening, which is the primary degradation mechanism for the electrodes.

Micro-SOFCs are typically fabricated on silicon substrates by thin film deposition and semiconductor processing techniques [78-80, 119, 120]. Thicknesses of electrolyte membranes in thin film  $\mu\text{SOFCs}$  can be decreased down to sub-micrometer regime [46, 57, 58] and the dimensions of the material microstructure (e.g. grain size and layer thickness) can be extended down to the nanometer scale. As shown in the schematics in **Fig. 2.1**,  $\mu\text{SOFC}$  design is based on a dual chamber configuration where a dense, self-supported electrolyte membrane separates the fuel and oxidant gases and also serves as a mechanical support for anode and cathode electrodes. Avoiding high-temperature ceramics processing and fuel cell operation is extremely beneficial; chemical and thermal material compatibility problems at electrode/electrolyte interfaces are reduced, and metal components for electrodes and interconnects can be used.

The materials used for  $\mu\text{SOFC}$  electrodes should have suitable electrical conduction properties as well as chemical compatibility with the components they are in contact with, and structural stability at both fabrication and operation conditions. Precious metals, mainly

sputtered Pt, are mostly used for electrode material due to its simplicity, good availability, chemical stability and catalytic properties for investigating the cell performance of the  $\mu$ SOFCs [56, 81]. Only small amounts of materials are required for  $\mu$ SOFC electrodes due to their sub-micrometer scale thicknesses, and material costs are not a major concern compared to the process related costs. From the morphological point of view, electrodes should be porous in order to allow a sufficient gas exchange at the gas–electrolyte–anode interface (or TPB). Furthermore, the anode material should be catalytically active towards oxidation of the fuel, and the cathode material should be active towards reduction of oxygen under the operation temperature.

**Figure 2.2** shows an example planar view of a platinum cathode consisting of a porous network. High porosity is required for sufficient fuel access and a large TPB length, where an interconnected two dimensional metal network is necessary for in-plane current collection. The degree of porosity is a function of the thickness of the electrode and deposition conditions. Optimal deposition parameters need to be established in order to maximize the fuel cell performance by controlled balance of the porosity and the interconnectivity of metal grains [57].

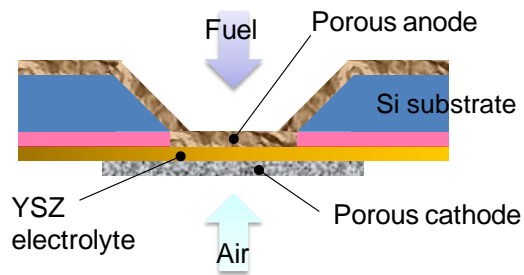


**Fig. 2.1** Schematic diagram of the design of a  $\mu$ SOFC based on a self-supported electrolyte membrane with anode and cathode layers.

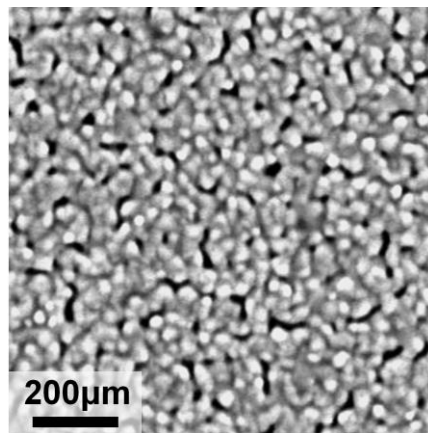


**Fig. 2.2** A typical SEM image of a platinum thin film  $\mu$ SOFC cathode.

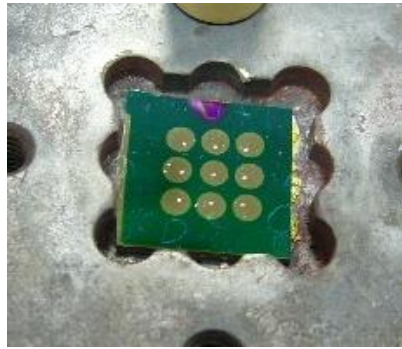
The dark areas are pores.

## 2.2 Fabrication Processes of Micro-Solid Oxide Fuel Cell Platform

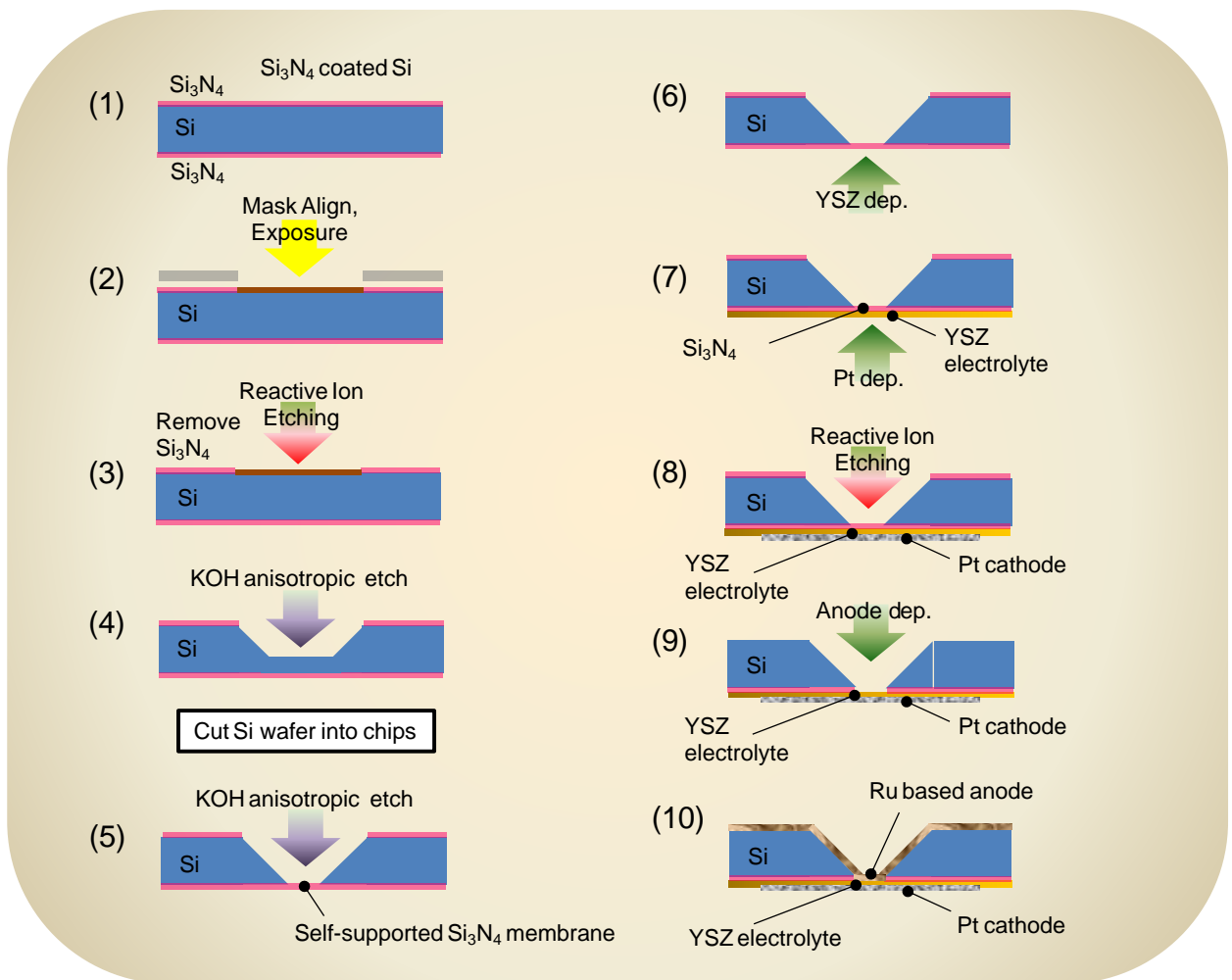
In this research, silicon processing technologies developed for micro-electromechanical systems (MEMS) are utilized to process  $\mu$ SOFCs. Microfabrication enables unique designs with ultra-thin self-supported dense membrane as the support for the cathode/electrolyte/anode cell structure.  $10 \times 10 \times 0.5 \text{ mm}^3$  silicon nitride ( $\text{Si}_3\text{N}_4$ ) double side coated silicon chips were used as substrates for  $\mu$ SOFC fabrication. Each chip was processed to have nine individual fuel cells with designed widths of 160 to 200  $\mu\text{m}$ . A typical view of a fabricated  $\mu$ SOFC chip is shown in **Fig. 2.3 (a)**.

The microfabrication process for self-supported electrolyte oxide membranes is shown in **Fig. 2.3 (b)** [56, 78]. First, to prevent electrical current leak and to avoid reaction between silicon and YSZ, 200 nm thick low-stress  $\text{Si}_3\text{N}_4$  was coated on both sides of 500  $\mu\text{m}$  thick, 4 inches diameter double-side polished (100) silicon wafer by low-pressure chemical vapor deposition (1). Each silicon wafer was designed to provide 32 of  $10 \times 10 \text{ mm}$  square  $\mu$ SOFC chips. Next, on one side of the wafer, photoresist (Shipley 1813) was coated by spin coating. With conventional photolithography method, 32 individual squares that define  $\mu$ SOFC chip profiles, each having nine square shaped openings, were patterned on one side of the silicon wafer (2). This step was conducted on a Karl Suss MJB-3 mask aligner, where exposed photoresist was removed by Shipley CD-26 developer. After hard baking the photoresist at 150  $^\circ\text{C}$ ,  $\text{Si}_3\text{N}_4$  layer at the exposed area was removed by reactive ion etching (RIE) with radio-frequency (RF) power of 100 W in oxygen ( $\text{O}_2$ ) and tetrafluoromethane environment at 65 mTorr (3). In step (4), opened Si windows were anisotropically etched in 30 wt% KOH at temperatures of 72  $^\circ\text{C}$  with an etch rate of  $\sim 50 \mu\text{m}$  per hour [82]. KOH attacks Si preferentially in the  $\langle 100 \rangle$  plane, producing a characteristic anisotropic V-etch with sidewalls that form a 54.7 deg with the surface plane (35.3 deg from the normal plane). To target 160~200  $\mu\text{m}$  square opening at the other side of the wafer, the opened Si window was designed to be 870~910  $\mu\text{m}$  square. After

removing ~450  $\mu\text{m}$  of silicon, fabricated structure was cut and divided into 32 individual 10 x 10 mm chips. Each silicon chip was etched again in 30 wt% KOH to remove away the rest of Si from the patterned open window. As  $\text{Si}_3\text{N}_4$  has a very low etch rate in KOH, the 200 nm  $\text{Si}_3\text{N}_4$  layer works as an etch stopper. With completions of the etch, nine individual self-supported  $\text{Si}_3\text{N}_4$  membranes remain on the other side of the chip (5). At the next step (6), thin film YSZ electrolytes were deposited on  $\text{Si}_3\text{N}_4$  membranes by RF magnetron sputtering from a  $\text{Y}_2\text{O}_3$  8 mol% :  $\text{ZrO}_2$  92 mol% target in argon (Ar) environment with a deposition pressure of 5 mTorr and 100 W target power for 60~80 minutes. The target consisted of a circular pellet, two inches in diameter. ATC Orion sputtering system (from AJA International, Inc.) was used for both RF and DC sputtering (**Fig. 2.4**). At the YSZ electrolyte deposition, Si chips were heated to a temperature of 550  $^\circ\text{C}$ . Next, thin film porous Pt cathodes were deposited on top of YSZ electrolyte by DC sputtering in Ar environment with deposition pressure of 75 mTorr and 250 W target power for 10~15 minutes without substrate heating. Physical shadow masks were applied to separate cathodes between individual cells (7). Deposition rates of the thin films were calibrated by X-ray reflectivity (XRR) measurements of films deposited on single crystal sapphire substrates with a Bruker D8 X-ray Diffractometer in parallel beam geometry. Nominal deposition rates of YSZ and Pt films were estimated to be 0.7 and 3.4  $\text{nm min}^{-1}$ , respectively. Subsequently,  $\text{Si}_3\text{N}_4$  in the window structure as well as that on top of Si was etched away by RIE under the same condition with step (3) to release self-supported YSZ/Pt membranes (8). As the final step (9), anodes were deposited on YSZ/Pt membranes by sputtering to complete the self-supported  $\mu\text{SOFC}$  structure (10). In this study, metal Ru and Ru-CGO composites were deposited as anode materials. Detailed deposition conditions of anode materials are discussed in the following chapters.



(a)



(b)

**Fig. 2.3** (a) A typical view of a 10 x 10 mm completed  $\mu$ SOFC chip from cathode side, and a (b) fabrication flow of thin film self-supported  $\mu$ SOFC on a Si chip.



**Fig. 2.4** ATC Orion sputtering system (from AJA International, Inc.) used for depositions of thin film electrolytes and electrodes.

### 2.3 Critical Processes in Scope of Applying Ruthenium Based Anodes on Micro-Solid Oxide Fuel Cells

There are two critical processes where careful engineering was required upon fabricating Ru based anodes on  $\mu$ SOFC platform. The first is the YSZ deposition process, and the effect of deposition temperature will be discussed in detail in the following paragraphs. Another critical process is the Ru-CGO composite anode deposition. In case of porous metal anodes such as Pt, Pd or Ru [15, 39, 57], the two dimensional porous structure can absorb stresses generated by condition changes through fuel cell testing processes, such as heating up the cell and anode chemical condition change from air to fuel. However, in case of Ru-CGO composite anodes, the electrode microstructure is rather dense and condition change at the anode may generate internal stress sufficient to destroy the  $\mu$ SOFC structure. Addition to be rather dense, ceria containing composite anode tend to change its volume under reducing condition [18, 83]. The control parameters available to mitigate internal stress generation of the composite anodes are deposition pressure and power. This will be further discussed in chapters 6 and 7.

In order to investigate possible effects on YSZ thin film electrolyte thermal-mechanical stability during operation, depositions were done under two different substrate temperatures, i.e. without substrate heating and with heating to 550 °C. **Figure 2.5 (a)** shows an optical microscope image of a self-supported  $\mu$ SOFC with YSZ electrolytes deposited without substrate heating. The electrolyte thickness was ~150 nm. The YSZ electrolyte shows a slight buckling pattern indicating weak compressive stress. **Figure 2.5 (b)** shows an optical image of a self-supported  $\mu$ SOFC with YSZ electrolyte deposited with substrate temperature of 550 °C. The buckling pattern appears stronger, indicating larger compressive stress generated through the deposition process. The thermal expansion coefficient (TEC) of silicon substrate is  $2.6 \times 10^{-6} \text{ K}^{-1}$ , where that of bulk YSZ is  $10.5 \times 10^{-6} \text{ K}^{-1}$ . When temperature is cooled down from 550 °C to room temperature YSZ film shrinks more than the silicon substrate due to the difference

in TEC, which should in turn give more tensile stress to the self-supported YSZ membrane. The fact that we see the opposite trend, more compressive stress with 550 °C deposited membranes, suggests that there is a substantially stronger initial compressive stress generated at 550 °C deposition compared to room temperature deposition. This is presumably due to higher mobility of atoms (or clusters) reaching the substrate surface during the sputtering process, leading to more enhanced grain growths and denser microstructure. **Figure 2.6** shows XRD patterns of 550 °C deposited YSZ films on Si<sub>3</sub>N<sub>4</sub> coated Si substrate with peak positions of cubic YSZ. Measured peaks show good match with the expected peak positions of cubic YSZ. No clear peak was observed with the XRD patterns from YSZ films deposited without substrate heating, indicating the film is in amorphous or in fine-grained nano-crystalline form.

In fact,  $\mu$ SOFCs with YSZ electrolytes deposited at 550 °C showed excellent thermal-mechanical stability during heating up to fuel cell test temperature (500 °C), while  $\mu$ SOFCs with electrolytes deposited without substrate heating showed tendencies to turn into tensile mode and eventually break during the heating. Due to this superior thermal-mechanical stability of 550 °C deposited YSZ electrolytes, all the following fuel cell investigations with Ru and Ru-CGO anodes are done with electrolytes deposited with substrate heating.

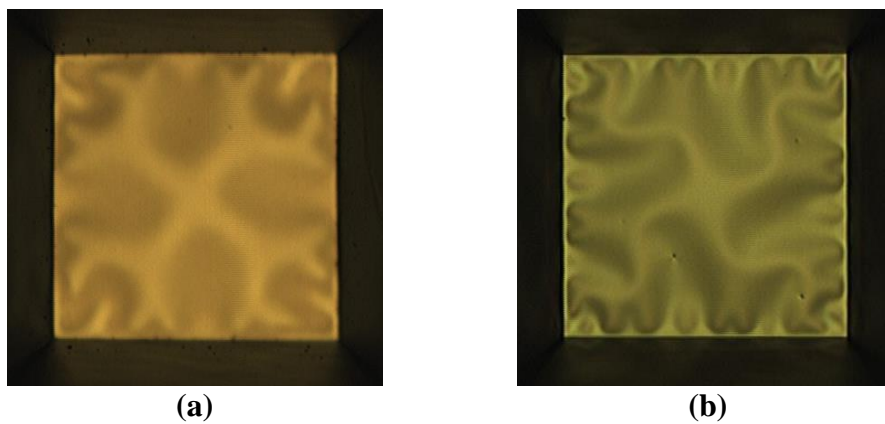


**Fig. 2.5** Optical microscope images of  $\mu$ SOFCs, (a) with YSZ electrolyte deposited without substrate heating, and (b) with YSZ electrolyte deposited at substrate temperature of 550 °C.

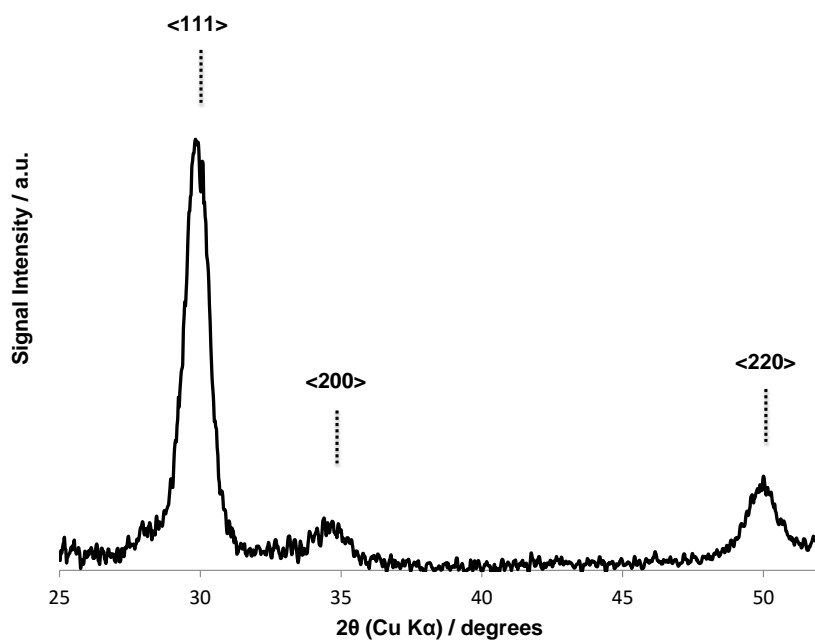
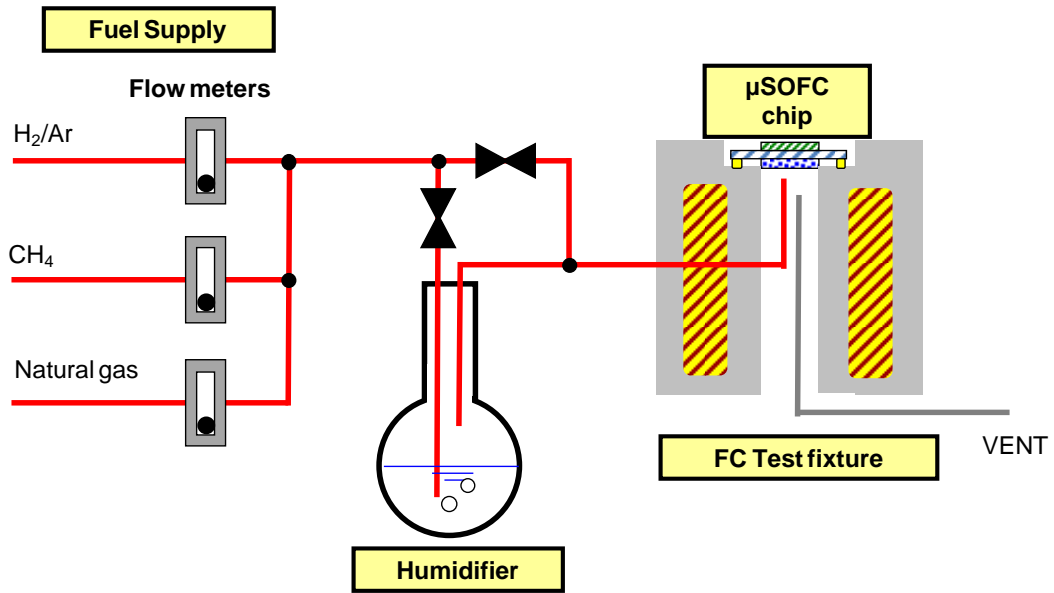


**Fig. 2.6** X-ray diffraction patterns of a 550 °C deposited YSZ film on  $\text{Si}_3\text{N}_4$  coated Si substrate. Peak positions of cubic YSZ indexed in JCPDS 00-030-1468 are presented in the figure.

## 2.4 Performance Measurement of the Fuel Cells

Micro-SOFCs were tested in a fuel cell test station, configured as depicted in **Fig. 2.7 (a)**. The anode side of the  $\mu$ SOFC was attached to a test fixture and sealed by a gold ring, whereas the cathode side was exposed to laboratory air. The fuel supply lines were designed to be able to switch between three fuels: natural gas, methane, and hydrogen. A humidifier filled with de-ionized water and a bypass line allowed direct or 3 % humidified fuel supply. The fuel was supplied to the anode compartment of the  $\mu$ SOFC after being preheated by the heater installed in the test fixture. **Figure 2.7 (b)** shows the appearance of the fuel cell test fixture part of the test station setup. Micro-SOFC chips were heated up in the test fixture at a controlled ramp rate to desired operation temperatures by an external heater. Dry 5 %  $\text{H}_2/\text{Ar}$  gas was supplied to the anodes of the  $\mu$ SOFCs at a flow rate of  $50 \text{ ml min}^{-1}$  during temperature ramp and for hydrogen fuel cell measurements. When a temperature of  $300 \text{ }^\circ\text{C}$  was reached, dry methane (purity 99.9 %) was fed at a flow rate of  $50 \text{ ml min}^{-1}$  for dry methane and natural gas fuel cell tests, where room temperature humidified methane was fed for 3 % humidified methane fuel cell tests. When a temperature of  $450 \text{ }^\circ\text{C}$  was reached, methane was further switched to dry natural gas fed at a flow rate of  $50 \text{ ml min}^{-1}$  for natural gas fuel cell tests. These gas switching procedures were used to confirm OCV at low temperature, and to avoid accelerated morphology change of the porous metal thin film during temperature ramp under a hydrogen atmosphere [39]. The fuel cell start-up procedure is summarized in **Fig. 2.8**. The sulfur content in a pipeline supplied natural gas was  $\sim 0.0017 \text{ \%}$  by weight. Current collection from individual  $\mu$ SOFC cells was done by contact probes. No additional current collector was applied, utilizing in-plane conduction through deposited electrodes (i.e. Pt cathodes, Ru anodes). Programmed current-voltage (I-V) measurements were carried out periodically during the temperature ramp. Extended operation for 300 minutes was performed at a constant voltage of  $0.7 \text{ V}$  between the anode and the cathode with a Solartron 1287A operated in potentiostatic mode, while keeping

the  $\mu$ SOFC chip temperature constant.



(a)



(b)

**Fig. 2.7 (a)** Schematic diagram of the fuel cell test station, fuels can be switched and humidifier can be connected / disconnected during the testing.

**(b)** Appearance of the fuel cell test fixture.

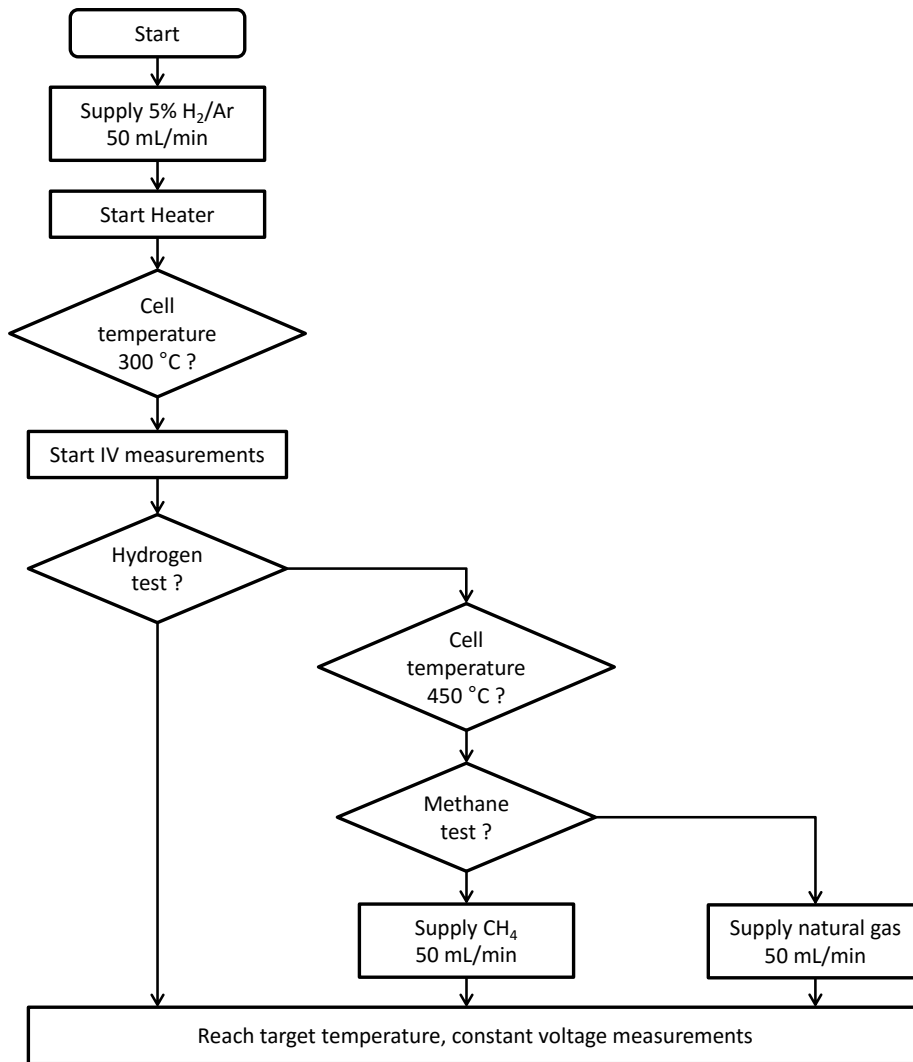


**Fig. 2.8** Flow diagram of the fuel cell test start-up, fuel kinds are switched during the cell heat-up.



## Chapter 3: Thermal-Electrochemical Multi-Physics Simulation on Micro-Solid Oxide Fuel Cells

### 3.1 Introduction

In this chapter, thermal-electrochemical multi-physics one dimensional modeling studies are performed on a  $\mu$ SOFC platform assuming disc shape, in order to evaluate temperature profile in the thin film. In the thermal model, various heat transfer mechanisms are considered such as surface radiation from the cathode, lateral conduction through electrolyte and electrodes, and forced convection from the anode surface. In the electrochemical model, temperature dependent I-V characteristics, heat generations due to electrochemical overvoltage losses and Ohmic losses are considered. The developed thermal model and the electrochemical model are integrated as a one dimensional disk form model to enable multi-physics simulation on the  $\mu$ SOFC platform. Temperature distribution and current density distribution over the disc geometry, and a macroscopic heat balance is derived.

### 3.2 Model Structure

#### 3.2.1 Overview

A thin film disc geometry with a radius of 75  $\mu\text{m}$  for a thermal-electrochemical simulation is schematically described in **Fig. 3.1** with related heat transfer mechanisms. The edge of the disc connects to the substrate, where the temperature is fixed to the controlled wall temperature as a boundary condition. Here, heat conducts in/out the fuel cell from/to the wall. Temperature along the fuel cell thickness direction is assumed constant due to an extremely high aspect ratio. The fuel is supplied from the bottom of the cell at the wall temperature, and with a flow rate of 0.01 m/s. Heat is exchanged between the fuel cell membrane and the fuel flow by forced convection. A heater block surrounds the cell which keeps the cell ambient air temperature at

the fuel cell operation temperature. The cathode of the cell is exposed to the ambient, where heat is dissipated to ambient temperature by thermal radiation. Fuel cell current flows through the cell and generates heat by Ohmic losses and electrochemical overvoltage losses. Local cell temperature is calculated based on a balance of heat transferred or generated by above mentioned mechanisms. Local cell current is calculated based on temperature dependent I-V curves, which characteristic is determined from a local cell temperature. Detailed one dimensional model configuration is schematically shown in **Fig. 3.2**, with model unit cells, related heat flows and electrical currents.

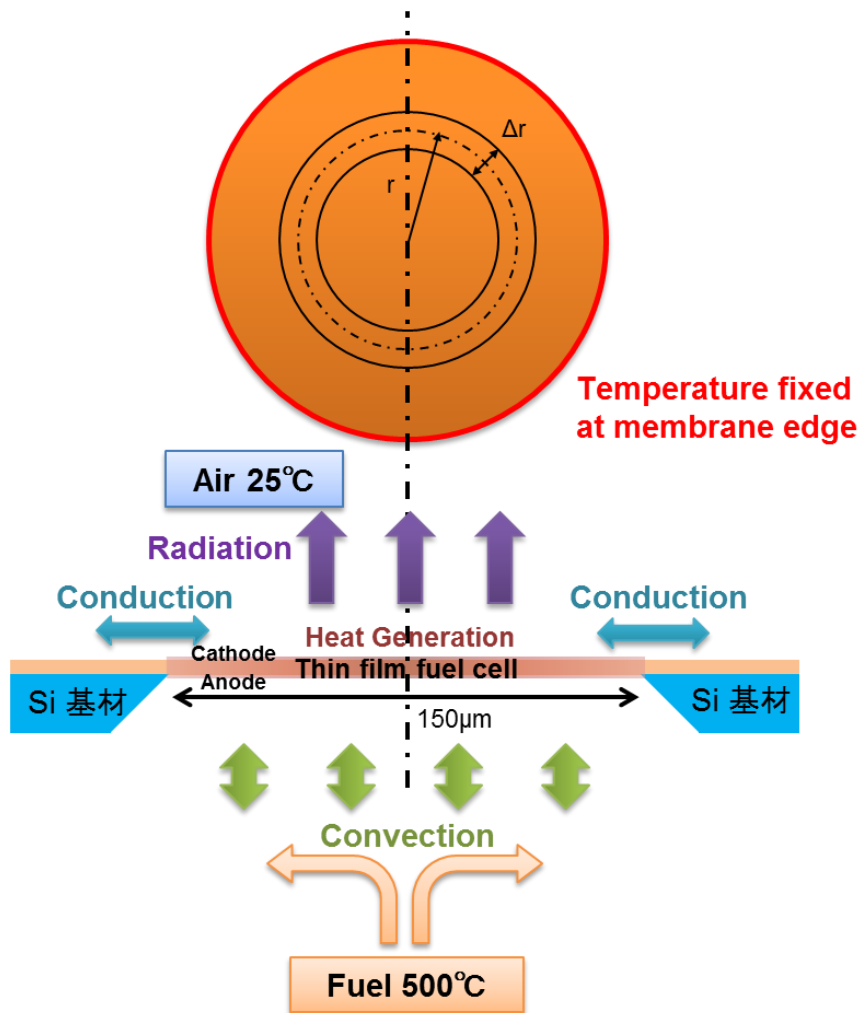


**Fig. 3.1** Thermal-electrochemical model of a disc shaped thin film  $\mu$ SOFC.

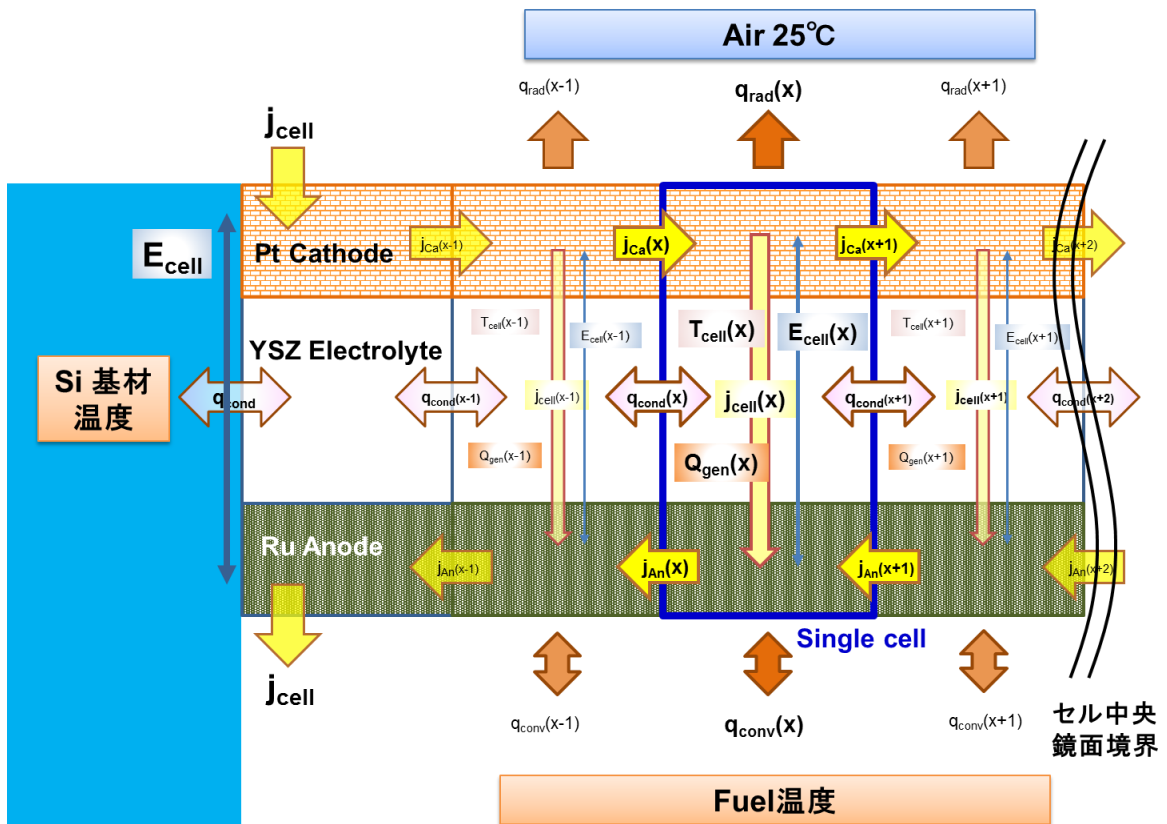


**Fig. 3.2** Detailed configuration of a thermal-electrochemical model with model unit cells, related heat flows and electrical currents.

### 3.2.2 Heat transfer model

#### Heat radiation

Heat radiation to the ambient from the cell cathode surface is modelled as stated in equation (3.1), where  $q_{rad}$  is the radiation heat transfer,  $\varepsilon$  the emissivity of the cathode,  $\sigma$  the Stefan-Boltzman coefficient ( $= 5.669 \times 10^{-8} \text{ W m}^{-2} \text{ K}^{-4}$ ),  $T_{cell}$  the local cell temperature, and  $T_a$  the ambient temperature.

$$q_{rad}(r) [\text{W m}^{-2}] = \varepsilon \cdot \sigma \cdot (T_{cell}^4(r) - T_a^4) \quad (3.1)$$

As a standard case, the cathode emissivity  $\varepsilon$  was set to 0.3 assuming a metallic Pt cathode electrode. The ambient temperature  $T_a$  was set to 25 °C.

#### Heat conduction

In-plane heat conduction within the cell and to/from the silicon support is modelled as equation (3.2), where  $q_{cond}$  is the in-plane conduction heat transfer,  $k$  the heat transfer coefficient,  $t$  the thin film layer thicknesses, and  $r$  the distance from the center of the cell. Subscripts  $An$ ,  $Elec$  and  $Ca$  stands for anode, electrolyte and cathode, respectively. The electrolyte heat transfer coefficient  $k_{Elec}$  was set to  $2.85 \text{ W m}^{-1} \text{ K}^{-1}$  from the YSZ bulk property. The anode heat transfer coefficient  $k_{An}$  was set to  $0.87 \text{ W m}^{-1} \text{ K}^{-1}$  from the Ru bulk thermal conductivity ( $117 \text{ W m}^{-1} \text{ K}^{-1}$ ) and from the fraction of nano-porous Ru film electrical conductivity compared to that of the bulk (0.0075). The cathode heat transfer coefficient  $k_{Ca}$  was set to  $19.4 \text{ W m}^{-1} \text{ K}^{-1}$  from the Pt bulk thermal conductivity ( $71.6 \text{ W m}^{-1} \text{ K}^{-1}$ ) and from the fraction of nano-porous Pt film electrical conductivity compared to that of the bulk (0.271). Thicknesses of the layers were set to  $t_{Elec} = 110 \text{ nm}$ ,  $t_{An} = 50 \text{ nm}$ , and  $t_{Ca} = 50 \text{ nm}$ .

$$q_{cond}(r) [\text{W}] = (k_{An} \cdot t_{An} + k_{Elec} \cdot t_{Elec} + k_{Ca} \cdot t_{Ca}) \cdot 2\pi r \frac{\Delta T_{cell}(r)}{\Delta r} \quad (3.2)$$

### Heat convection

Heat convection between the anode surface and the fuel gas is modelled as equation (3.3) assuming forced convection heat transfer.  $q_{conv}$  is calculated from  $h_{gas}$  the convective heat transfer coefficient,  $T_{gas}$  the fuel gas temperature and  $T_{cell}$ .  $h_{gas}$  is derived from a well known empirical correlation (3.4) between a Nusselt number  $Nu$ , Prandtl number  $Pr$  and Reynolds number  $Re$  and characteristic length  $L$ , for forced convection heat transfer.  $Re$  is calculated from the fuel flow velocity  $U_{\infty}$ , kinematic viscosity coefficient  $\nu$ , and  $L$ .  $Pr$  is derived from  $\nu$  and the thermometric conductivity  $\alpha$  as shown in equation (3.5).

$$q_{conv}(r) [W m^{-2}] = h_{gas} \cdot (T_{gas} - T_{cell}(r)) \quad (3.3)$$

$$Nu = \frac{h_{gas}L}{k_{gas}} = 0.664 \cdot Pr^{1/3} \cdot Re^{1/2} \quad (3.4)$$

$$Re = \frac{U_{\infty}L}{\nu}, \quad Pr = \frac{\nu}{\alpha} \quad (3.5)$$

### 3.2.3 Electrochemical model

#### Current-voltage relation

Local cell current is derived from a local fuel cell temperature  $T_{cell}$  and a local cell voltage  $E_{cell}$ , from the relationship presented in equation (3.6).  $E_{cell}$  and  $j_{cell}$  represents local cell voltage and current density, respectively, while  $j_{leak}$  represents leak current density through the cell. Contact resistance  $R_{con}$  and Tafel constant  $A$  is assumed to be constant regardless of  $T_{cell}$ . Theoretical OCV  $E_T^0$  is a function of the  $T_{cell}$  and is derived from Gibbs free energy and Nernst equation assuming oxidation of hydrogen generated by local steam reforming (for detail, see section 5.3).  $E_T^0$  is best fitted to the theoretical values with equation (3.7), and is shown in **Fig. 3.3**. Electrolyte resistance  $R_{Elec}$  and exchange current density  $j_0$  are also dependent on  $T_{cell}$ .  $R_{Elec}$  is modelled based on a bulk YSZ ionic conductivity property and is approximated with equation (3.8), and is shown in **Fig. 3.4**. Note that the contribution from  $R_{Elec}$  to the total cell voltage loss was negligible being at most 10 mV within the operation condition. I-V data obtained from cells operated at different temperatures (478~525 °C) are modeled with exchange current densities  $j_0$  in a form of equation (3.9) [84], as shown in **Fig. 3.5**.

$$E_{cell}(r) [V] = E_T^0(r) - (j_{cell}(r) + j_{leak}) \cdot (R_{Elec}(r) + R_{con}) - A \cdot \ln\left(\frac{j_{cell}(r) + j_{leak}}{j_0(r)}\right) \quad (3.6)$$

$$E_T^0(r) [V] = -0.000238 \cdot T_{cell}(r) + 1.2006 \quad (3.7)$$

$$R_{Elec}(r) [\Omega \text{ cm}^2] = t_{Elec} \cdot 10^{(0.02 + 3940/T_{cell}(r))} \quad (3.8)$$

$$j_0(r) [\text{A cm}^{-2}] = A \cdot \exp(-B/T_{cell}(r)) \quad (3.9)$$

$$(A: 1.0 \times 10^4, B: 2.2 \times 10^4)$$

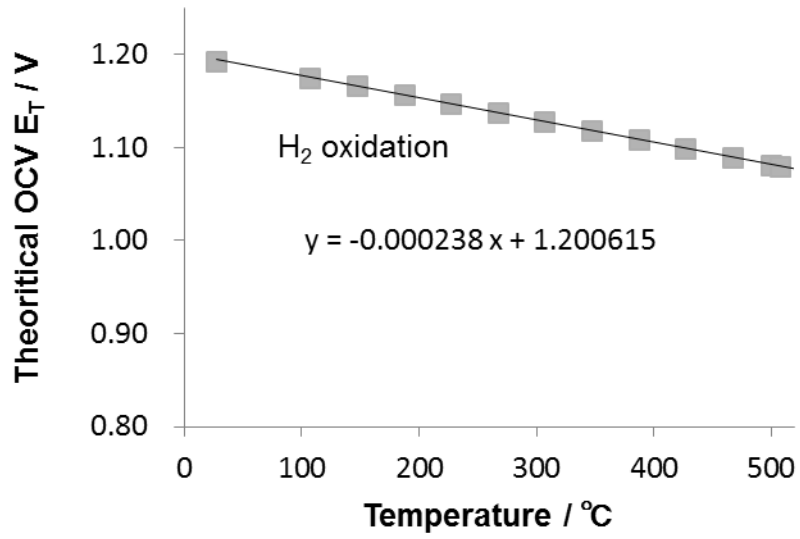


**Fig. 3.3** Theoretical OCV assuming reforming and hydrogen oxidation.

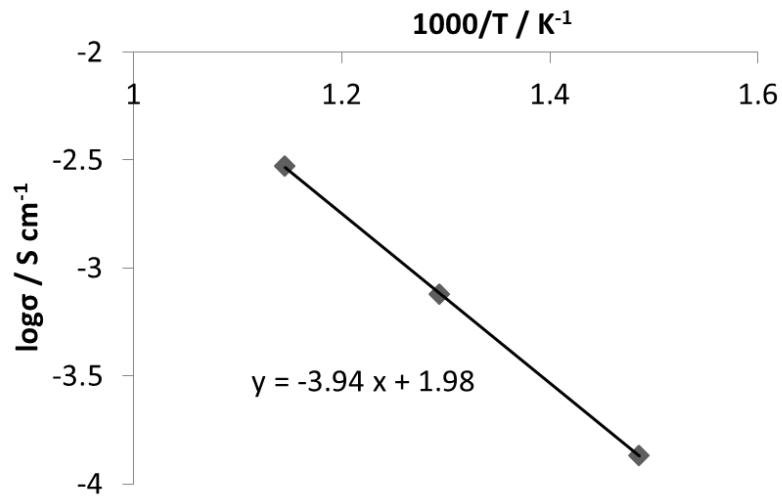


**Fig. 3.4** YSZ ionic conductivity dependence on temperature.

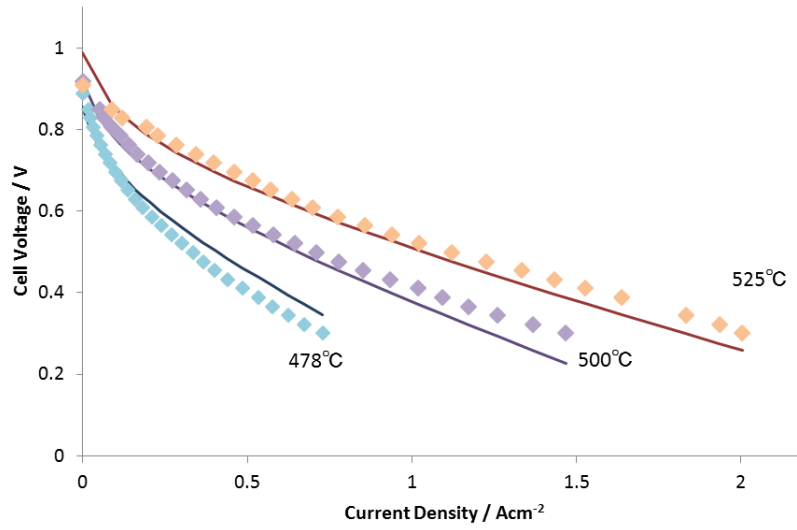


**Fig. 3.5** I-V curves from experimental data (solid markers) with modeled curves (solid lines) at different temperatures based on equation (3.6).

### Heat generation

Local heat generation  $q_{gen}$  in the cell occurs due to electrochemical overvoltage losses and in-plane / through-plane Ohmic loss.  $q_{gen}$  is modelled with equation (3.10), where  $I_{inp}$  is the local in-plane current,  $R_{Inp}$  the in-plane electrical resistance,  $I_{cell}$  the local fuel cell current which can be calculated by equation (3.11) with local fuel cell current density  $j_{cell}$ . The first half of the terms in equation (3.10) represents heat generation due to in-plane Ohmic losses, while the latter terms represents heat generation from irreversible electrochemical losses and through-plane Ohmic losses.

$$q_{gen}(r) [W] = I_{inp}(r) \cdot R_{Inp} + (E_T^0(r) - E_{cell}(r)) \cdot I_{cell}(r) \quad (3.10)$$

$$I_{cell}(r) [A] = j_{cell}(r) \cdot 2\pi r \Delta r \quad (3.11)$$

### 3.3 Results and Discussion

Using the developed thermal-electrochemical 1D model, impacts on temperature distribution, fuel cell current distribution and overall fuel cell characteristics from following five parameters are investigated.

- Fuel cell operation voltage (terminal voltage)
- Wall temperature
- Cathode emissivity
- Close system versus open system
- Degradation of electrode electrochemical performance

#### 3.3.1 Effect of fuel cell terminal voltage

The effect of the fuel cell terminal voltage on the cell temperature distribution and fuel cell current distribution was investigated by varying the voltage from 0.9 to 0.3 V while keeping other parameters constant. Cathode emissivity  $\varepsilon$  was fixed to 0.3, the wall temperature  $T_{\text{wall}}$  and fuel gas temperature  $T_{\text{gas}}$  were set to 500 °C. **Fig. 3.6 (a)** shows a fuel cell current density ( $j_{\text{cell}}$ ) distribution, and a cell temperature ( $T_{\text{cell}}$ ) distribution in a 150  $\mu\text{m}$  diameter circular cell along the radial direction from the cell edge to the center.  $T_{\text{cell}}$  drops towards the center of the cell in cases of terminal voltages above 0.5 V due to a strong heat radiation effect from the cathode surface, while  $T_{\text{cell}}$  rises in case of 0.3 V where the heat generation overcomes the radiation loss. **Fig. 3.6 (b)** shows a summary of change in cell center temperature and area averaged temperature with respect to the terminal voltage. Between terminal voltages of 0.9 and 0.3 V, the cell center temperature changes  $\sim 10$  °C while the change in the average temperature is  $\sim 5$  °C.  $T_{\text{cell}}$  exceeds the  $T_{\text{wall}}$  at terminal voltage of 0.4~0.5 V, where heat radiation and heat generation balance out. **Fig. 3.6 (c)** shows heat balance in the cell at terminal voltage of 0.7 V. While 102  $\mu\text{W}$  of heat dissipates away via radiation, 13  $\mu\text{W}$  of heat is generated through

electrochemical reaction and  $86 \mu\text{W}$  is supplied by heat conduction from the wall. The remaining  $3 \mu\text{W}$  is supplied by heat convection from the fuel gas.

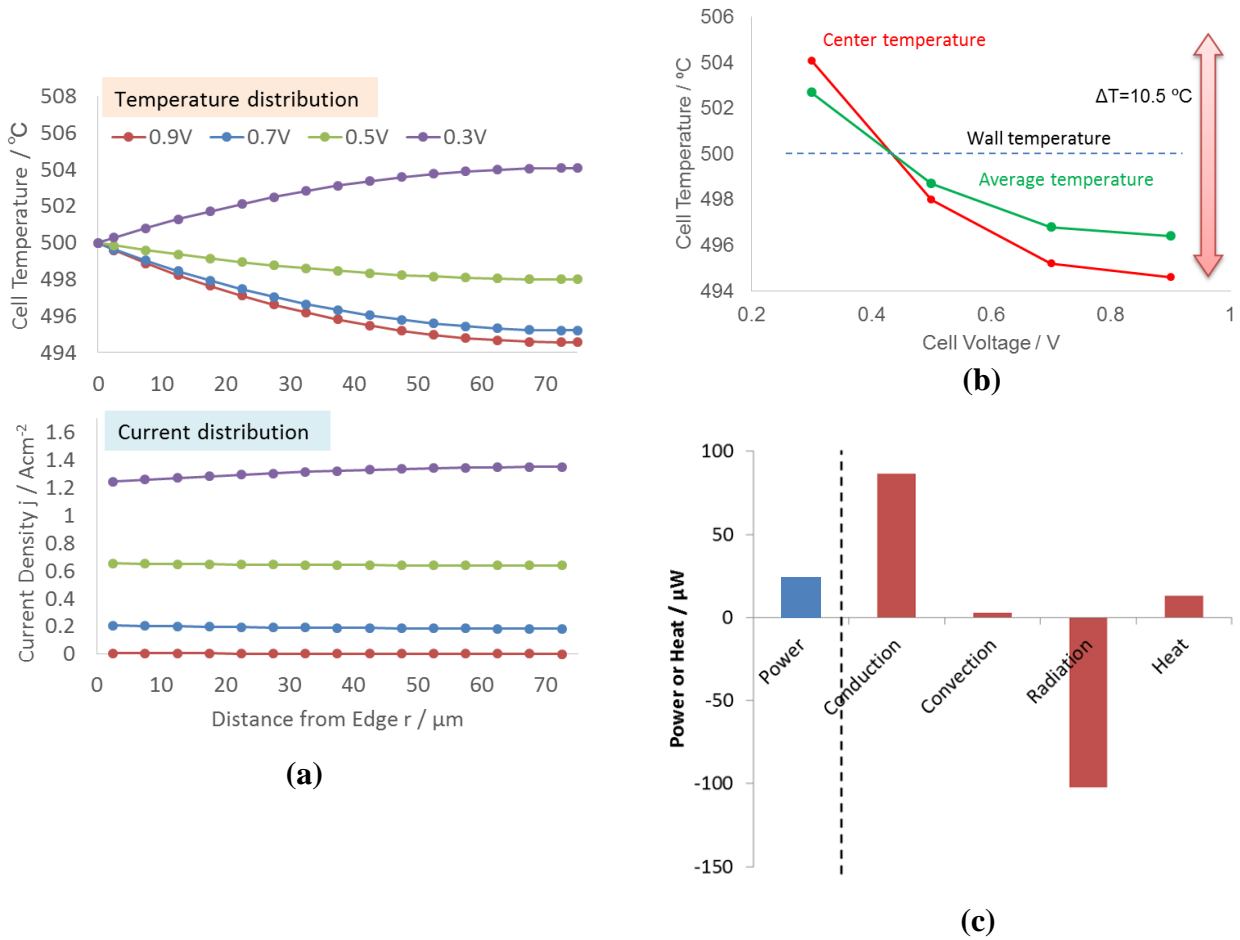


**Fig. 3.6 (a)** Fuel cell current density distribution, and a temperature distribution in a  $150 \mu\text{m}$  diameter circular cell along the radial direction from the edge to the center. The fuel cell terminal voltage was varied from 0.9 to 0.3 V, with wall temperature  $T_{\text{wall}}$  of  $500 \text{ }^\circ\text{C}$  and cathode emissivity  $\epsilon$  of 0.3. **(b)** Summary of change in cell center temperature and cell average temperature with respect to the terminal voltage. **(c)** Heat balance in the cell at terminal voltage of 0.7 V.

### 3.3.2 Effect of wall temperature

The effect of wall temperature  $T_{\text{wall}}$  on the cell temperature distribution, fuel cell current distribution and fuel cell performance was investigated by varying  $T_{\text{wall}}$  from 475 to 525 °C, while keeping other parameters constant. Cathode emissivity  $\varepsilon$  was fixed to 0.3, the terminal voltage was set to 0.7 V. **Fig. 3.7 (a)** shows a fuel cell current density ( $j_{\text{cell}}$ ) distribution, and a cell temperature ( $T_{\text{cell}}$ ) distribution. The current density increases exponentially with the wall temperature as expected. In all cases,  $T_{\text{cell}}$  drops towards the center of the cell due to strong heat radiation from the cathode surface. **Fig. 3.7 (b)** shows a summary of temperature drops of the cell center temperature and area averaged temperature compared to  $T_{\text{wall}}$ . Temperature drop is rather insensitive to  $T_{\text{wall}}$ , indicating dominant heat transfer mechanism in this operation regime being heat radiation. **Fig. 3.7 (c)** shows heat balance in the cell at  $T_{\text{wall}}$  of 525 °C. While 116  $\mu\text{W}$  of heat dissipates away via radiation, 25  $\mu\text{W}$  of heat is generated through electrochemical reaction and 89  $\mu\text{W}$  is supplied by heat conduction from the wall. The remaining 3  $\mu\text{W}$  is supplied by heat convection from the fuel gas. As can be seen, the main source and sink in the heat balance is conduction from the wall and radiation from the cathode due to relatively low heat generation at 0.7 V.

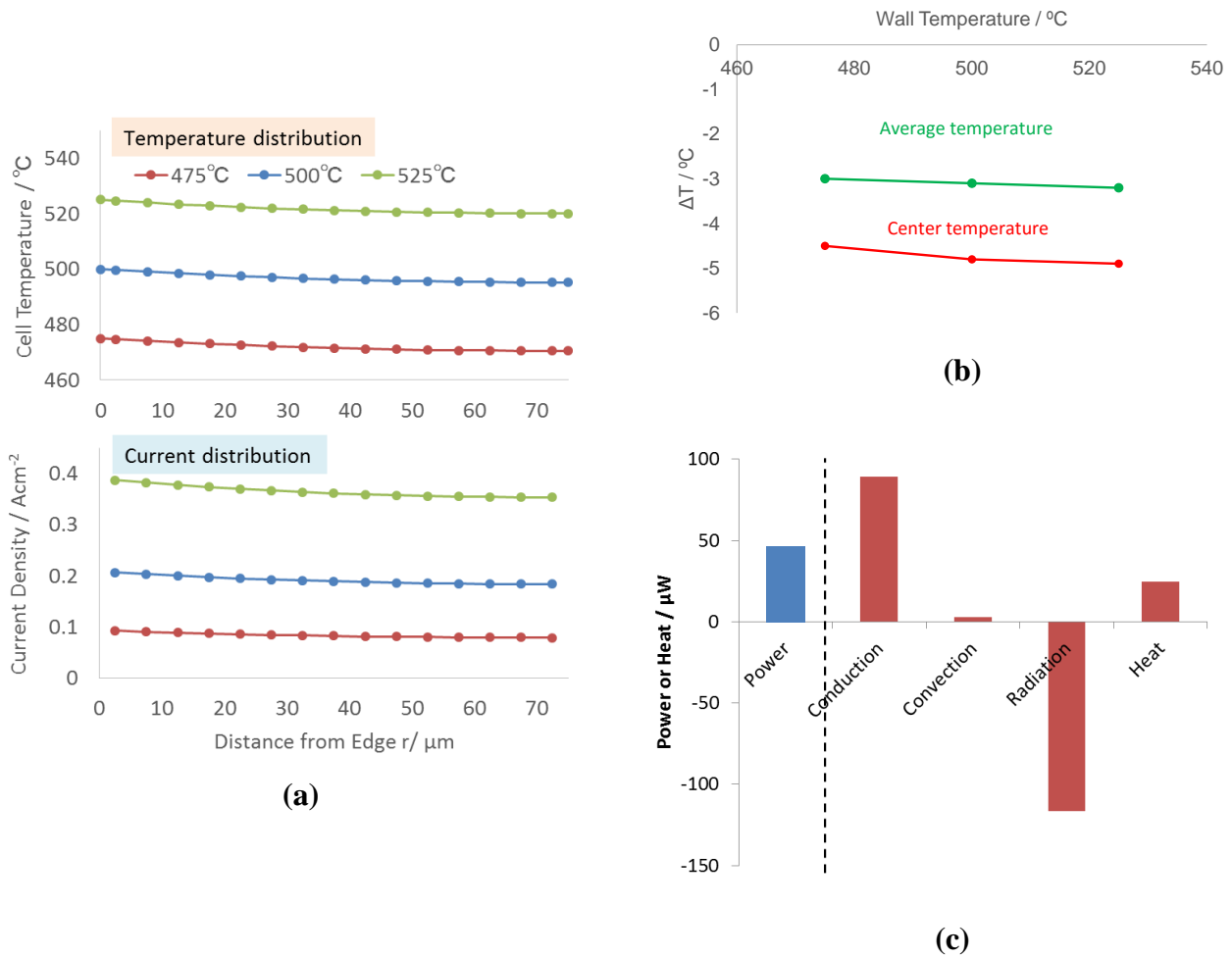


**Fig. 3.7 (a)** Fuel cell current density distribution, and a temperature distribution in a 150  $\mu\text{m}$  diameter circular cell with different wall temperatures  $T_{\text{wall}}$ , with cathode emissivity  $\epsilon$  of 0.3 and terminal voltage of 0.7 V.  $T_{\text{wall}}$  was varied from 475 to 525  $^{\circ}\text{C}$ . **(b)** Summary of change in cell center temperature and cell average temperature with respect to  $T_{\text{wall}}$ . **(c)** Heat balance in the cell at  $T_{\text{wall}}$  of 525  $^{\circ}\text{C}$ .

### 3.3.3 Effect of cathode emissivity

The effect of cathode emissivity  $\epsilon$  at cathode surface on cell temperature distribution and fuel cell current distribution was investigated by varying  $\epsilon$  from 0.1 to 0.6 while keeping other parameters constant. The wall temperature  $T_{\text{wall}}$  was fixed to 500 °C, while the terminal voltage was set to 0.7 V. **Fig. 3.8 (a)** shows a fuel cell current density ( $j_{\text{cell}}$ ) distribution, and a cell temperature ( $T_{\text{cell}}$ ) distribution. With increase in  $\epsilon$ ,  $T_{\text{cell}}$  shows steeper drop towards the center of the cell. **Fig. 3.8 (b)** shows a summary of cell center temperature and area averaged temperature with respect to  $\epsilon$ . The center and averaged temperature linearly increases with decreasing  $\epsilon$ . However, the radiation effect is so strong such that even with  $\epsilon$  of 0.1, the cell center temperature is lower than  $T_{\text{wall}}$ . **Fig. 3.8 (c)** shows heat balance in the cell at  $\epsilon$  of 0.6. While 199  $\mu\text{W}$  of heat dissipates away via radiation, 12  $\mu\text{W}$  of heat is generated through electrochemical reaction and 181  $\mu\text{W}$  is supplied by heat conduction from the wall. The remaining is supplied by heat convection from the fuel gas. Dominant source and sink in the heat balance are conduction from the wall and radiation from the cathode, due to relatively low heat generation at 0.7 V.

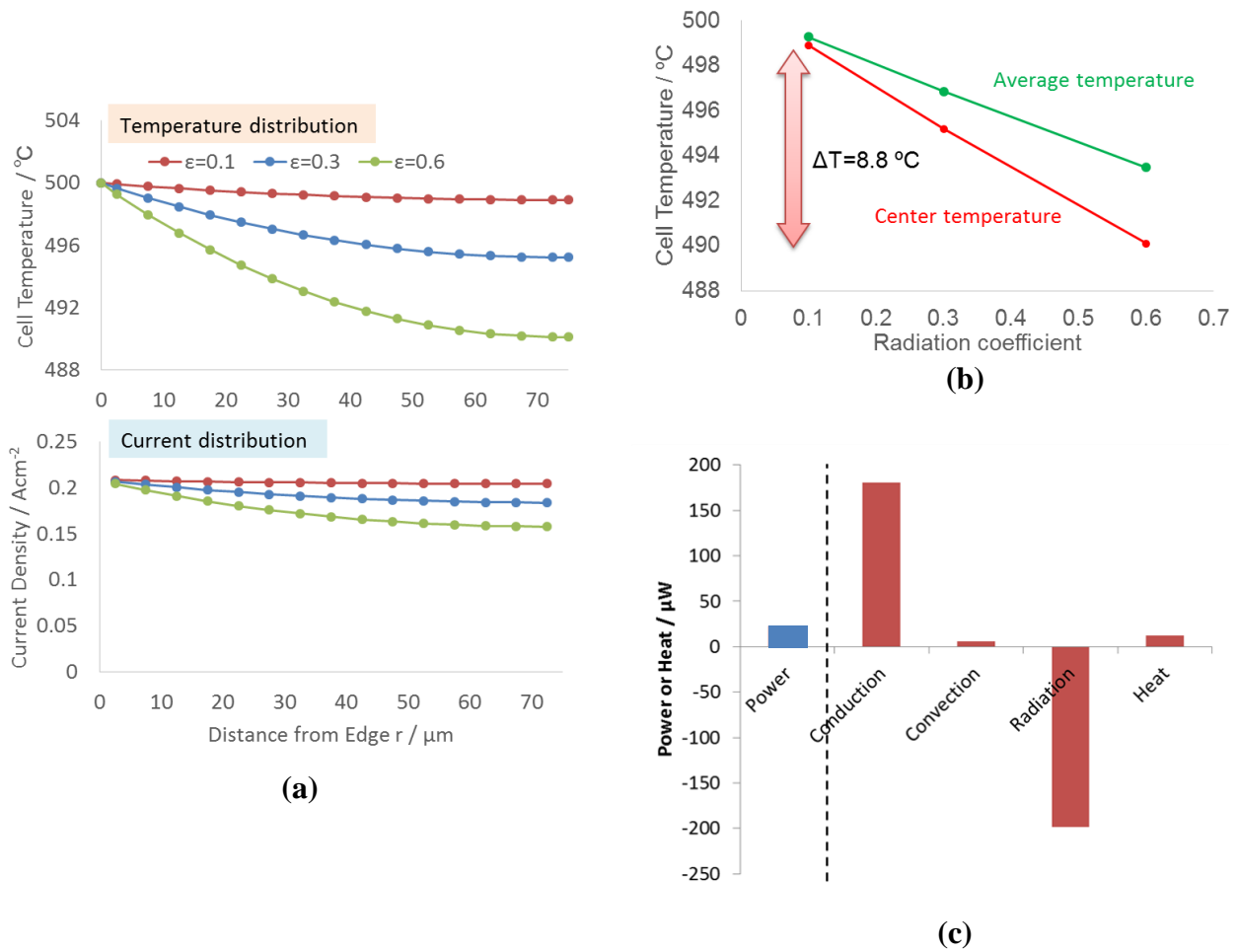


**Fig. 3.8 (a)** Fuel cell current density distribution, and a temperature distribution in a 150  $\mu\text{m}$  diameter circular cell with different cathode emissivity  $\epsilon$ , with wall temperature  $T_{\text{wall}}$  of 500  $^{\circ}\text{C}$  and terminal voltage of 0.7 V.  $\epsilon$  was varied from 0.1 to 0.6. **(b)** Summary of change in cell center temperature and cell average temperature with respect to  $\epsilon$ . **(c)** Heat balance in the cell at  $\epsilon$  of 0.6.

### 3.3.4 A closed system and an open system

The effect of a fuel cell terminal voltage on cell temperature distribution and fuel cell current distribution in a closed system was investigated by varying the terminal voltage from 0.9 to 0.3 V while keeping other parameters constant. Cathode emissivity  $\varepsilon$  was set to 0 (no radiation effect) assuming a closed system, where the wall temperature  $T_{\text{wall}}$  and fuel gas temperature  $T_{\text{gas}}$  was set to 500 °C. **Fig. 3.9 (a)** shows a fuel cell current density ( $j_{\text{cell}}$ ) distribution, and a cell temperature ( $T_{\text{cell}}$ ) distribution along the radial direction. In all cases,  $T_{\text{cell}}$  increases towards the center of the cell. **Fig. 3.9 (b)** shows a summary of change in cell center temperature and area averaged temperature with respect to the terminal voltage. Between terminal voltages of 0.9 and 0.3 V, the cell center temperature increases ~11 °C while the change in the average temperature is ~6 °C. **Fig. 3.9 (c)** shows heat balance in the cell at terminal voltage of 0.5 V. While 14  $\mu\text{W}$  of heat is generated through electrochemical reaction, 13  $\mu\text{W}$  dissipates away by heat conduction to the wall and 1  $\mu\text{W}$  is carried away by heat convection to the fuel gas. No radiation is present in this case.

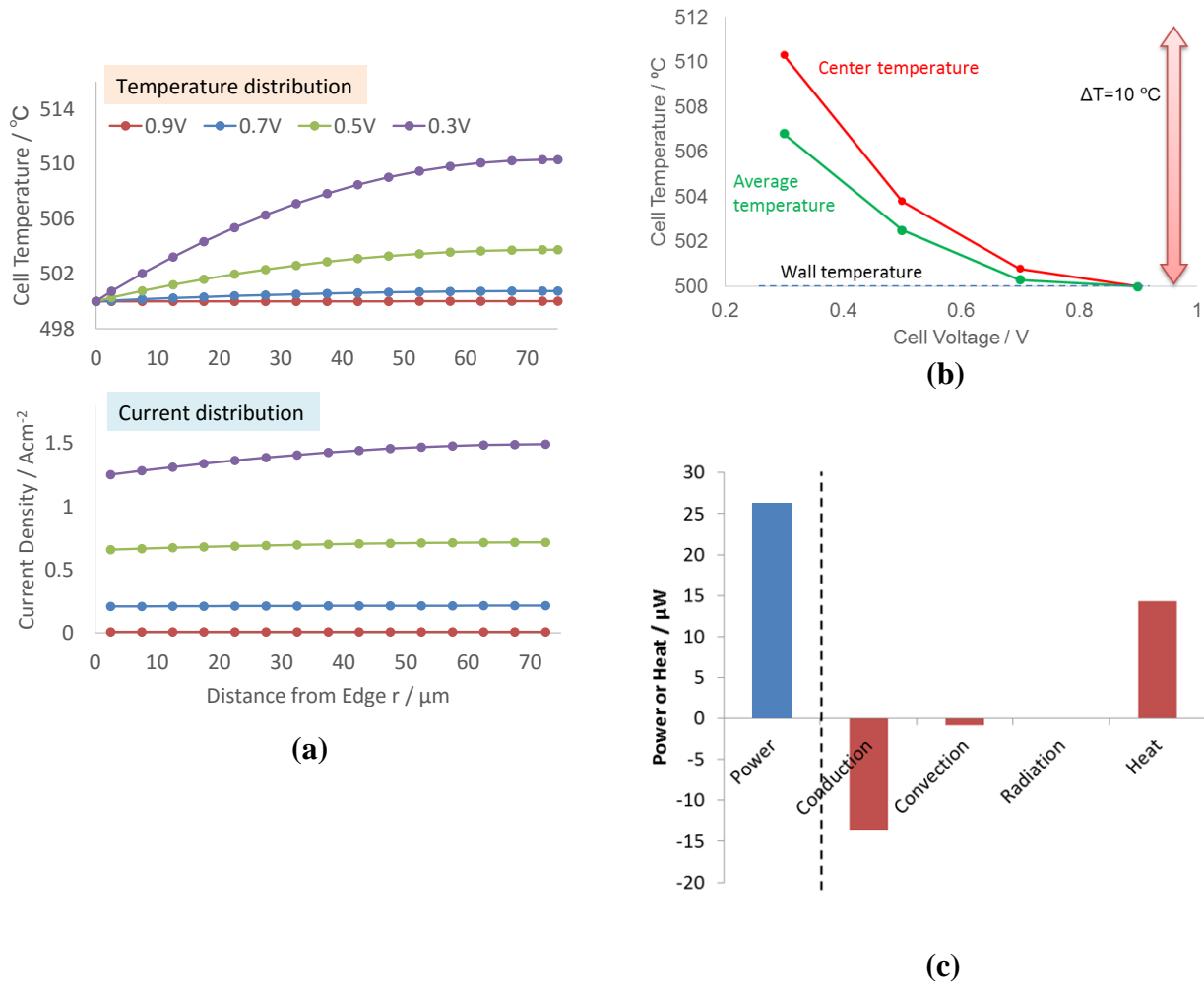


**Fig. 3.9** (a) Fuel cell current density distribution, and a temperature distribution in a 150  $\mu\text{m}$  diameter circular cell assuming closed system (no radiation), with different terminal voltages at wall temperature  $T_{\text{wall}}$  of 500 °C. (b) Summary of change in cell center temperature and cell average temperature with respect to the terminal voltage. (c) Heat balance in the cell at terminal voltage of 0.7 V.

### 3.3.5 Effect of electrode degradation

The effect of electrode degradation on the cell temperature distribution and fuel cell current distribution was investigated by varying the cell exchange current density  $j_0$  down to 57% from the original value, while keeping other parameters constant. Cathode emissivity  $\varepsilon$  was set to 0.3, the wall temperature  $T_{\text{wall}}$  and fuel gas temperature  $T_{\text{gas}}$  was set to 450 °C, and the fuel cell terminal voltage was fixed to 0.7 V. **Fig. 3.10** shows (a) fuel cell current density distribution, and (b) cell temperature  $T_{\text{cell}}$  distribution along the radial direction. The current density decreases with degradation in  $j_0$ , while there is only a slight change in  $T_{\text{cell}}$  distribution. At this operation voltage, dominant factors that determine the  $T_{\text{cell}}$  field are cathode surface heat radiation and electrode lateral heat conduction. Effect from the change in electrochemical heat generation resulted in a minor contribution.

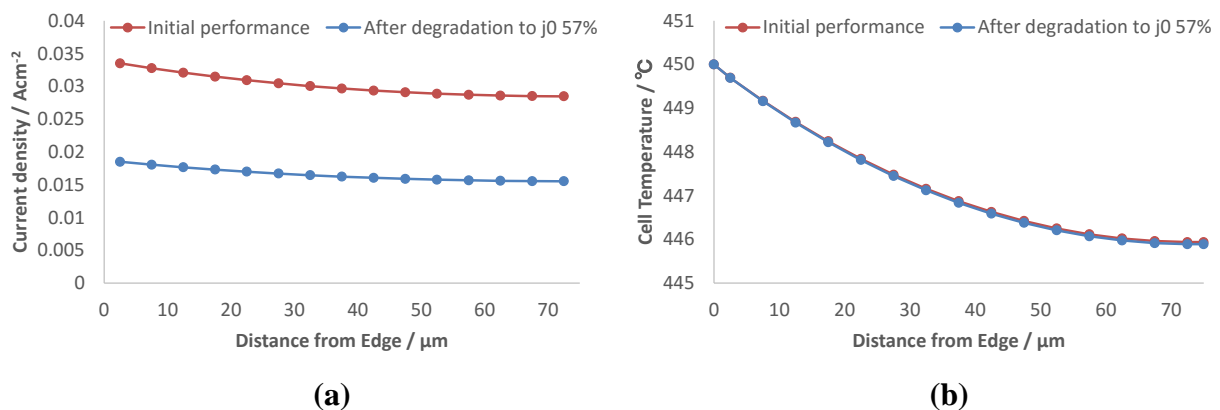


**Fig. 3.10** (a) Fuel cell current density distribution, and a (b) temperature distribution in a 150 μm diameter circular cell at terminal voltage of 0.7 V, cathode emissivity  $\varepsilon$  of 0.3, and wall temperature  $T_{\text{wall}}$  of 450 °C, before and after electrode degradation (57 % of the original).

### 3.4 Conclusions

In order to investigate temperature distribution, fuel cell current distribution and resulting impact on fuel cell performances, thermal-electrochemical integrated one dimensional simulation model was newly developed for a disc configuration  $\mu$ SOFCs. With regard to heat transfer models, heat radiation to the ambient from Pt cathode surface, lateral heat conduction to the substrates along multi-layered thin films, heat convection between anode electrodes and the fuel flow were considered. Temperature dependent I-V characteristics, heat generation due to electrochemical overvoltage losses, through-plane and in-plane IR losses were considered in the electrochemical model. Impact of fuel cell operation voltage, wall temperature, cathode emissivity, close system and electrode degradation were investigated using the constructed simulation model. Results are summarized as follows;

#### Impact of fuel cell operation voltage (terminal voltage)

- Due to a strong radiation cooling effect, temperature close to the center of the cell was lower than the controlled wall temperature at terminal voltages of 0.9, 0.7 and 0.5 V. At 0.3 V, heat generation within the cell overcame heat radiation. The temperature difference at the center of the cell was  $\sim 10$  °C between terminal voltages of 0.9 and 0.3 V.

#### Impact of wall temperature

- Average cell temperatures were lower than the controlled wall temperature for 4~5 °C at wall temperature of 475~525 °C. At higher wall temperature, heat generation within the cell increases due to an increased current density. However it did not result in further increase in the cell temperature due to a compensating radiation loss.

#### Impact of cathode emissivity

- Fuel cell temperature distribution was strongly sensitive on the cathode emissivity  $\epsilon$ . At  $\epsilon = 0.6$ , the cell center temperature dropped  $\sim 10$  °C from the wall temperature where at  $\epsilon = 0.1$ , the drop was  $\sim 1$  °C. This again indicates that in an open system, heat radiation is a

dominant mechanism in the overall heat transfer that determines the thin film fuel cell temperature.

#### Impact of a closed system

- In a closed system, heat radiation is neglected. As a result, the cell temperature is higher than the wall temperature at all terminal voltages (0.9~0.3 V). The difference in cell center temperature was ~11 °C between cell terminal voltages of 0.9 and 0.3 V, due to difference in heat generation. In case of a closed system, in-plane heat conduction removes the heat generated by electrochemical reactions.

#### Degradation of electrode electrochemical performance

- When exchange current density is reduced to 57 %, the current density distribution is reduced accordingly. At 450 °C wall temperature and at cell terminal voltage of 0.7 V, effect of change in heat generation to the cell temperature distribution is minor because dominant mechanisms are heat radiation and conduction.



## **Chapter 4: Characterization of Nano-Porous Ruthenium Thin Films for Micro-Solid Oxide Fuel Cell Anodes**

### **4.1 Introduction**

In this chapter, nano-porous Ru thin films for direct methane  $\mu$ SOFC anodes are explored. As there are not sufficient data available on physical and electrical properties of Ru thin films for utilization in  $\mu$ SOFC anodes, the primary emphasis was put on understanding microstructure evolution and electrical characteristics. Nano-porous Ru thin films were fabricated by DC-sputtering from a Ru metal target. Deposition rates, film morphology, film porosities and in-plane electrical conductivities were explored on as-deposited films. Binarization image analysis was applied on planar SEM images to understand current conduction path formation. Thermal annealing was applied on the films to investigate nano-structural stability of the films, where morphological and in-plane electrical conductivity evolutions were evaluated.

### **4.2 Experimental Details**

#### **4.2.1 Deposition and characterization of nano-porous ruthenium thin films**

Basic properties of Ru thin films deposited on 0.5 mm thick single crystalline YSZ <100> (sc-YSZ) substrates (MTI Corp.) were investigated. Ruthenium films were deposited by DC sputtering from a Ru metal target (purity 99.9 %, from AJA International, Inc.) in argon (Ar) environment without substrate heating. First, depositions were carried out in 75 mTorr Ar and 250 W target power without substrate heating, with similar condition to porous Pt anode deposition reported in previous works [57, 78, 85]. The deposition time ranged from 5 to 25 min, while the Ru film thickness showed a linear relationship with the deposition time. Thicknesses and deposition rates of the films were measured by X-ray reflectivity (XRR) with a Bruker D8 X-ray Diffractometer in a parallel beam geometry. Morphology of Ru thin films

were investigated with a Carl Zeiss Ultra 55 field emission SEM. In-plane electrical conductivities of Ru thin films at room temperature were measured by a Creative Design Engineering four point probe resistivity measurement system ResMap 178.

Secondly, morphological and electrical properties of Ru thin films deposited at different pressures and powers were investigated. Deposition pressure was varied between 10~75 mTorr while target power was varied between 50~200 W. Ru film thicknesses resulted in 15~85 nm range. Film porosities of the film deposited with different pressures were compared by analyzing critical angles obtained from XRR measurements. Interconnectivity of the Ru grains was analyzed by processing planar SEM images with an ImageJ software.

Interface nano-structures of Ru thin films on YSZ substrates are investigated by cross-sectional transmission electron microscope (TEM) analysis at Kobelco Research Institute. Ru thin film samples were coated with carbon by vacuum vapor deposition, followed by a tungsten coating in a focused ion beam (FIB) process equipment (FB-2000A, Hitachi). Cross-sectioned thin films were sampled out from films by FIB micro-sampling method, and were further thin-sliced in a dual beam FIB-SEM (Nova200 Nano-lab, FEI). Sliced cross-sectioned film samples were then transferred to a field emission transmission electron microscope (JEM-2010F, JEOL) for a high resolution imaging with an acceleration voltage of 200 kV.

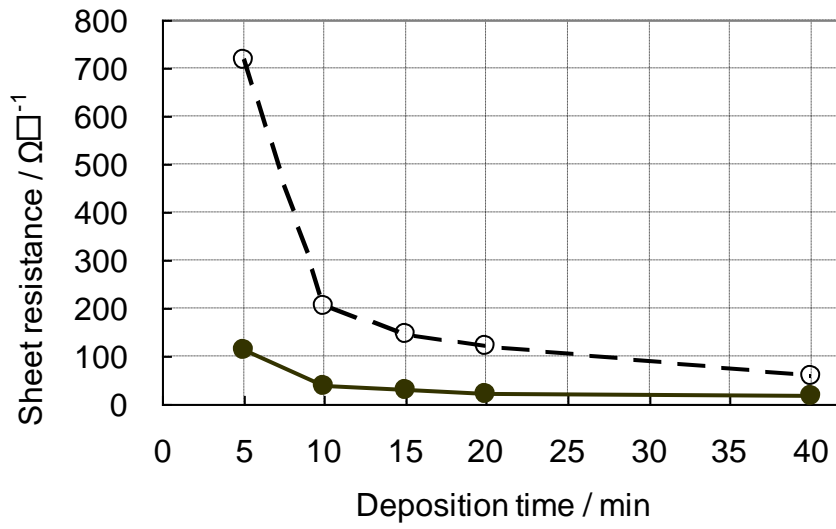
#### **4.2.2 Effect of annealing on thin film morphology and in-plane electrical conductivity**

Thermal annealing was conducted at 550 °C for 1 h in vacuum (with a pressure lower than  $5 \times 10^{-5}$  Torr) in the same chamber used for Ru deposition. Morphology, thicknesses, in-plane electrical conductivities and grain interconnectivities of as-deposited and 550 °C annealed Ru thin film samples are analyzed and compared, following the same methods described in 4.2.1.

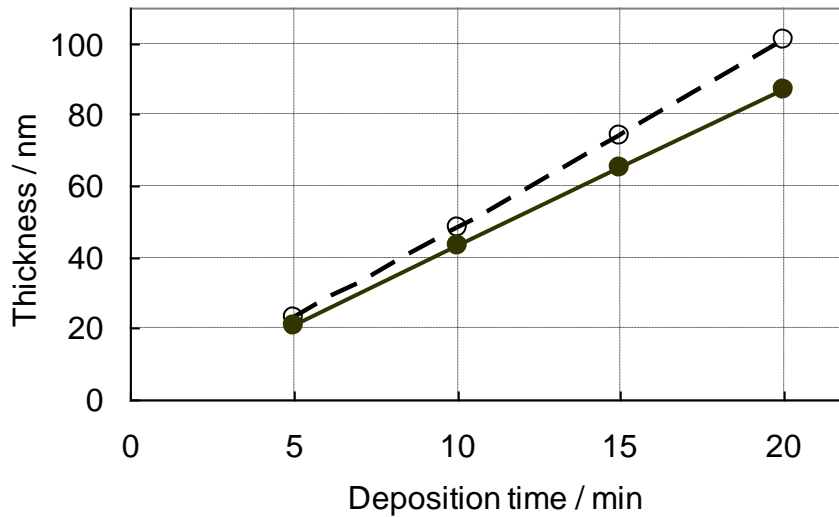
## 4.3 Results and Discussion

### 4.3.1 Ruthenium thin films with different thicknesses

Thickness and sheet resistance of as deposited and 550 °C vacuum annealed Ru thin films on sc-YSZ substrates with different deposition times are shown in **Fig. 4.1 (a)** and **(b)**. The target power was 250 W with chamber pressure of 75 mTorr in Ar. Nominal deposition rates of Ru thin films were  $\sim 4.8 \text{ nm min}^{-1}$ . After annealing, film thicknesses decreased nearly 11 %, while  $\sim 83$  % drop in sheet resistance was observed. Increasing deposition time from 5 to 10 min reduced sheet resistance by more than 70 % for as-deposited films, indicating a critical thickness ( $\sim 24$  to 48 nm) for in-plane conduction path formation. **Figure 4.2 (a) - (d)** show SEM images of as-deposited Ru films with deposition times of 5, 10, 15 and 20 min, respectively. Morphology of these Ru films is highly granular and grain sizes show strong dependence on deposition time. The apparent average grain size of Ru thin films was 10 nm at 5 min, 15 nm at 10 min, 20 nm at 15 min, and 25 nm at 20 min deposition times, respectively. **Figure 4.2 (e)** and **(f)** show SEM images of vacuum annealed Ru thin films with deposition times of 10 and 15 min, respectively. After vacuum annealing, significant grain growths were observed. The average grain sizes were estimated to be 25 nm with 10 min deposited film and 30 nm for 15 min deposited film. Highly granular textures were retained. Film conductivities before and after annealing of different film thicknesses are plotted in **Fig. 4.3**, with comparison to Ru bulk electronic conductivity. A more than an order lower film conductivity observed compared to those calculated from Ru bulk properties is likely due to the still loosely packed granular structure that scatters electrons at grain boundaries.



(a)



(b)

**Fig. 4.1** (a) Thickness and (b) sheet resistance of Ru thin films, as-deposited and annealed in vacuum at 550 °C for 1 h. Open and closed symbols represent as-deposited and annealed thin films, respectively. Films were deposited at 250 W target power and 75 mTorr pressure.

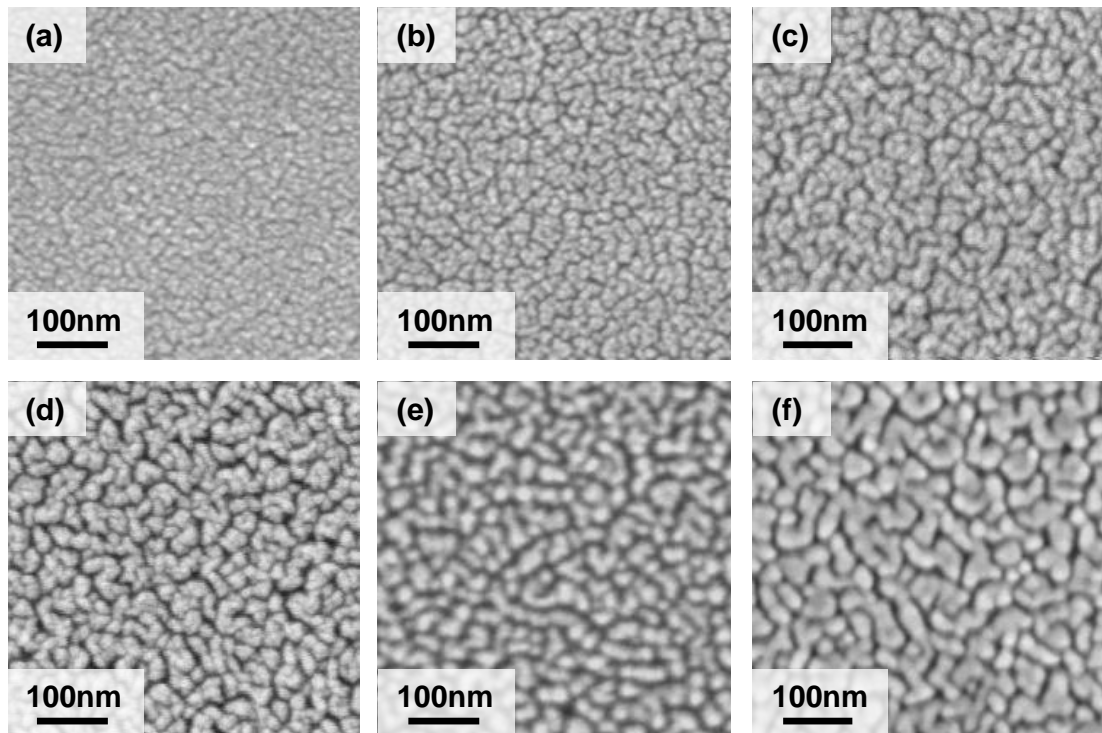


**Fig. 4.2** SEM micrographs of as-deposited Ru thin films on single crystalline YSZ substrates with deposition times of **(a)** 5 min, **(b)** 10 min, **(c)** 15 min, and **(d)** 20 min.

SEM images of 10 min and 15 min deposited Ru thin films underwent 550 °C annealing for 1 h in vacuum are presented in **(e)** and **(f)**, respectively.

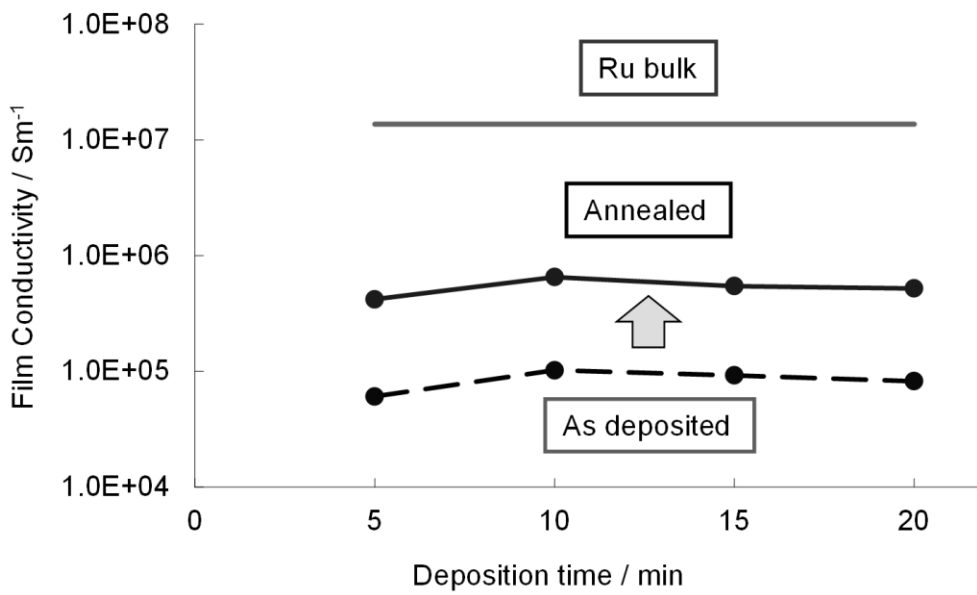


**Fig. 4.3** Film conductivities of Ru thin films on single crystalline YSZ substrates with different deposition times, before and after annealing at 550 °C in vacuum.

Ru bulk conductivity is plotted as a reference.

In order to investigate possible conductivity paths within the Ru films, SEM images of the Ru thin films with various thicknesses were further processed. Binarization of SEM images enables evaluation of the connectivity of Ru grains within the SEM view field. First, SEM images were conditioned to have similar level of contrast and brightness. Subsequently binarization processes were applied using an ImageJ software and grain agglomerates were automatically separated. Following the binarization process, grain agglomerates were manually filled with different colors to allow easier identification of connection and disconnection between the agglomerates. **Figure 4.4** shows conditioned SEM images, binarized images, and color-processed images of (a) 10 min as-deposited, (b) 15 min as-deposited, and (c) 20 min as-deposited Ru thin film, respectively, on single crystalline YSZ substrates. In either deposition condition, there was no single grain agglomerate that connects one side to the other side of the image. However, in-plane electrical conductivities for these films are not zero. This indicates existence of very thin interconnecting Ru layer between the grain agglomerates. As the films grew thicker, the agglomerates grew larger. The apparent Ru surface coverage did not show clear dependence on film thickness, being 66 %, 69 %, and 68 %, for 10 min, 15 min, and 20 min deposited films, respectively. The number of isolated grain agglomerates within the 500 nm x 500 nm SEM image field decreased with increasing film thickness, being 99, 86, and 62, for 10 min, 15 min, and 20 min deposited films, respectively. **Figure 4.5** shows conditioned SEM images, binarized images, and color-processed images of (a) 10 min deposited, and (b) 15 min deposited Ru thin film, respectively, on single crystalline YSZ substrates annealed at 550 °C in vacuum. As listed in **Table 4.1**, the average size of the grain agglomerates grew larger which appeared as a decrease in the number of isolated grain agglomerates, compared to as-deposited samples. Apparent surface coverage increased slightly. As shown in **Fig. 4.1**, the sheet resistance of the films significantly decreases after annealing with decrease in film thickness. However, the grain agglomerates seemed to be unconnected from each other within

the SEM image field, indicating existence of thin interconnecting Ru layers or grain boundaries between the grain agglomerates. A significant decrease in sheet resistance after annealing can be attributed to following factors; first there are fewer grain agglomerates. This allows electrons to travel longer length in the agglomerated grains rather than crossing thin Ru layers or grain boundaries between agglomerates. Second, there are fewer grain boundaries to cross that scatters electrons.

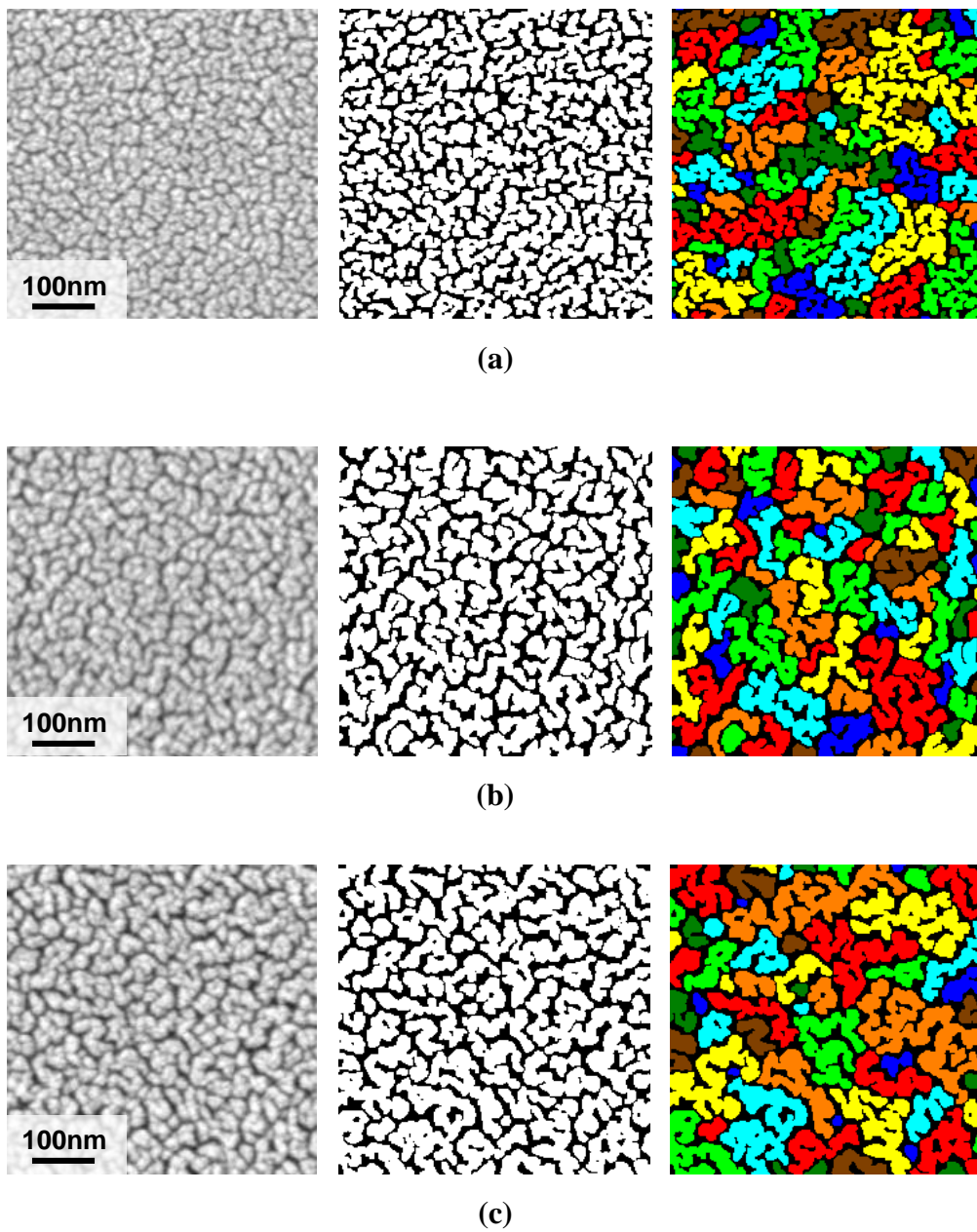


**Fig. 4.4** (From left to right) Conditioned SEM images, binarized images, and color-processed images of **(a)** 10 min as-deposited Ru thin film, **(b)** 15 min as-deposited Ru thin film, and **(c)** 20 min as-deposited Ru thin film, on single crystalline YSZ substrates.

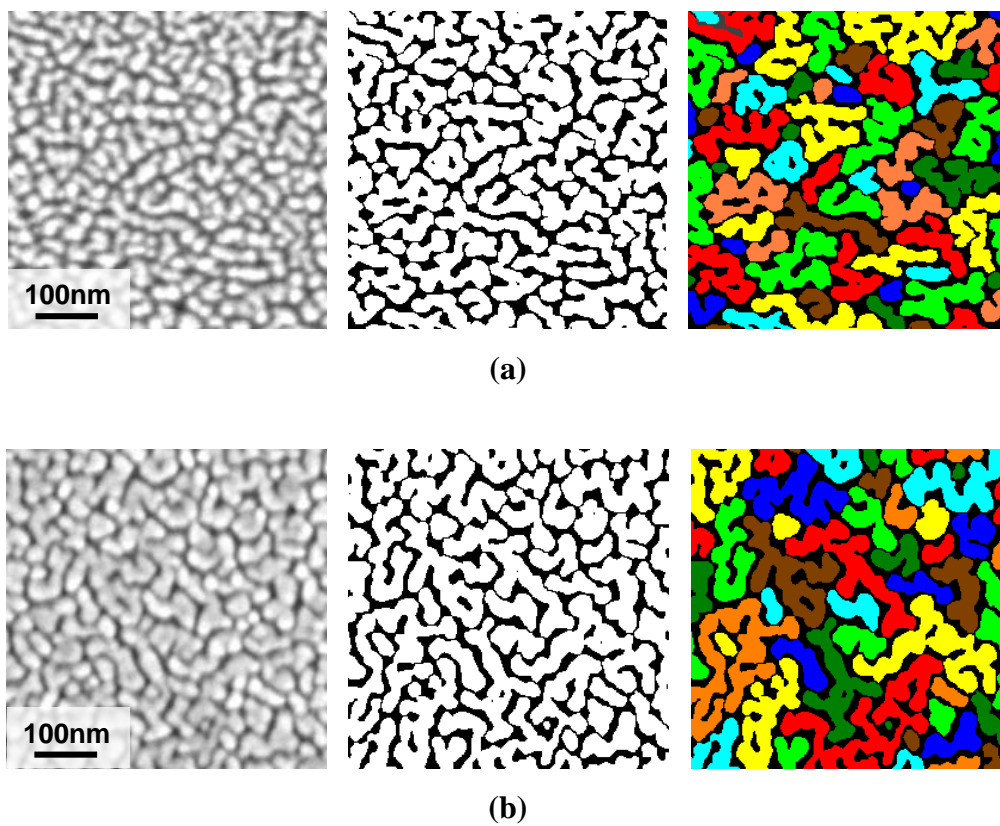


**Fig. 4.5** (From left to right) Conditioned SEM images, binarized images, and color-processed images of **(a)** 10 min deposited Ru thin film, and **(b)** 15 min deposited Ru thin film, on single crystalline YSZ substrates annealed at 550 °C in vacuum.

**Table 4.1** Results of image analysis and measured film conductivity of Ru thin films.

Deposition time / minutes	Film condition	Apparent surface coverage / %	Number of isolated agglomerates	Average size of agglomerates / nm <sup>2</sup>	Film conductivity / mS
10	As-deposited	66	99	1670	4.9
10	Annealed at 550 °C in vacuum	70	69	2530	28.0
15	As-deposited	69	86	2000	6.8
15	Annealed at 550 °C in vacuum	71	52	3410	35.5
20	As-deposited	68	62	2760	8.3

#### 4.3.2 Ruthenium thin films deposited with different pressures and powers

Next, morphology and conductivity of as-deposited Ru thin films on sc-YSZ substrates grown at different deposition pressures and powers were investigated and are shown in **Fig. 4.6 (a)** and **(b)**. The grain size of these Ru films showed strong dependence on deposition power and pressure. Grain size increases with increasing deposition power or decreasing deposition pressure, though it is also sensitive to film thicknesses. At 10 mTorr, film conductivity is relatively high and increases as deposition power is increased. With higher deposition pressures (40 and 75 mTorr) film conductivity becomes relatively low. As film conductivity is strongly related to film porosity (i.e. increased porosity gives lower conductivity), our observations suggest that deposition pressure from above 40 mTorr leads to more porous films. **Figure 4.6 (c)** depicts deposition rates of Ru films deposited at different target power and pressure. Within the controlled parameter range, deposition rate increased with increasing power and with decreasing pressure. The deposition rate ranged from 0.2 nm min<sup>-1</sup> at 50 W and 75 mTorr, to 12.3 nm min<sup>-1</sup> at 200 W and 10 mTorr.

In order to further investigate the effect of deposition pressure on film porosity, XRR data from porous Ru films were inspected in more detail. XRR is a powerful tool for investigating thin film structures. The measurement results are highly sensitive to electron density gradients irrespective of the crystalline nature of the film investigated [86]. Electron densities and thicknesses of thin layers along the direction normal to the specimen surface can be determined by analyzing the XRR patterns. XRR profiles taken from porous Ru thin films are shown in **Fig. 4.7**, where deposition pressure was 40 mTorr for **(a)** and 75 mTorr for **(b)**. Profiles contain critical angles  $\alpha_C$  whose positions give the average electron densities, and interference fringes whose periods give the film thicknesses. The 40 mTorr deposited film was 47 nm thick where 75 mTorr deposited film was 45 nm thick, as calculated from fringe separations in the higher angle regime. The critical angle of incidence  $\alpha_C$  is an angle below which total reflection of x-rays occurs.  $\alpha_C$  can be related to the dispersion term  $\delta$  which appears in the real part of the refractive index  $n$  of the condensed matter as,

$$\alpha_C = \sqrt{2\delta} \quad (4.1)$$

$$n = 1 - \delta \quad (4.2)$$

The dispersion term  $\delta$  is related to the electron density  $\rho_e$  of a condensed matter as follows,

$$\delta = \left(\frac{\lambda^2}{2\pi}\right) r_e \rho_e \quad (4.3)$$

where  $\lambda$  is the x-ray wavelength, and  $r_e$  ( $=2.818 \times 10^{-15}$  m) the classical electron radius. By calculating the electron density  $\rho_{e0}$  of an ideally dense substance from the crystalline structure, corresponding lattice parameters and numbers of electrons in the system, one can derive critical angle  $\alpha_{C0}$  for an ideally dense substance as follows, where  $\delta_0$  is the dispersion term of an ideally dense substance.

$$\alpha_{C0} = \sqrt{2\delta_0} = \lambda \sqrt{\frac{1}{\pi} r_e \rho_{e0}} \quad (4.4)$$

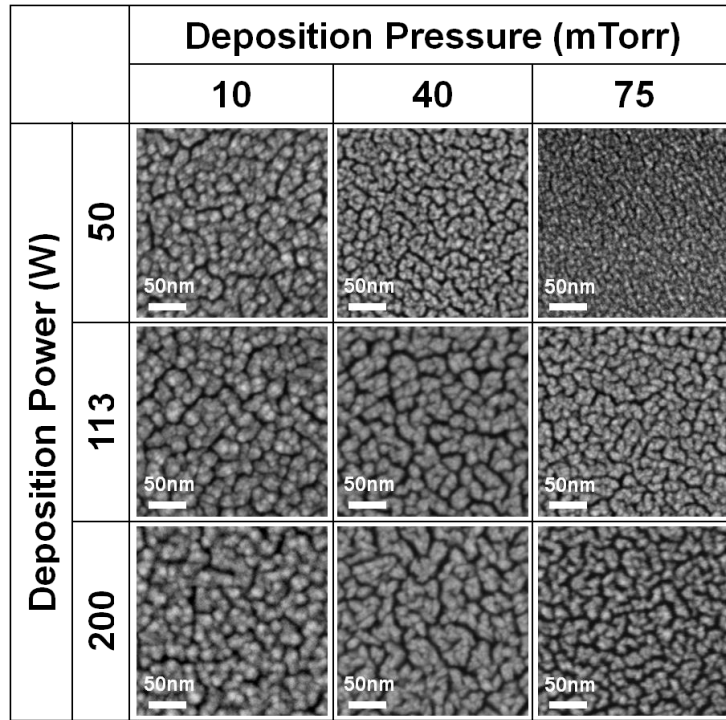
From equations (4.1) and (4.3), the critical angle  $\alpha_{C0}$  of an ideally dense substance and the

measured critical angle  $\alpha_C$  is related to the electron density  $\rho_{e0}$  of an ideally dense substance and the measured film electron density  $\rho_e$  as follows, and film porosity  $\phi$  can be estimated from the ideal electron density and measured electron density using equation (4.6).

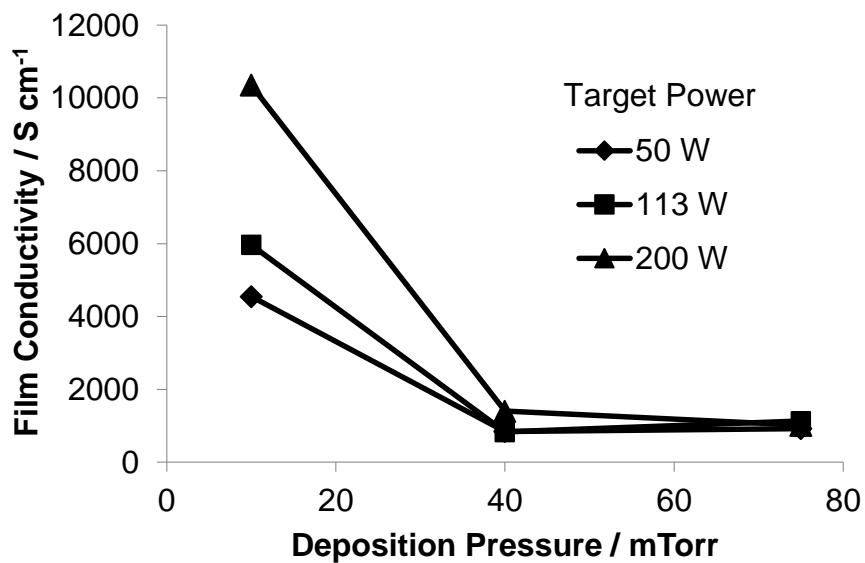
$$\frac{\alpha_C}{\alpha_{C0}} = \frac{\sqrt{2\delta}}{\sqrt{2\delta_0}} = \sqrt{\frac{\rho_e}{\rho_{e0}}} \quad (4.5)$$

$$\phi = 1 - \frac{\rho_e}{\rho_{e0}} \quad (4.6)$$

Ru has a hexagonal close-packed structure with lattice parameters listed on **Table 4.2**. The critical angle  $\alpha_{C0}$  for an ideally dense substance is calculated using equation (4.4) and is 0.476 degrees. The measured critical angle  $2\alpha_C$  of 40 mTorr deposited film was 0.66 deg, where that of 75 mTorr deposited film was 0.62 deg. Film porosities calculated from equations (4.5) and (4.6) are plotted in **Fig. 4.8**. At 40 mTorr the calculated film porosity was ~52 % where at 75 mTorr it was ~58 %. Though in-plane conductivity measurements of the Ru thin films indicated no noticeable difference between 40 mTorr and 75 mTorr deposited films, analysis on the XRR critical angles indicated ~10 % difference in film porosity between the films with these deposition conditions.



(a)



(b)

**Fig. 4.6** (a) Surface morphology (SEM), and (b) DC conductivity measured at room temperature of as-deposited Ru films on single crystal YSZ substrates at various deposition pressures and powers. All SEM micrographs are in same scale in (a).

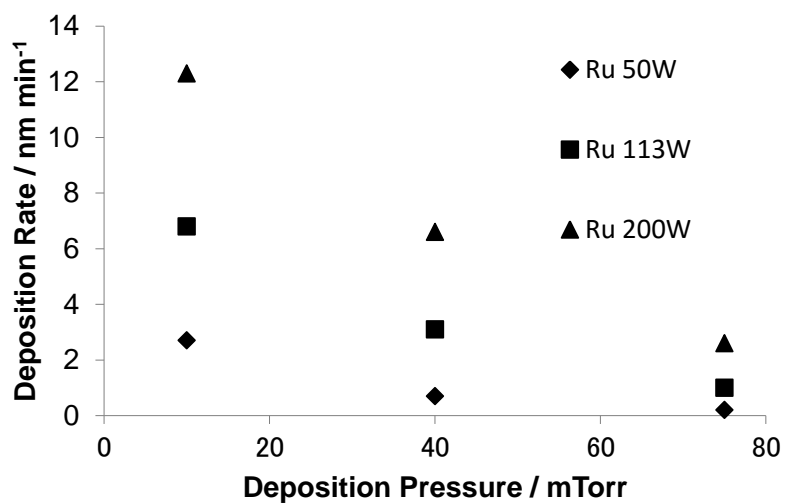
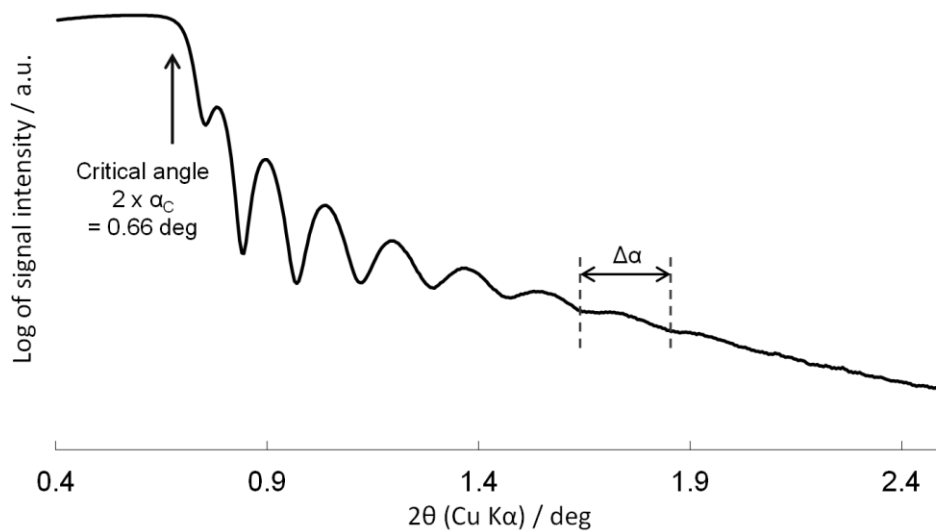


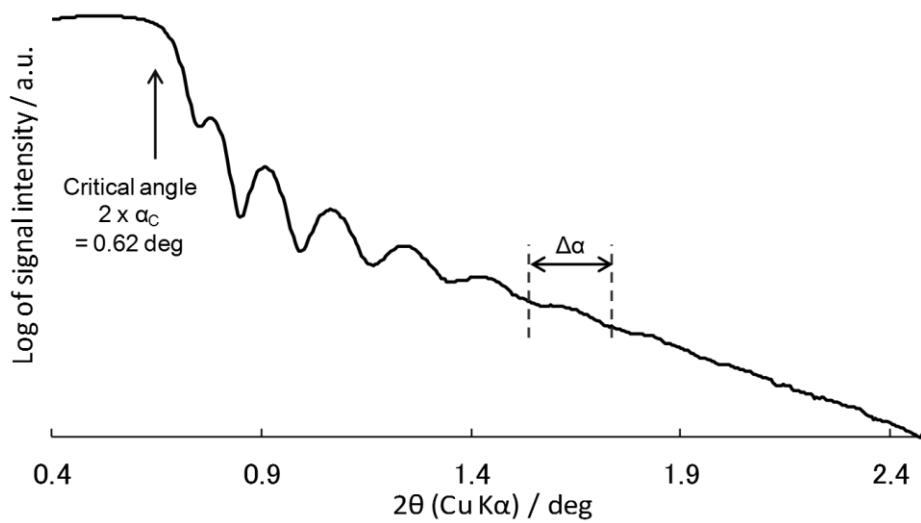
**Fig. 4.6 (c)** Deposition rates of Ru films on single crystal YSZ substrates at various deposition pressures and powers.

**Table 4.2** Lattice parameters and electron densities of Ru hexagonal close-packed crystalline structure.

Cell parameters	
a	2.7059 Å
b	2.7059 Å
c	4.2815 Å
Cell volume	81.45 Å <sup>3</sup>
Number of Ru atoms in one cell	6
Electron density $\rho_{e0}$	$3.24 \times 10^{30} \text{ m}^{-3}$
Critical Angle $\alpha_{C0}$	0.476 deg
Volume per single Ru atom	13.57 Å <sup>3</sup> / atom



(a)



(b)

**Fig. 4.7** XRR profiles measured from porous Ru thin films on single crystal YSZ substrates deposited (a) at 40 mTorr, and (b) at 75 mTorr.

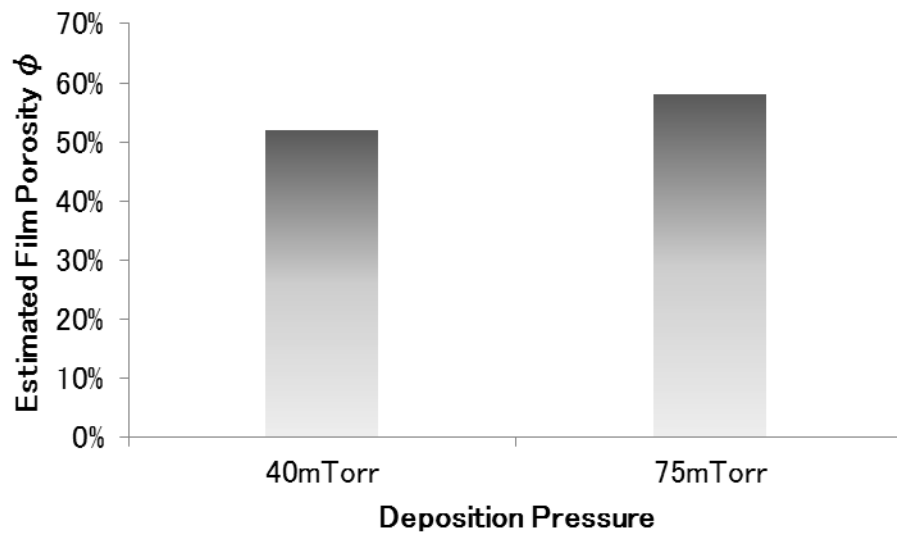


**Fig. 4.8** Film porosities calculated from critical angle measurements of porous Ru thin films deposited at 40 mTorr and 75 mTorr.

### 4.3.3 Microstructures of Ru thin films at the interface with YSZ

Interfacial nano-scale morphology between Ru anodes and YSZ electrolytes is critical in terms of fuel cell performance, because electrochemical reactions are considered to take place at the triple phase boundary between the anode, the electrolyte and the fuel gas phase. In order to obtain a detailed nano-scale morphological understandings on the Ru-YSZ interface, TEM cross-sectional analysis has been applied on Ru thin films deposited on sc-YSZ substrates. **Fig. 4.9 (a) and (b)** show a nano-scale morphology of a Ru thin film deposited at 75 mTorr, RF target power of 250 W for 10 mins. Ru thin films exhibit a columnar structure, where each of the column has a longitudinal length of ~40 nm and a width of ~10 nm. The contrast difference in the columns indicate density variations within the film. Columns show fine nano-crystalline structures with detailed nano-scale morphologies. It is interesting to see a darker layer with a thickness of ~2 nm at the YSZ interface, indicating an existence of a denser Ru layer. The columnar structure seems to have grown on a thin dense layer formed on the YSZ surface.

**Fig. 4.10 (a) and (b)** show a nano-scale morphology of a Ru thin film vacuum annealed at 550 °C for one hour. The annealed film contains columnar but more granular structure compared to an as-deposited film. Longitudinal lengths of columns decreased to ~30 nm, where their widths increased to 25~45 nm. Detailed nano-scale morphology existed in as-deposited column seemed to have disappeared, showing more uniform contrast due to crystal growths and agglomeration of neighborhood columns. Density variation in the film seems to be enhanced, where clear separations between granular columns are observed. The dense thin layer observed at the YSZ surface has disappeared, assumedly due to Ru agglomeration and dewetting. Due to this change at the Ru-YSZ interface where the YSZ electrolyte gets exposed to the gas phase, it is likely that a triple-phase boundary required for electrochemical fuel oxidation is formed.

A cross-sectional TEM image of a Ru thin film on a polycrystalline YSZ thin film is shown

in **Fig. 4.11 (a)** and **(b)**. Deposition pressure was at 75 mTorr, RF target power of 250 W and deposition time for 10 mins. The nano-scale morphology was very similar to those on sc-YSZ, showing a columnar structure with longitudinal length of ~45 nm and width of ~10 nm.

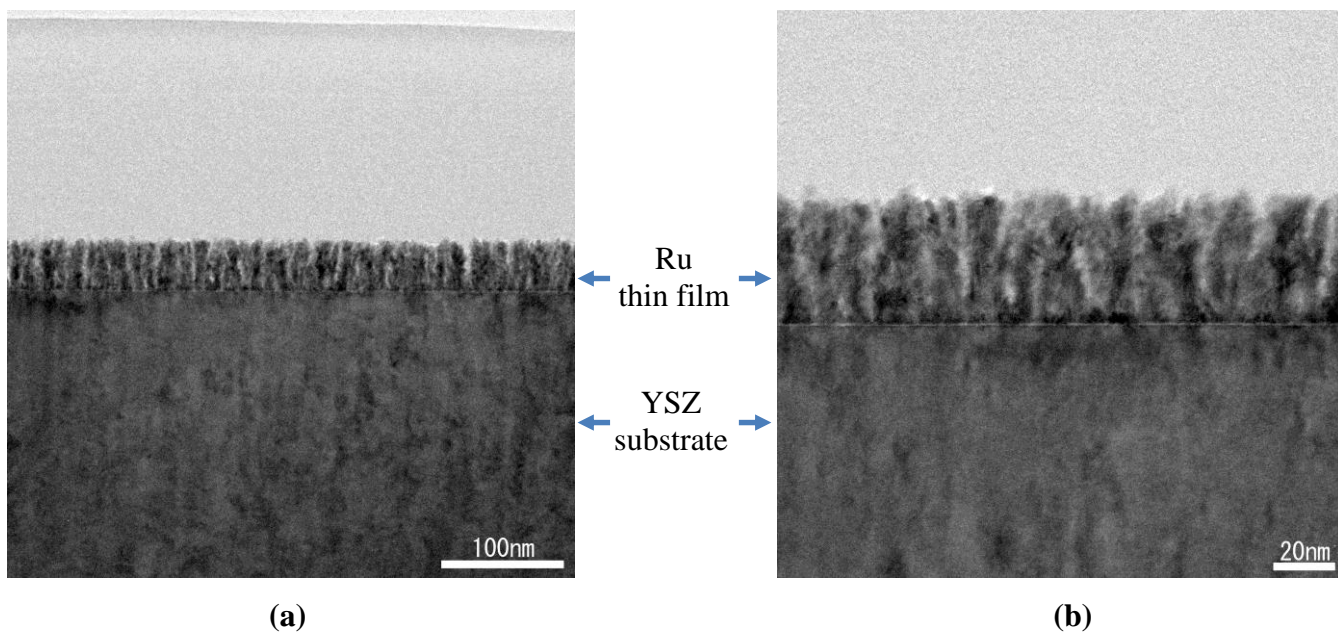


**Fig. 4.9** TEM cross-sectional micrographs of an as-deposited porous Ru films on sc-YSZ substrates at **(a)** 100 nm and **(b)** 20 nm scale. Films were deposited at 75 mTorr, 250 W for 10 min.

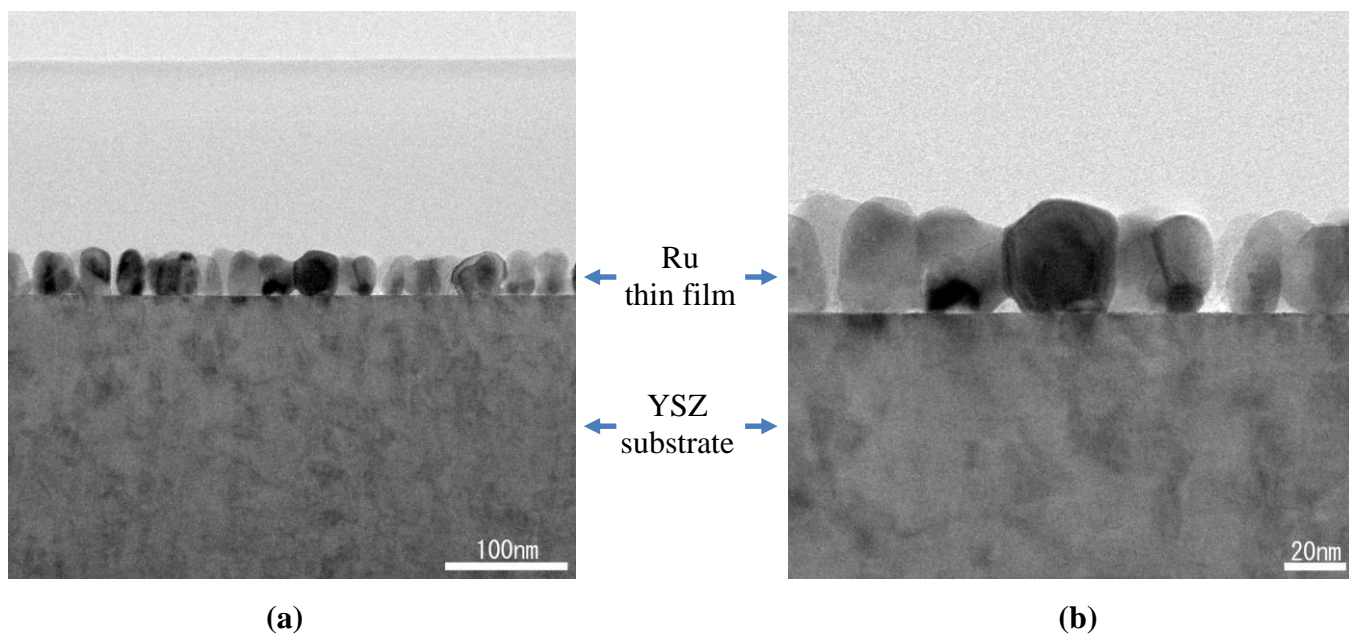


**Fig. 4.10** TEM cross-sectional micrographs of Ru films on sc-YSZ substrates after vacuum annealed at 550 °C, on **(a)** 100 nm and **(b)** 20 nm scale. Films were deposited at 75 mTorr, 250 W for 10 min.

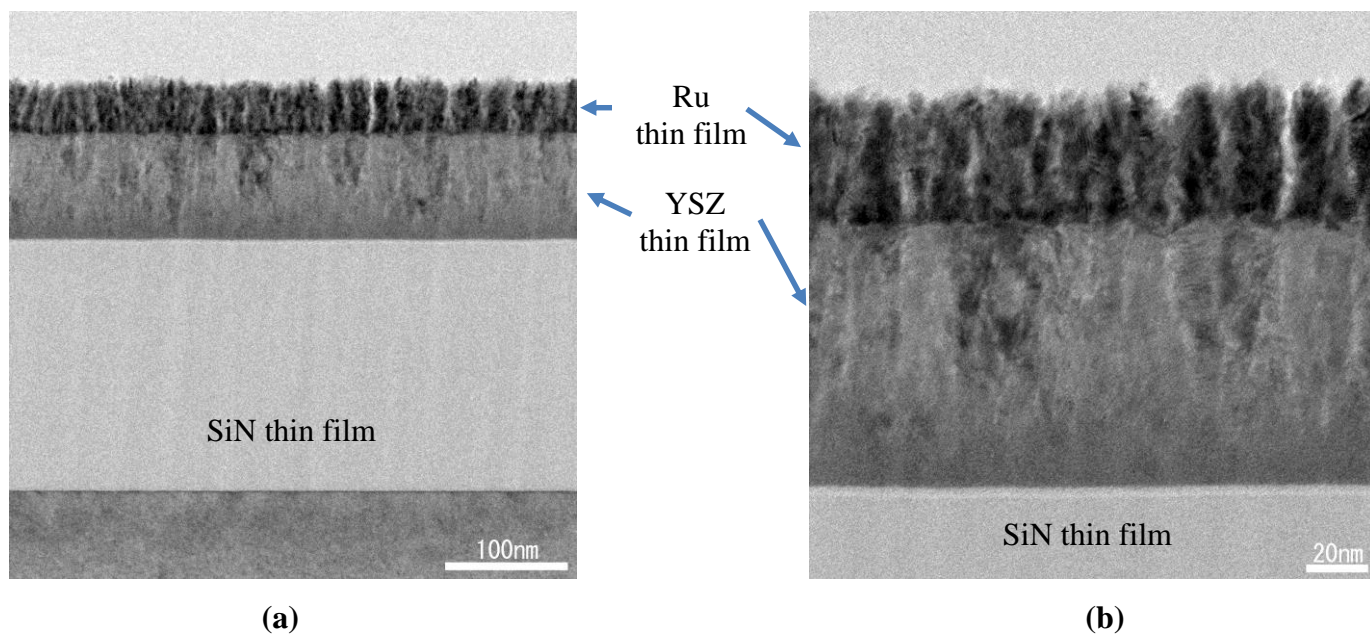


**Fig. 4.11** TEM cross-sectional micrographs of an as-deposited Ru films on thin film polycrystalline YSZ coated Si substrates, at (a) 100 nm and (b) 20 nm scale.

Films were deposited at 75 mTorr, 250 W for 10 min.

#### 4.4 Conclusions

Nano-porous Ru thin films were fabricated by DC sputtering for characterizations towards application as  $\mu$ SOFC anodes. Critical thickness of the Ru thin film for in-plane current conduction path formation was indicated to be  $\sim 50$  nm following in-plane conductivity studies. Grain sizes increased with film thickness and target power, showing highly granular texture. Film porosities of the thin films were highly dependent on deposition pressure, where higher pressure gave higher film porosity as indicated by in-plane conductivity and XRR data analyses. Nano-structural stability under elevated temperature was evaluated through  $550$  °C annealing in vacuum. The porous films showed extensive grain growths from  $10\sim 20$  nm to  $30\sim 40$  nm range, where highly granular texture was retained. At the same time, significant decrease in sheet resistance was observed. Binarization image analysis on planar SEM images of annealed Ru thin films showed that grain agglomerates appears to be still isolated from each other. This indicates that very thin interconnecting Ru layer exists between the grain agglomerates enabling in-plane electron transfer. TEM cross-sectional analysis of Ru thin films on YSZ substrates revealed nano-scale columnar structures with longitudinal lengths of  $\sim 40$  nm and widths of  $\sim 10$  nm. Dense Ru layer with thickness of  $\sim 2$  nm exists covering the YSZ surface. After annealed in vacuum triple phase boundaries were formed with an exposure of YSZ to gas phase, due to agglomeration and dewetting of the Ru thin film while still maintaining nm scale morphologies.

## **Chapter 5: Micro-Solid Oxide Fuel Cells with Nano-Porous Ruthenium**

### **Anodes for Direct Methane Operation**

#### **5.1 Introduction**

Following the basic characterizations, nano-porous Ru thin films were applied on  $\mu$ SOFC platforms as anodes. Fuel cell performance was evaluated through careful engineering of the anode microstructure, with direct supply of 3 % humidified methane as a fuel. OCV and peak power densities of 0.71 V and 450 mW cm<sup>-2</sup>, respectively, were achieved at 500 °C. No carbon deposition was observed in SEM study after fuel cell operation. The evolution of Ru anode morphology under methane and hydrogen operation are compared and discussed.

Next, the  $\mu$ SOFCs were operated with dry natural gas and methane and directly compared [87]. At 500 °C, comparable power densities were obtained. In 3 % humidified natural gas, a peak power density of 800 mW cm<sup>-2</sup> was obtained. Extended constant voltage operation was investigated with methane fuel, where intermittent cell current oscillation was observed. The instability is discussed with regard to oxidation states of the Ru anode catalysts, based on post-operation XPS analysis.

#### **5.2 Experimental Details**

##### **5.2.1 Fabrication and performance evaluation of ruthenium anode thin film micro-solid oxide fuel cells**

Thin film  $\mu$ SOFC platforms with YSZ electrolytes and Pt cathodes were fabricated following the processes described in chapter 2. Porous thin film Ru anodes were deposited on self-supported YSZ/Pt  $\mu$ SOFC platform in Ar at a pressure of 75 mTorr and power of 250 W by DC sputtering without substrate heating. Deposition rates of Ru thin film were calibrated by XRR with a Bruker D8 X-ray Diffractometer in a parallel beam geometry. Fuel cell

performance was evaluated following the procedure described in section 2.4.

### 5.2.2 Post-operation analyses on fuel cells and ruthenium anodes

The morphology of Ru anodes were investigated with SEM before and after the fuel cell measurements in order to look into grain growths, microstructure changes and possible carbon depositions. Cross-sectional sample of a  $\mu$ SOFC was prepared and investigated by Zeiss NVision 40 FIB-SEM after the fuel cell test to investigate the microscopic cell integrity and microstructures of the electrodes and electrolytes.

As-deposited and after methane operation Ru anodes were analyzed by Auger electron spectroscopy (AES) with a Physical Electronics Model 700 Scanning Auger Nanoprobe to further investigate possible carbon deposition from methane decomposition. AES allows elemental analysis with high depth resolution ( $\sim 3$  nm) and lateral resolution ( $\sim 6$  nm). Samples were analyzed in ultrahigh vacuum chamber ( $\sim 10^{-10}$  Torr) which avoids problematic carbon contamination during the measurement.

Oxidation states of Ru anodes were investigated with XPS using a SSX-100 ESCA XPS system equipped with a monochromated Al  $K\alpha$  X-ray source (1.4866 keV) in high vacuum ( $\sim 10^{-8}$  Torr). X-ray photoelectron spectra of the Ru 3d, Ru 3p and Oxygen (O) 1s emissions were obtained with the pass energy at 100 eV and an X-ray spot size of 150  $\mu$ m. The Ru films were grounded to the sample holder to avoid charging effects. The data was fitted with a CasaXPS program package using mixed Gaussian-Lorentzian peak shapes and a Shirley background. The signal intensity of O 1s and Ru 3d spectra was normalized against corresponding Ru 3p peak area. The Ru 3d emission overlapping with the carbon C 1s emission was deconvoluted into contributions from Ru metal, oxide and carbon, considering quantitative relationship between theoretical intensities of Ru 3d 5/2 and 3/2 spin-orbit components. Tabulated sensitivity factors of 7.39 for 3d 5/2 and 5.1 for 3d 3/2 were used. The O 1s emission

was deconvoluted into contributions from different species, while full width at half maximum (FWHM) was limited in a narrow range. Trends in the atomic concentrations of different oxygen species were estimated by comparing the corresponding O 1s peak areas against the Ru 3p peak area using tabulated sensitivity factors, 2.93 for O 1s and 10.2 for Ru 3p.

### 5.3 Results and Discussion

#### 5.3.1 Characterization of ruthenium anodes on micro-solid oxide fuel cells, and fuel cell performance measurements with 3 % humidified methane

**Figure 5.1** shows (a) a schematic of a Ru anode  $\mu$ SOFC with (b) a representative optical micrograph. They are highly buckled as a result of compressive film stresses [57]. The maximum buckling from the horizontal plane is expected to be 5~7  $\mu\text{m}$  [88], the aspect ratio being more than 25~30. **Figure 5.2 (a) - (d)** show SEM images of Ru anodes before fuel cell measurements. Unlike the Ru thin films deposited on sc-YSZ substrates, Ru anode films deposited on self-supported  $\mu$ SOFC electrolytes exhibited island-like morphology. Both the size and number of Ru islands increased with deposition time. After 20 min of deposition, Ru islands still did not contact each other. This island-like morphology has been reported in previous works with Pt and Pd anode thin films deposited by similar techniques in a lithographically patterned structure [85, 89]. This could arise from two factors. Firstly, Ru anodes were deposited inside a geometrically confined Si well, as opposed to the unobstructed flat surface on a sc-YSZ substrate. This may lead to enhanced shading effect that can result in films with columnar morphology [90-92]. Secondly, Ru anodes were deposited on self-supported YSZ - Pt membranes with very small thermal mass to absorb kinetic energy released during Ru sputtering. This may give rise to membrane heating during the sputtering process, leading to agglomeration of deposited Ru particles and result in the formation of island-like morphology.

However, a detailed SEM analysis with a higher resolution revealed an existence of thin Ru layer beneath the larger island-like structure. **Figure 5.3** shows high resolution SEM images focused on underlayers of Ru anodes deposited for (a) 12 mins, and (b) 16 mins. Both samples exhibited island-like structures on the surface similar to **Fig. 5.2**, but at the same time highly granular nano-structures similar to those observed on substrates in section 4.3 were observed at the layer beneath the islands.

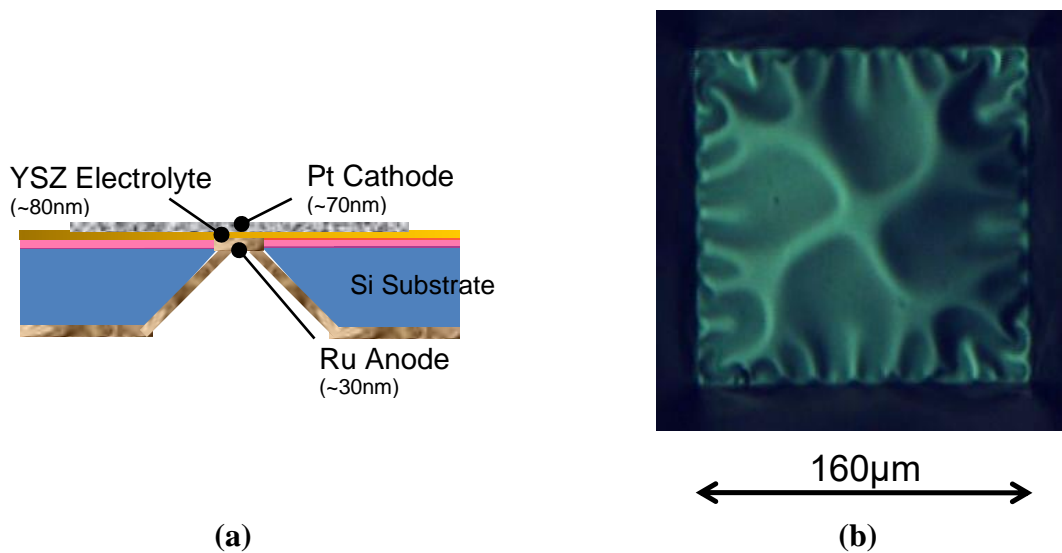


**Fig. 5.1** (a) A schematic of a Ru anode  $\mu$ SOFC, with (b) representative optical micrograph taken from the anode side.

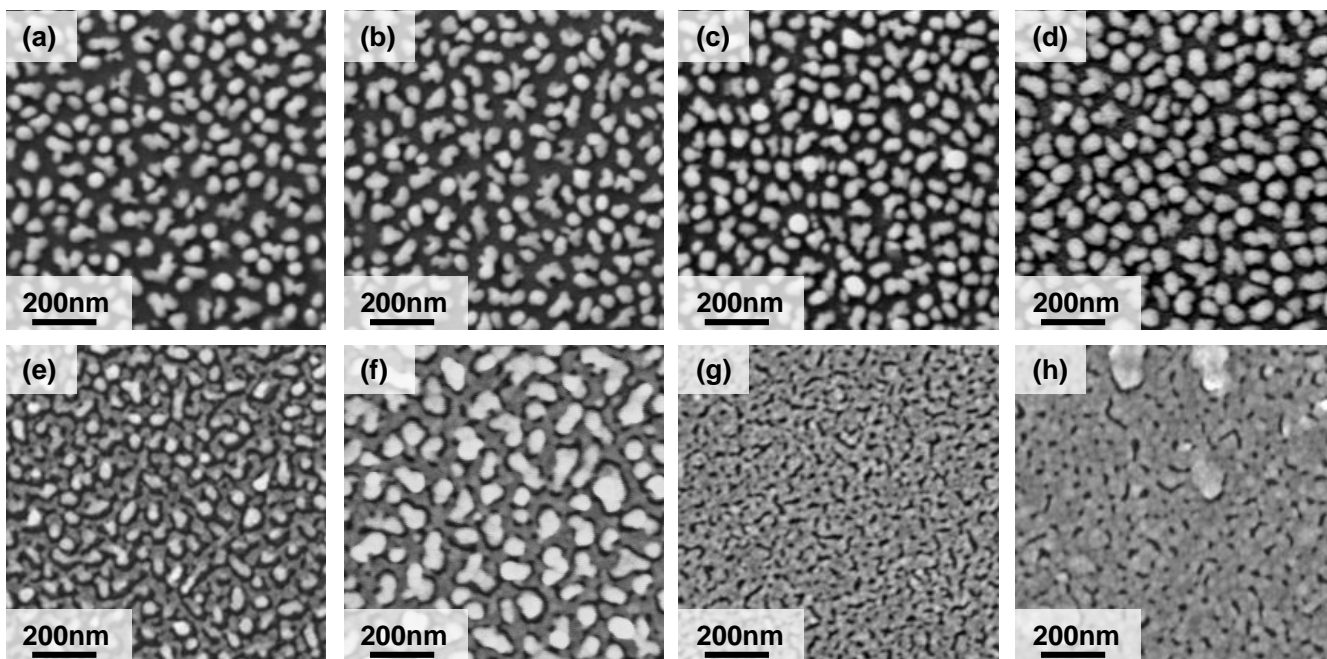


**Fig. 5.2** SEM micrographs of Ru thin films on  $\mu$ SOFC YSZ electrolytes. As-deposited Ru anodes with deposition times of (a) 7.5 min, (b) 10 min, (c) 15 min, and (d) 25 min. Ru anodes after operated with methane, deposition times of (e) 7.5 min and (f) 15 min. Ru anodes after operated with hydrogen, deposition times of (g) 10 min and (h) 15 min.

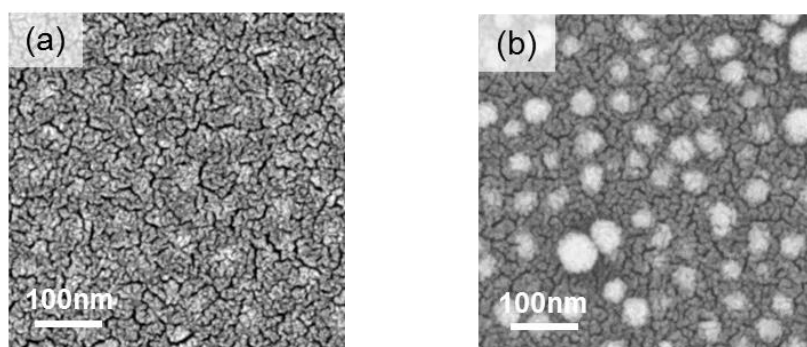


**Fig. 5.3** High resolution SEM micrographs of as-deposited Ru thin films on  $\mu$ SOFC YSZ electrolytes, with deposition times of (a) 12 min, and (b) 16 min.

Fuel cell performance measurements of  $\mu$ SOFCs with Ru anodes deposited for 15 min were conducted with 3 % humidified methane as the fuel and laboratory air as the oxidant. I-V and performance curves of the  $\mu$ SOFC at 400, 450, and 500 °C are shown in **Fig. 5.4**. At 500 °C, a peak power density of 450 mW cm<sup>-2</sup> was obtained with an OCV of 0.71 V, while those at 450 °C were 195 mW cm<sup>-2</sup> and 0.64 V, respectively. The actual active area of this cell was measured by SEM and was 158  $\mu$ m x 155  $\mu$ m. To the best of authors' knowledge, the power density at 500 °C is among the highest performance reported to date for methane-fueled fuel cells operated at equivalent temperatures. For example, a micro-tubular SOFC with methane fuel has displayed 0.3 W cm<sup>-2</sup> at 503 °C, but with internal steam reforming which may induce undesirable thermal gradients within the cell compartment [16]. Peak power densities of  $\mu$ SOFCs operated with 3 % humidified methane with different Ru anode thicknesses (deposition time of 7.5, 15 and 25 min) are shown in **Fig. 5.5**. Deposition time of 15 min gave the optimum thickness of Ru anode to achieve highest peak power density.

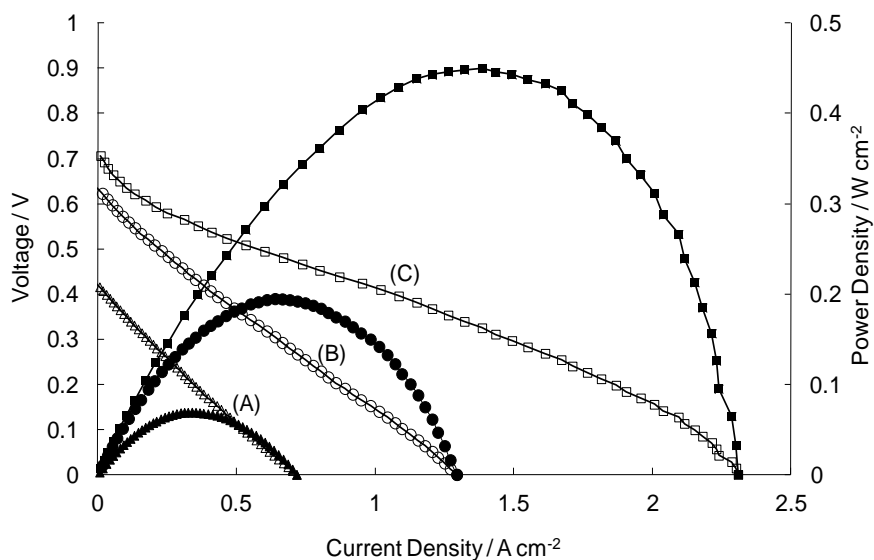


**Fig. 5.4** Performance of a Ru anode/YSZ electrolyte/Pt cathode  $\mu$ SOFC operating at (A) 400 °C, (B) 450 °C and (C) 500 °C with 3 % humidified methane as the fuel. Open and closed symbols represent voltage and power density, respectively.

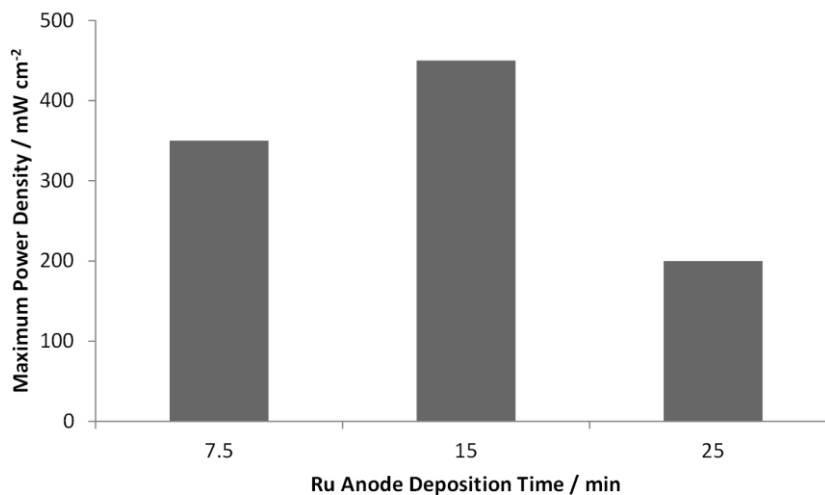


**Fig. 5.5** Peak power densities of Ru anode/YSZ electrolyte/Pt cathode  $\mu$ SOFCs with different Ru anode thicknesses.

The high performance with methane fuel can be attributed to the high catalytic activity of Ru with respect to electrochemical and chemical reactions of methane occurring on its surface. One of the reaction pathways proposed is indirect oxidation, i.e. cracking the methane on the anode followed by the electro-oxidation of the cracked species [12]. This is an exothermic reaction that may be preferred at low operating temperature. In addition, Ru is known to be catalytically active for steam reforming [26-29] and dry reforming [27, 30-32]. With the local coupling of these reactions and its high resistance to carbon deposition, products of cracking and electro-oxidation of methane, H<sub>2</sub>O and CO<sub>2</sub> can be used to reform methane. Hydrogen and CO produced by reforming are consumed as fuels and generate H<sub>2</sub>O and CO<sub>2</sub> in turn, which can be further utilized in aiding reforming reactions, accelerating the overall number of reactions occurring [41]. However, the electrochemical process of methane on Ru anodes could be complicated due to possible reforming and cracking reactions, and multiple intermediate species involved [21]. The results presented here do not provide sufficient evidence for identifying the elementary electrochemical mechanism. As stated above, it is possible that both of these pathways are present in the case of methane reacting on Ru anode, leading to the performance exhibited in this work. The reason for lower OCV compared to the theoretical value may be attributed to following factors: first, our YSZ membrane is very thin (~80 nm) and it is possible that we have pinhole-related electrical or gas shorting between anode and cathode. A second possibility is that methane oxidization is not reaching its equilibrium under OCV conditions. Low OCVs with methane fuel due to low catalytic activity have been reported previously by other groups [21]. Scanning electron microscopy observations of Ru anodes after fuel cell tests in **Fig. 5.2 (e)** and **(f)** showed no visible indication of carbon depositions, such as filaments, sheets or crystals, indicating high carbon deposition resistance of Ru [27]. Scanning electron microscope may not be able to capture trace carbon deposition on the surface, however, if significant amounts of carbon deposition occur, one would expect to see

macroscopic evidence. In order to further investigate possible carbon deposition on Ru surface, AES measurements were carried out on as-prepared and methane operated anodes. **Figure 5.6** (a) shows results from as-prepared anodes, and (b) shows results from methane operated anodes. As Ru Auger peak at 273 eV overlaps with carbon Auger peak at 272 eV, quantitative analysis is not straightforward [93, 94]. However, a qualitative difference in the spectra after methane operation can be observed indicating existence of carbon on Ru surface. The level of the spectra change is minor with still distinguishable Ru peak. This carbon signal may be originating from a couple of nanometers of carbon deposition, or from carbon containing intermediates remaining on Ru surface due to incomplete methane oxidation.

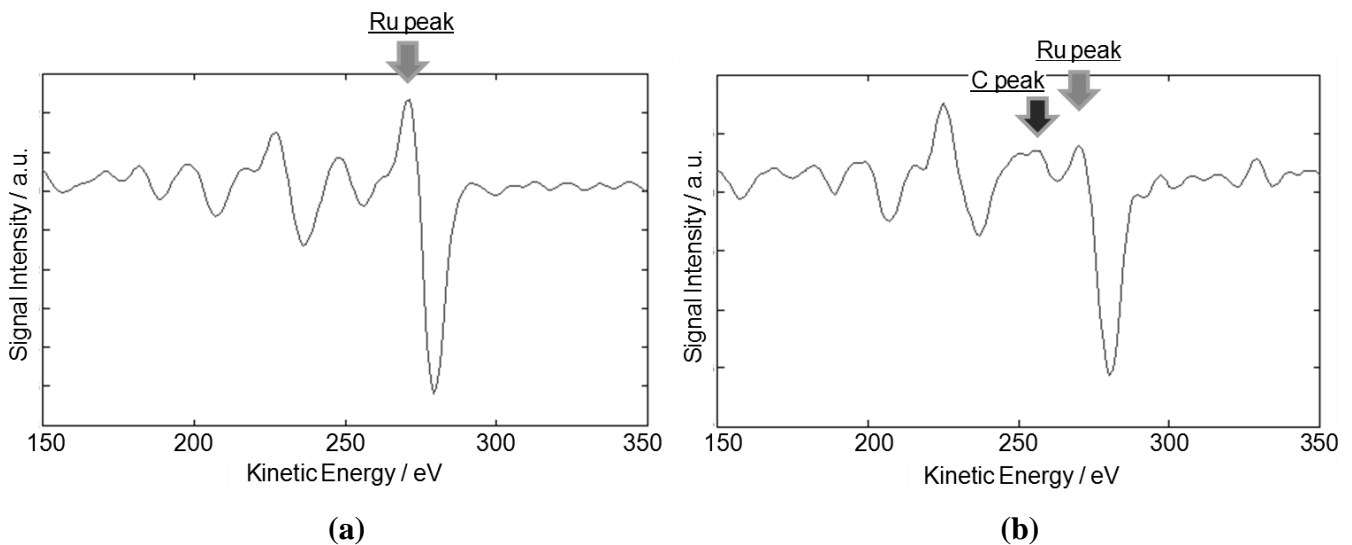


**Fig. 5.6** Auger electron spectroscopy results of Ru anodes from (a) as-prepared  $\mu$ SOFC, and (b)  $\mu$ SOFC operated with methane fuel.

In addition to the qualitative AES analyses, quantitative analyses in XPS data on the Ru anodes before and after fuel cell operations were applied. The Ru 3d core level spectra obtained from Ru anodes are shown in **Fig. 5.7 (a)** as-prepared, **(b)** after operation with dry H<sub>2</sub>, and **(c)** after operation with 3 % humidified methane at 455 °C. They are characterized by a pair of relatively narrow peaks corresponding to the 5/2 and 3/2 spin-orbit components located at 279.0 and 283.2 eV, respectively. It is well known that the C 1s core level spectra from carbon at 284.0 eV closely overlaps with the Ru 3d 3/2 spin-orbit components. However, with a quantitative relationship between theoretical intensities of Ru 3d 5/2 and 3/2 spin-orbit components, one can derive C 1s profiles by appropriately fitting signal contributions from Ru metal (shown in green lines) and oxides (shown in blue lines) , as represented by red profiles in the figures. **Figure 5.7 (d)** shows results of a semi-quantitative analysis on the C 1s intensities. The carbon intensity decreased for more than 70 % after hydrogen operation compared to as-deposited samples, but increased for more than 70 % after methane operation indicating emergence of additional carbon related species. These agree well with AES analyses results, and could be due to a minor carbon deposition or carbon containing intermediates remaining on the Ru surface.

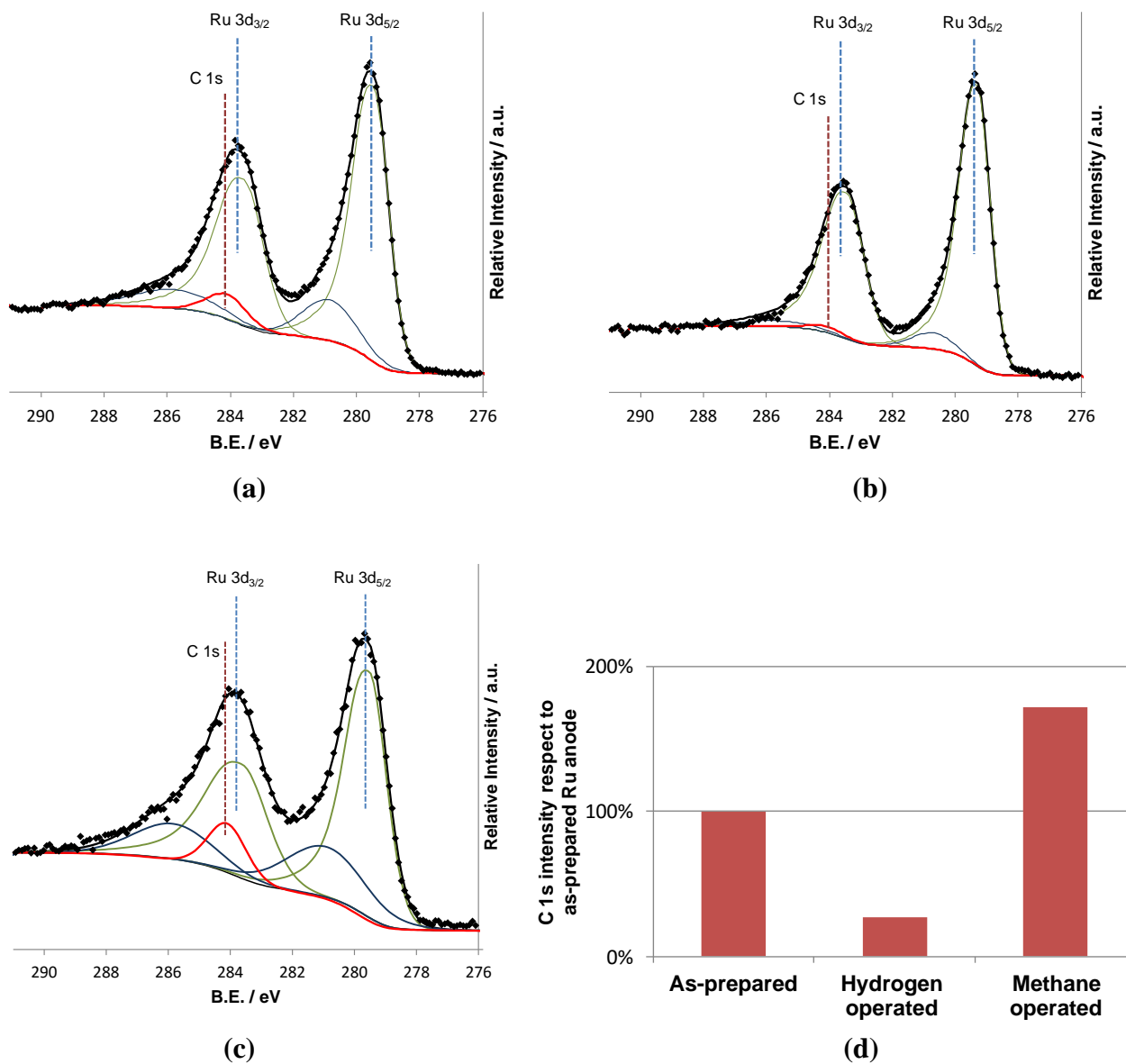


**Fig. 5.7** High resolution Ru 3d spectra recorded from  $\mu$ SOFC Ru anodes by XPS, (a) as-prepared, (b) after operated in dry hydrogen at 455 °C, (c) after operated in 3 % humidified methane at 455 °C, and (d) relative changes of carbon intensity after fuel cell operations.

Good adhesion among the YSZ electrolytes and porous Ru anodes was also observed, as revealed by a FIB cross-sectioned SEM image of a Pt/YSZ/Ru  $\mu$ SOFC after hydrogen fuel cell operation (**Fig. 5.8**). The total cell thickness of the fuel cell is about 180 nm: ~70 nm thick Pt cathodes, ~80 nm thick YSZ electrolyte, and ~30 nm thick Ru anodes. The morphology of Ru anodes was investigated after methane fuel cell testing over 2 hours, showing spreading of Ru particles on YSZ surfaces as shown in **Fig. 5.2 (e)** and **(f)**. These changes under elevated operation temperature are often attributed to the Ostwald ripening process [95]. As seen in **Fig. 5.9**, portions of the YSZ surface became uncovered and formed triple phase boundaries required for electrochemical oxidation reactions. These microstructures are significantly different from those reported for Pt electrodes under hydrogen operation [81, 85, 95]. The original as-deposited island-like structure is retained to a large degree, potentially indicating superior durability and higher flexibility in the microstructure-design of Ru anodes.

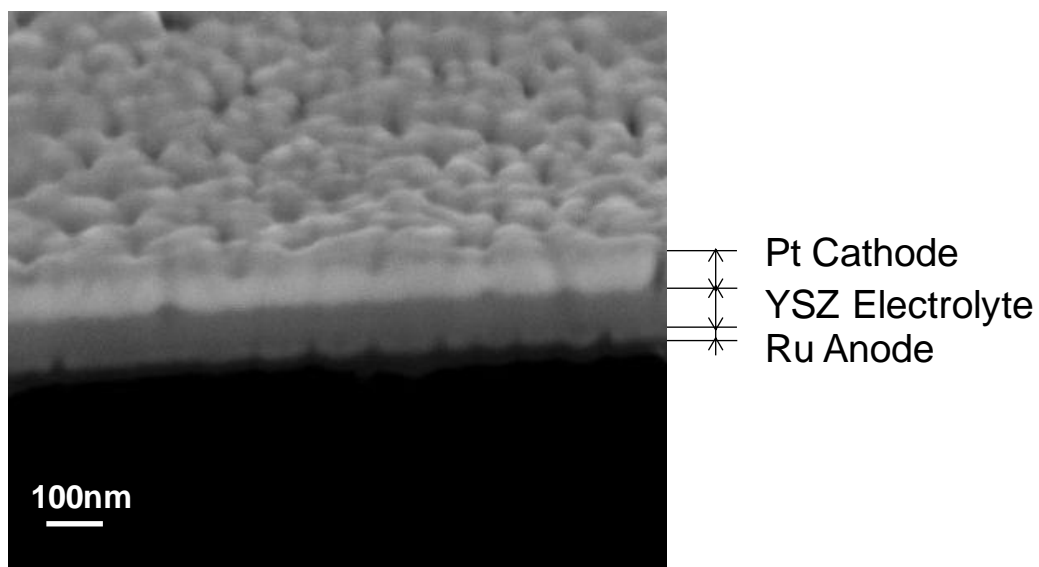


**Fig. 5.8** Focused ion beam (FIB) cross-section SEM image of a Pt/YSZ/Ru  $\mu$ SOFC.

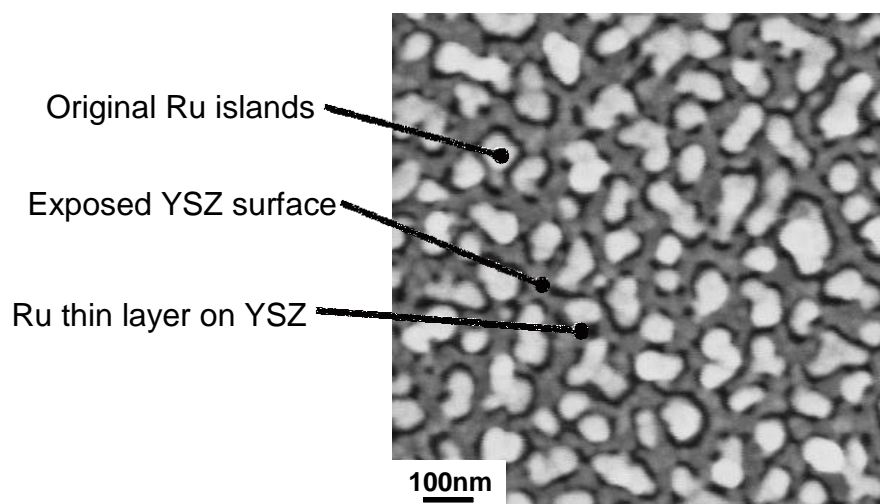


**Fig. 5.9** High resolution SEM micrograph of Ru anodes after methane operation.

We also observed that the morphology of Ru anodes after hydrogen testing is quite different than after methane testing, as shown in **Fig. 5.2 (g)** and **(h)**. As seen, original island-like Ru morphology evolved into porous film-like morphology, indicating accelerated deformation. Although further studies are required for quantitative understanding, we can discuss this distinct morphology difference in light of previous studies. Ye et al. [96] showed that dewetting behavior of Ni during annealing depends on the hydrogen flow rate. Horch et al. [97] reported that hydrogen promotes self-diffusion of platinum. In their report, an activated Pt-H complex was observed, which has a diffusivity enhanced by a factor of 500 relative to other Pt adatoms. Similar behavior has been reported with other precious metal systems [98]. Operation with hydrogen may give higher Ru surface coverage by hydrogen atoms, thus giving higher mobility of Ru atoms leading to an accelerated sub-microscopic deformation, followed by Ru spreading on the YSZ surface. In the case of methane operation, it is likely that decomposed intermediates from methane (such as CO) cover the Ru surface, inhibiting hydrogen trapping on Ru atoms [97].

**Figure 5.10** illustrates evolution of the Ru anode morphology as a function of temperature under different fuels. As-deposited Ru anodes show island-like structure with a thin nano-structured underlayer. As the cell is heated, Ru island-like structure start to spread on YSZ surfaces, and the thin underlayer starts to agglomerate and dewet, exposing YSZ electrolytes to the fuel stream. The temperature at which ripening initiates and rates of spreading strongly depend on the environment of Ru anode proximity. Spreading of Ru at low temperatures is faster in the presence of hydrogen. This is required to establish activate triple phase boundaries. However, excess spreading will decrease the active triple phase boundaries length and decrease the fuel cell performance, as have been reported for  $\mu$ SOFCS with Pt electrodes [85, 95]. Together with its high melting point that suppresses excessive deformation and high activity towards electrochemical reaction of methane, Ru is indeed a promising candidate for further

integration as a direct-methane low temperature fuel cell anode. In addition to the above discussion, we have observed interesting differences in OCV rise during fuel cell start-up. Different behaviors in OCV rise during cell temperature ramp are shown in **Fig. 5.11**. As in the case of Ru anodes on hydrogen, OCV started to increase around 130 °C, and gradually rises to around 0.75 V as shown in **Fig. 5.11 (a)**. This indicates gradual activation of the Ru catalyst towards hydrogen oxidation, and also indicates that electrical connection has been established in this temperature range. On the other hand, abrupt OCV rise to around 0.8 V at 360 °C, which is at much higher temperature than in the case of hydrogen, was observed in the case of methane as shown in **Fig. 5.11 (b)**. Sudden rise at a higher temperature suggests that electrical connection was established at a rate slower than that observed in hydrogen, consistent with the discussion above. As mentioned earlier, it is quite possible that slow ripening and spreading of Ru electrode under methane environment together with its high melting point allowed stable triple phase boundary (TPB) morphology at elevated temperatures, and led to a superior performance.

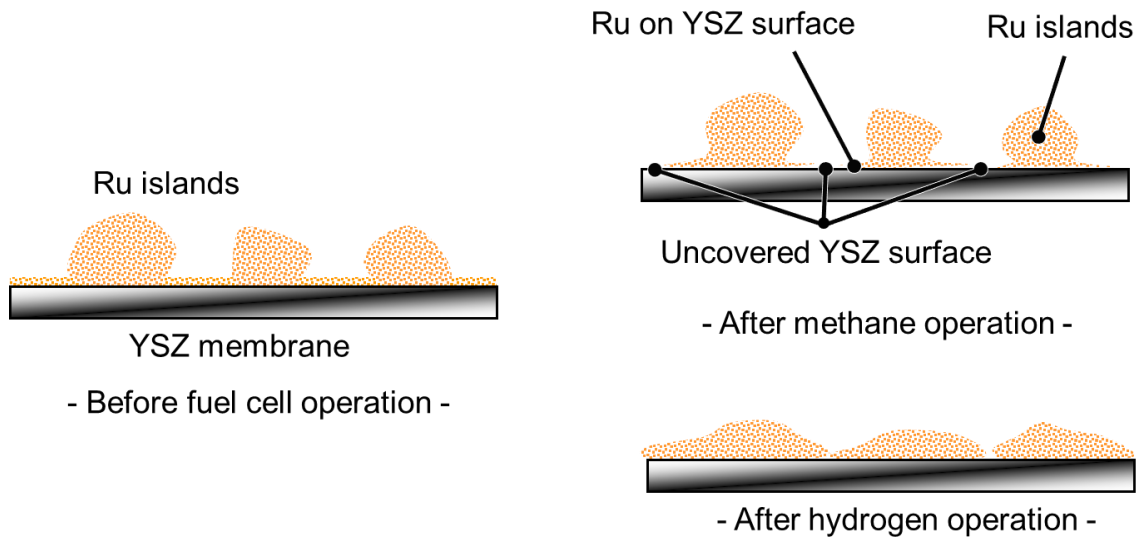


**Fig. 5.10** Illustration of temperature-dependent evolution of Ru anode morphology under different fuels.

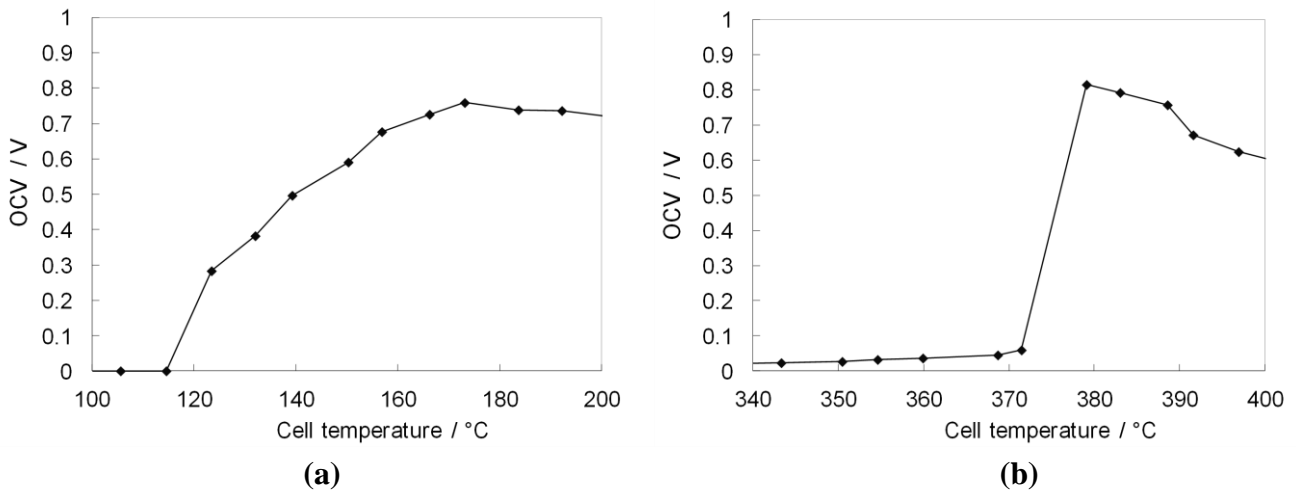


**Fig. 5.11** Temperature-dependent OCV behavior during fuel cell test with (a) hydrogen and (b) methane.

### 5.3.2 Further optimization and fuel cell performance measurements with dry hydrogen, methane and natural gas

Following encouraging initial results from sub-section 5.3.1, further optimizations in fuel cell performance were attempted. A representative optical image of  $\mu$ SOFCs fabricated for this work is shown in **Fig. 5.12 (a)**. A typical effective working area of a  $\mu$ SOFC cell was 200  $\mu\text{m}$  x 200  $\mu\text{m}$  as measured in the SEM. A symmetrical buckling pattern results from residual compressive film stress due to YSZ deposition conditions. These buckling patterns are typically observed in thermal-mechanically stable self-supported thin film  $\mu$ SOFCs [38, 39, 88, 99].

Prior to evaluating the fuel cell performance under different fuels, electrode and electrolyte thicknesses were optimized to maximize the OCV and power density with methane fuel. Porous metal electrodes require sufficient in-plane conductivity and high triple phase boundary density (interface at YSZ electrolyte, metal electrode and gas) [39]. These factors are controlled by the porosity and thickness of the electrode. The electrolyte thickness must also be optimized as thicker electrolytes may prevent electronic and gas leakage, but concurrently lead to higher Ohmic loss [57]. The Ru anode thickness was optimized to  $\sim 50$  nm, YSZ electrolyte to  $\sim 110$  nm and Pt cathode to  $\sim 70$  nm. A typical cross-sectional view of a  $\mu$ SOFC after fuel cell operation is shown in **Fig. 5.12 (b)**. Good adhesion between electrolyte and electrodes is observed without detachment or cracks between the layers.

**Figure 5.13 (a) and (b)** shows OCV, peak power density and I-V characteristics of the  $\mu$ SOFC operated in dry hydrogen fuel, measured from 370  $^{\circ}\text{C}$  to 525  $^{\circ}\text{C}$ . At 525  $^{\circ}\text{C}$ , a peak power density of 305  $\text{mW cm}^{-2}$  was obtained with an OCV of 0.95 V, while those at 450  $^{\circ}\text{C}$  were 102  $\text{mW cm}^{-2}$  and 0.99 V, respectively. With hydrogen fuel, the fuel cell showed high OCV and deliver power from lower temperature regime, i.e.  $\sim 370$   $^{\circ}\text{C}$ . **Figure 5.14 (a) and (b)** shows OCV, peak power density and I-V characteristics of the  $\mu$ SOFC operated in dry methane fuel, measured from 410  $^{\circ}\text{C}$  to 525  $^{\circ}\text{C}$ . The fuel cell demonstrated a maximum power density of 635

mW cm<sup>-2</sup> with OCV of 0.91 V at 525 °C, respectively. The OCV value increases with temperature up to 500 °C, which may be due to the gradual formation of in-plane current collection paths within the porous electrodes during the temperature ramp as observed in a prior work [39]. As the electrolyte in this work is in the nano-meter scale, the OCV is determined by the balance of an electromotive force applied through the active interconnected electrodes and a leak current through the ultrathin electrolyte. Once an interconnect porous network is formed, the OCV becomes stable [57]. Performance of the fuel cell operated with dry natural gas is shown in **Fig. 5.15 (a)** and **(b)**, in the 410~500 °C temperature range. The fuel cell exhibited a maximum power density of 410 mW cm<sup>-2</sup> with OCV of 0.96 V at 500 °C. The OCV slightly decreased by 30 mV when fuel was switched from methane to natural gas, possibly due to impurities present in natural gas. Performance at 530 °C with 3 % humidified natural gas is depicted in **Fig. 5.15 (c)**. Under this condition, the highest power density achieved was 800 mW cm<sup>-2</sup> at OCV of 0.95 V. As a comparison, Wang et al. [24] reported power density of 330 mW cm<sup>-2</sup> at 600 °C with humidified methane and Ru-SDC / Ni-SDC anode. Liu et al. [23] demonstrated power density of 90 mW cm<sup>-2</sup> at 600 °C with humidified natural gas and Ni-YSZ anode. The improvement in the maximum power density by a factor larger than two at lower operation temperatures can be attributed to the use of sub-micrometer scale electrolytes and the high electro-catalytic activity of nano-porous Ru anode toward electrochemical reaction of methane.

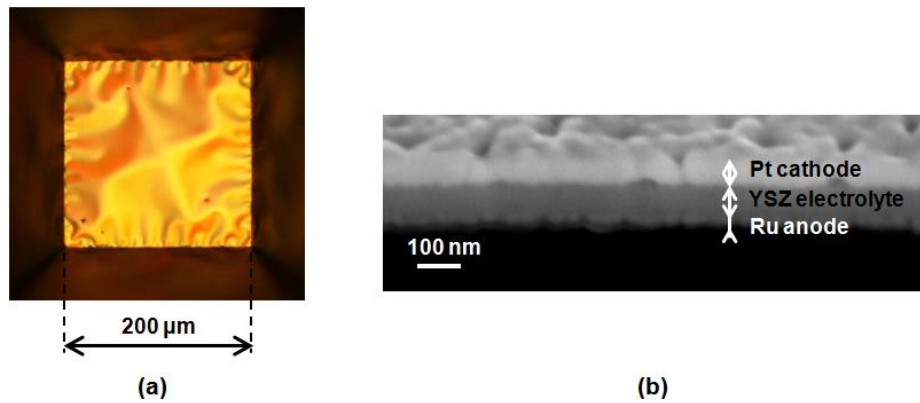


**Fig. 5.12** (a) An optical micrograph of a self-supported  $\mu$ SOFC with nano-porous Ru thin film anodes, taken from the anode side. Buckling is due to the residual compressive stress typical in such membranes. (b) Focused ion beam (FIB) cross-section SEM micrograph of a  $\mu$ SOFC.

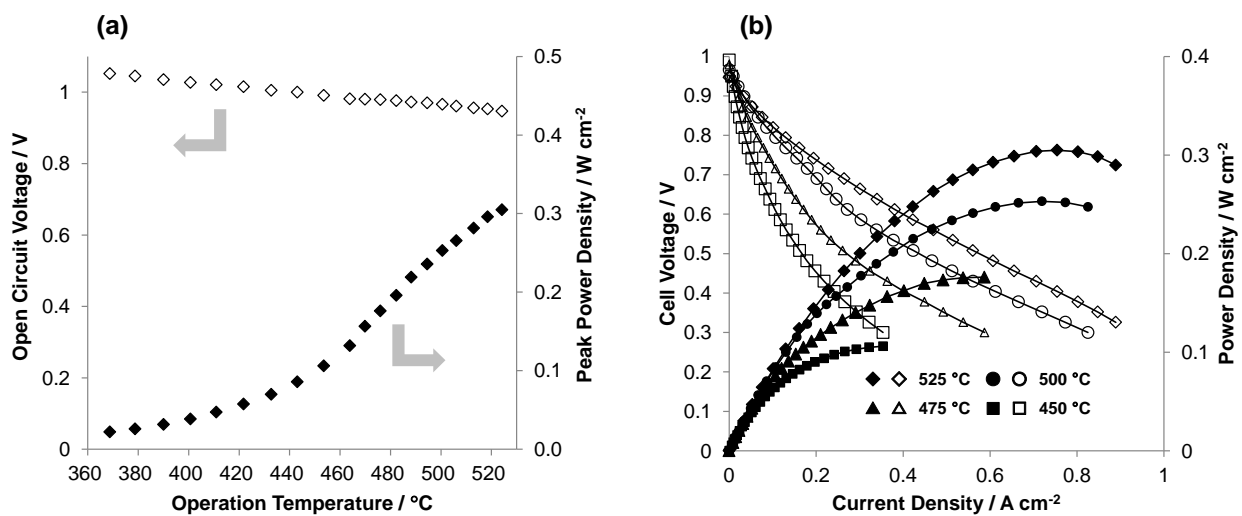


**Fig. 5.13** (a) OCV, peak power density, and (b) I-V characteristics of a Ru anode  $\mu$ SOFC operated with dry hydrogen, measured between cell temperatures of 370  $^{\circ}\text{C}$  and 525  $^{\circ}\text{C}$ .

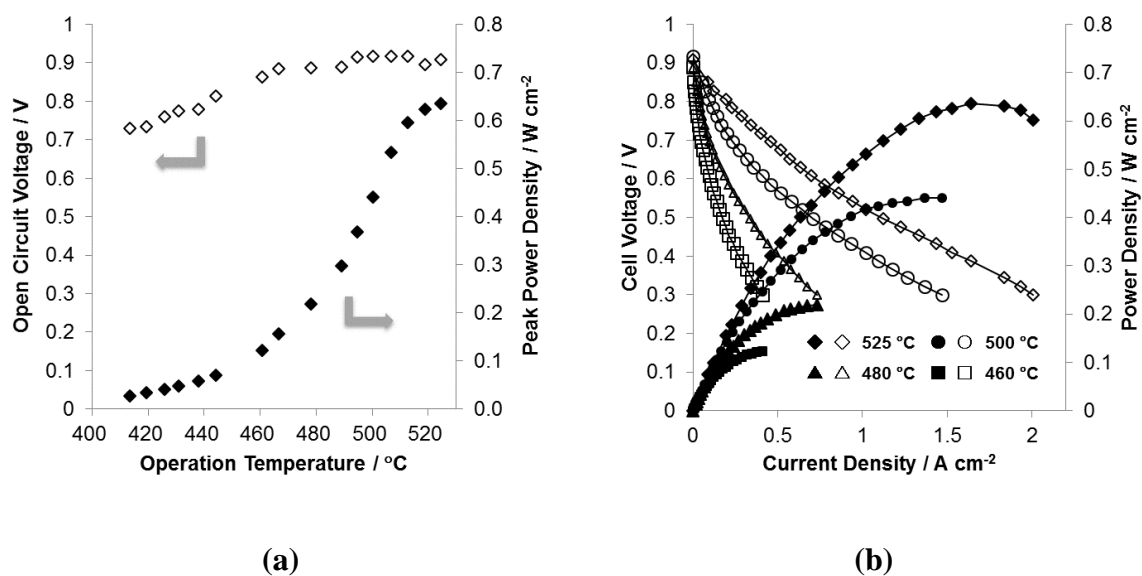


**Fig. 5.14** (a) OCV, peak power density, and (b) I-V characteristics of a Ru anode  $\mu$ SOFC operated with dry methane, measured between cell temperatures of 410 °C and 525 °C.

Highest power density achieved was 635 mW cm<sup>-2</sup> with OCV of 0.91 V at 525 °C.

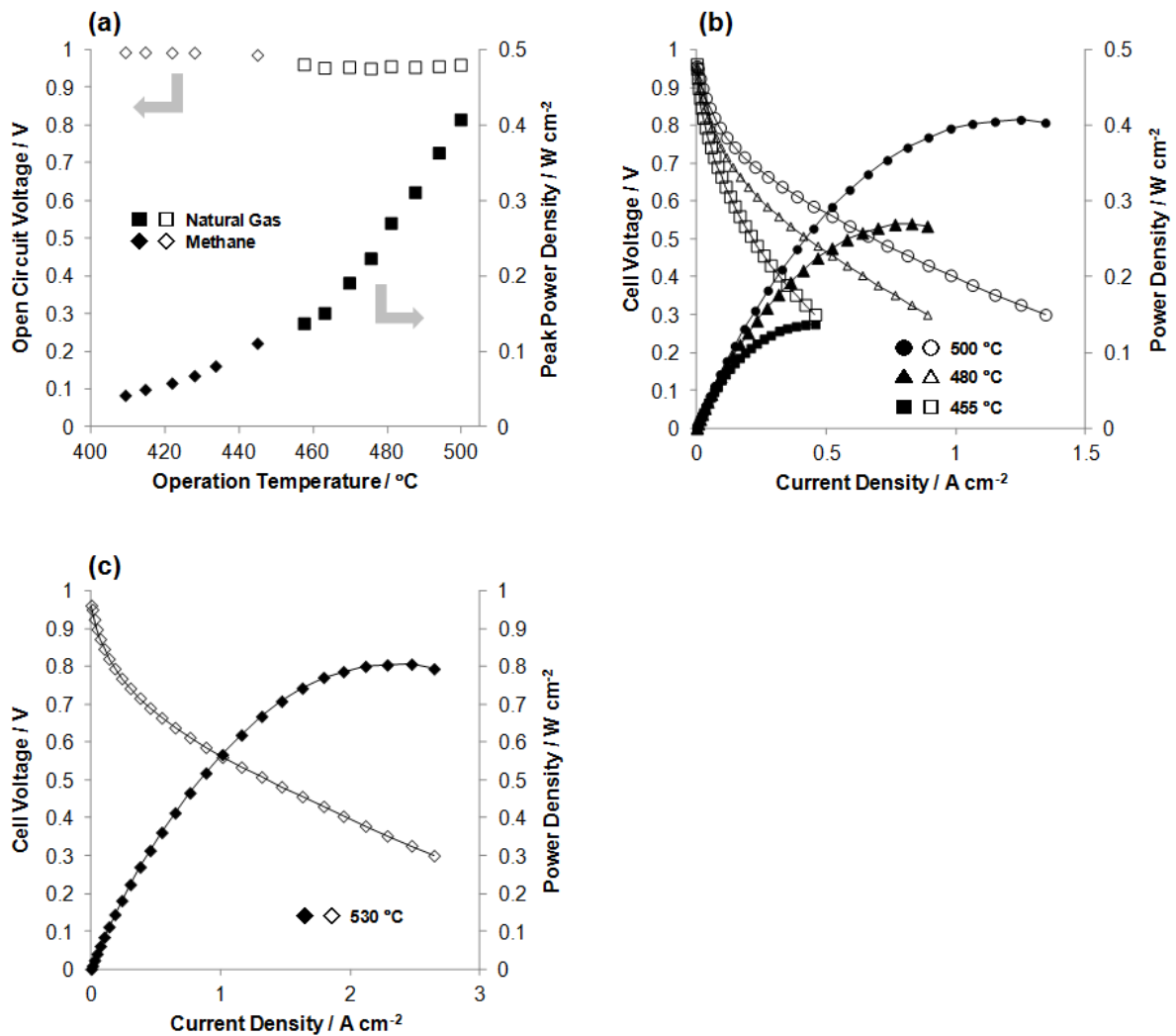


**Fig. 5.15** (a) OCV, peak power density, and (b) I-V characteristics of a Ru anode  $\mu$ SOFC operated with dry natural gas, measured between cell temperatures of 410 °C and 500 °C, and (c) I-V characteristics of a Ru anode  $\mu$ SOFC operated with 3 % humidified natural gas, measured at cell temperature of 530 °C. Highest power density achieved was 410  $\text{mW cm}^{-2}$  with OCV of 0.96 V at 500 °C with dry natural gas, and 800  $\text{mW cm}^{-2}$  with OCV of 0.95 V with humidified natural gas.

Peak power densities with dry natural gas and dry methane at different temperatures are summarized and compared in **Table 5.1**. Peak power densities with natural gas and methane were comparable, suggesting minor effect from additional species present in natural gas on Ru anodes within the period of the measurement. The power densities were comparable to previous results with humidified methane [39]. The reaction of complete methane oxidation is,



The theoretical OCV  $E_T$  for complete oxidation of methane can be calculated from the Nernst equation as follows.

$$E_T = E_T^0 + \frac{RT}{8F} \ln \left( \frac{P_{CH_4} P_{O_2}^2}{P_{CO_2} P_{H_2O}^2} \right) \quad (5.2)$$

where  $E_T^0$  is the standard potential at temperature T, R is the universal gas constant (=8.314 J mol<sup>-1</sup> K<sup>-1</sup>), F the Faraday constant (=96485 C mol<sup>-1</sup>).  $P_{CH_4}$  is the partial pressure of methane,  $P_{O_2}$  of oxygen,  $P_{CO_2}$  of carbon dioxide, and  $P_{H_2O}$  of water vapor, respectively.  $E_T^0$  can be obtained from the Gibbs free energy at temperature T with the following relationship.

$$E_T^0 = -\frac{\Delta G_T^0}{8F} \quad (5.3)$$

The reaction of partial methane oxidation to CO and H<sub>2</sub>O is,



In the case of partial oxidation of methane to CO and H<sub>2</sub>O, the above equations change to the following equations (5.5) and (5.6).

$$E_T = E_T^0 + \frac{RT}{6F} \ln \left( \frac{P_{CH_4} P_{O_2}^{1.5}}{P_{CO} P_{H_2O}^2} \right) \quad (5.5)$$

$$E_T^0 = -\frac{\Delta G_T^0}{6F} \quad (5.6)$$

$P_{CO}$  is the partial pressure of carbon monoxide. Note that the number of electrons involved in the electrochemical reaction changed from 8 to 6. **Figure 5.16 (a)** shows standard potentials of H<sub>2</sub> oxidation, methane complete oxidation and methane partial oxidation calculated from eq. (5.3) and (5.6). At 500 °C the standard potential of H<sub>2</sub> oxidation is 1.06V, methane complete

oxidation 1.04 V and methane partial oxidation 1.01 V. Theoretical OCVs calculated from eq. (5.2) and (5.5) considering Nernst effect of partial pressures of reactant species are shown in **Fig. 5.16 (b)**. Assuming partial pressures of methane equal to 0.97 atm, H<sub>2</sub>O as 0.03 atm, and CO<sub>2</sub> as 0.01 atm, the theoretical OCV for complete oxidation of methane at 500 °C is calculated to be 1.11 V. Assuming partial pressure of CO as 0.01 atm and otherwise the same with the case of complete oxidation, the theoretical OCV for partial oxidation of methane becomes 1.13V. A difference in theoretical OCVs between complete and partial oxidation becomes small. A theoretical OCV with H<sub>2</sub> is 1.04 V, slightly lower than those of methane oxidation reactions. **Figure 5.16 (c)** shows measured OCVs in H<sub>2</sub>, dry methane/natural gas, and 3% humidified methane, with calculated theoretical OCVs of H<sub>2</sub> oxidation and partial methane oxidation. The slope of measured OCVs in H<sub>2</sub> matches well with that of the theoretical value. The difference could be explained by possible existence of minute electronic leakage through nano-metric YSZ electrolytes. OCV with methane and natural gas fuels also followed a similar slope with theoretical OCV of hydrogen fuel. This may be indicating that H<sub>2</sub> is produced by gradual internal reforming and that the dominant electrochemical reaction is hydrogen oxidation. Though OCVs obtained in this work are somewhat lower than the theoretical values, they are similar to those obtained with electrolytes having a thickness two orders of magnitude larger and operated at higher temperature [3, 23, 24].

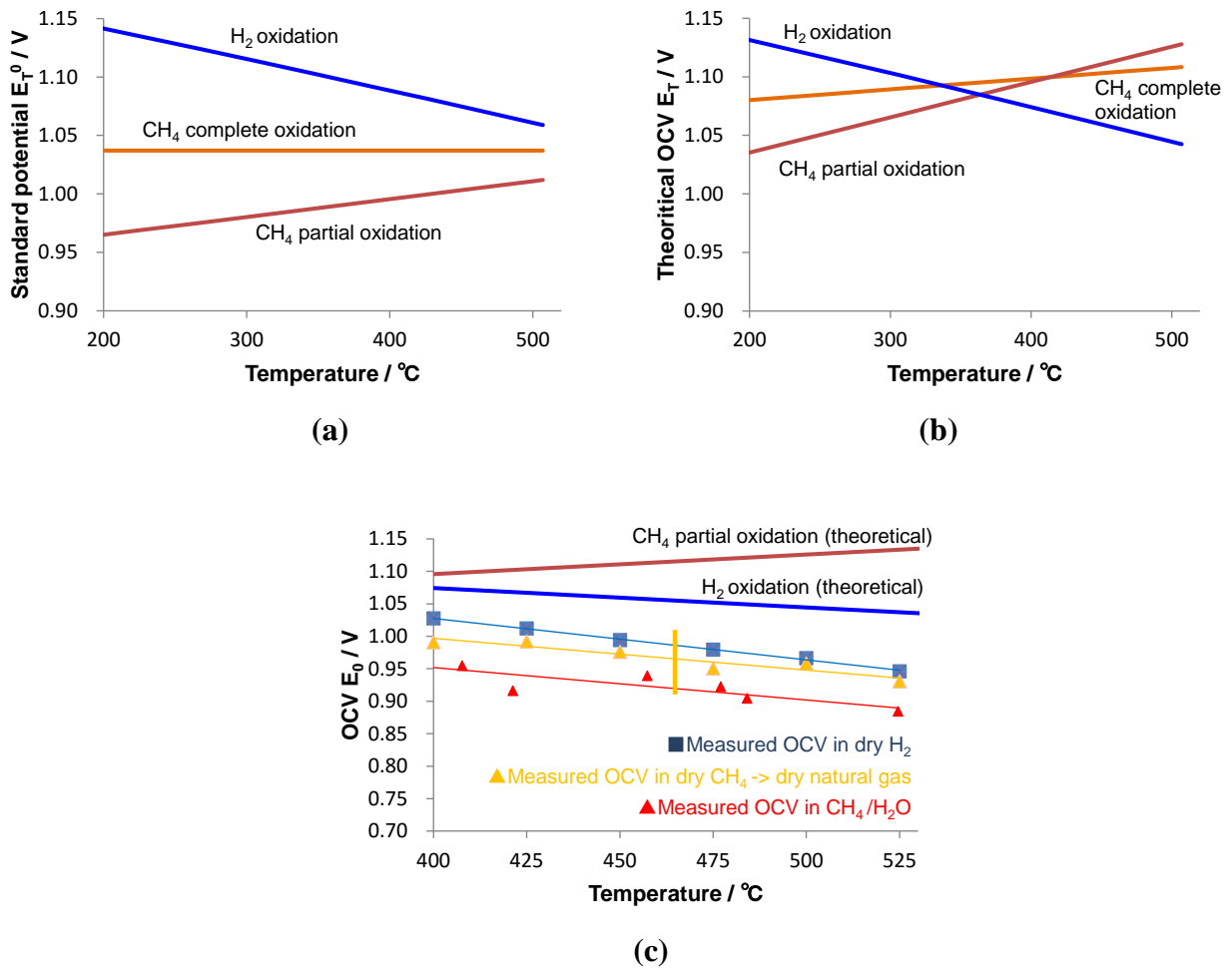


**Fig. 5.16** (a) Standard potentials of hydrogen oxidation, methane complete oxidation and methane partial oxidation, (b) theoretical OCVs considering Nernst effect, and (c) measured OCVs in dry H<sub>2</sub>, dry methane, and 3% humidified methane compared to the theoretical OCVs.

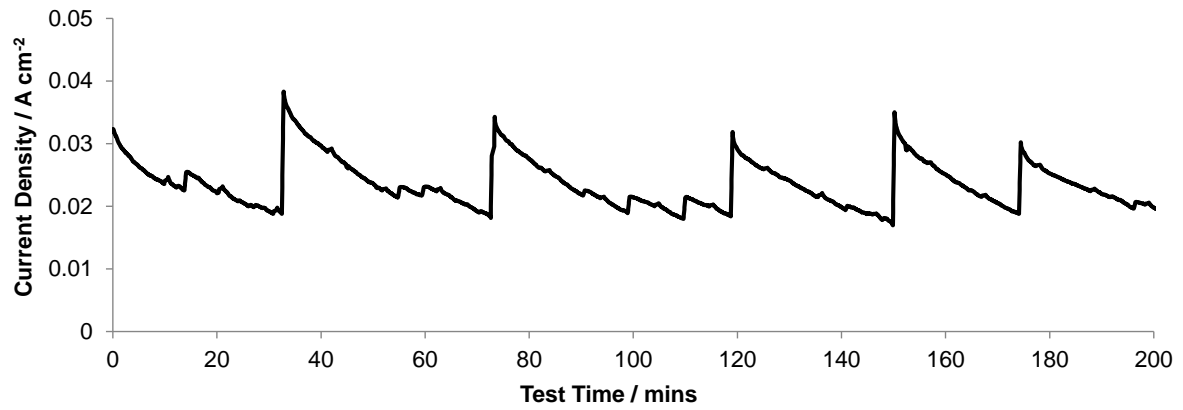
**Table 5.1** Peak power densities of Ru anode  $\mu$ SOFCs at different cell temperatures operated with dry natural gas and dry methane. Power densities were comparable between natural gas and methane.

<b>Cell temperature °C</b>	<b>Peak power density with Natural Gas W cm<sup>-2</sup></b>	<b>Peak power density with Methane W cm<sup>-2</sup></b>
<b>465</b>	<b>0.16</b>	<b>0.14</b>
<b>475</b>	<b>0.22</b>	<b>0.20</b>
<b>485</b>	<b>0.30</b>	<b>0.27</b>
<b>495</b>	<b>0.37</b>	<b>0.37</b>
<b>500</b>	<b>0.41</b>	<b>0.44</b>

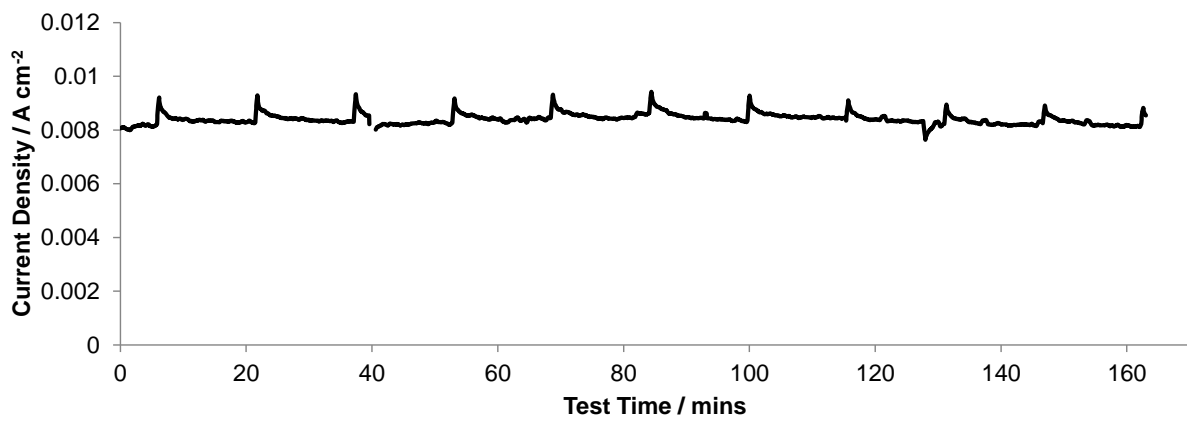
### 5.3.3 Oscillatory characteristics of ruthenium based anode micro-solid oxide fuel cells with methane fuel

Micro-SOFCs with nano-porous Ru anodes were continuously operated at a constant applied voltage of 0.7 V at 455 °C for more than 180 minutes. Fuel cell current evolution during extended operation with 3 % humidified methane as fuel is presented in **Fig. 5.17 (a)**. Quasi-periodic oscillations in the fuel cell current were observed. The periods of the oscillations ranged between 10 to 50 min. One period consisted of a slow current decay followed by a sudden recovery. By operating with dry hydrogen, no quasi-periodic oscillation was observed as shown in **Fig. 5.17 (b)**. Periodic bumps observed in the figure are an artifact due to programmed I-V measurements. Though same methodology was applied at measurements with methane fuel, current bumps were not observed.

Oscillatory catalytic behaviors in methane oxidation have been reported in previous works on RuO<sub>x</sub>-YSZ catalysts [33], palladium-alumina (Pd-Al<sub>2</sub>O<sub>3</sub>) catalysts [100], and Pt doped mixed oxide catalysts [36]. However, the mechanism of the oscillatory behavior is not fully understood. Published works indicate that methane activation and in turn the electrochemical performance is highly dependent on oxidation states of the metal catalyst surface. As for Ru, it is known that reduced metallic sites contribute in methane conversion by partial oxidation while oxidized Ru sites facilitate complete oxidation with lower activity [34]. For example, Bebelis et al. [33] found that the oscillatory behavior observed in methane oxidation over a RuO<sub>x</sub>-YSZ electrode is related to transitions between different oxidation states of Ru. The surface oxidation state of the electrode was correlated to the anode potential, a more negative potential indicating a lower surface oxygen activity and a higher degree of reduction, also showing improved electro-catalytic rate and higher selectivity to partial oxidation.



(a)



(b)

**Fig. 5.17** Fuel cell current history of nano-porous Ru anode  $\mu$ SOFCs with  
**(a)** 3 % humidified methane as fuel, at cell temperature of 455 °C, and cell voltage of 0.7 V,  
and **(b)** with dry H<sub>2</sub> as fuel, at cell temperature of 455 °C, and cell voltage of 0.7 V.

In order to investigate fuel effect on Ru oxidation states, XPS measurements were carried out on the Ru anodes with different fuel cell operation histories. Ru 3d core level spectra obtained from Ru anodes after operation at 455 °C are shown in **Fig. 5.7**. Dry hydrogen operation has two effects on the appearance of the spectra as shown in **Fig. 5.7 (b)**. Ru 3d peaks appear sharper with a decrease in FWHM, and peaks showed shifts to lower binding energy (B.E.) direction. These are due to decreased signal from oxidized Ru species with higher B.E., compared to an as-prepared sample as shown in **Fig. 5.7 (a)**. On the contrary, after operation in 3 % humidified methane the spectra showed increase in FWHM with a shift to higher B.E. as shown in **Fig. 5.7 (c)**, indicating further oxidation of Ru surface. Next, XP spectra from the oxygen related species were investigated in detail. High resolution O 1s core spectra recorded from Ru anodes are shown in **Fig. 5.18 (A)** as prepared, **(B)** after operation with dry hydrogen at 455 °C, and **(C)** after operation with 3 % humidified methane at 455 °C. The influence of the fuel on the oxidation state was investigated by deconvolution of O 1s spectra. Based on previous reports, the component at lower binding energy (529.1 +/- 0.3 eV) is attributed to O<sup>2-</sup> species [101-103]. For metallic oxides such as RuO<sub>2</sub>, final state effect gives rise to an asymmetry in the O 1s core level spectra [101, 104-106]. The O<sup>2-</sup> component was therefore fit with an asymmetric tail at high binding energies. Other components were fit with typical Gaussian-Lorentzian peak shapes. The higher binding energy component at 530.8 +/- 0.3 eV is attributed to OH<sup>-</sup> species [104, 107, 108], which likely originates from water produced by fuel oxidation or from those present in the humidified fuel feed. The spectrum from a sample operated with methane (**Fig. 5.18 (C)**) shows a third component at 532.2 eV. This component has been observed by O'Grady et al. [109], Sharma et al. [110], and Shen et al. [111]. Kim et al. [101] attributed it to be due to the presence of absorbed water and/or oxygen containing compounds such as CO. Foelske et al. [107] attributed this peak to surface adsorbed H<sub>2</sub>O. We extended our analysis by comparing the O 1s core spectra from Ru anodes operated with

humidified fuels at higher temperature. The XP spectra from Ru anodes are shown in **Fig. 5.19** (A) as-prepared, after operated with (B) 3 % humidified hydrogen, (C) with 3 % humidified methane, and (D) with 3 % humidified natural gas, at 530 °C. The peak at 532.2 eV was not observed after operation with humidified hydrogen, but appears only after operation with methane or natural gas. This suggests that the peak is not related to the presence of adsorbed water but rather, is due to oxygen containing compounds such as CO, or other intermediate products of the methane oxidation. The results of analyses on surface oxygen species after operation with different fuels are summarized in **Fig. 5.20**. Oxygen species detected on the Ru anode surface after fuel cell operations are strongly affected by the fuel that is used to operate the cells, as summarized below:

- 1) Operation with hydrogen reduces the Ru electrode surface and the O<sup>2-</sup> peak intensity as seen in **Fig. 5.18 (B)**. Hydrogen is highly reactive with oxygen species and cleans the Ru surface by reacting with surface oxygen. When humidified hydrogen is supplied at 530 °C, a stronger OH<sup>-</sup> peak is observed as shown in **Fig. 5.19 (B)**. OH<sup>-</sup> species may originate from H<sub>2</sub>O added in the fuel stream and from fuel oxidation. No appearance of the higher binding energy peak (532.2 eV) was observed.
- 2) Operating with methane or natural gas significantly increases the O<sup>2-</sup> component intensity as shown in **Fig. 5.18 (C)**, **Fig. 5.19 (C)** and **(D)**. There appears to be greater amount of oxygen coverage on the Ru surface due to favored oxygen adsorption relative to methane under the experimental conditions. The peak at 532.2 eV appears and is related to CO or other oxygen related intermediates of methane oxidation. No significant difference in photoelectron spectra was observed between anodes operated with methane (**Fig. 5.19 (C)**) and natural gas (**Fig. 5.19 (D)**). No sulfur related peak was detected.

In order to evaluate Ru oxidation potential, oxygen partial pressure required for oxidation is investigated via Ellingham diagram. **Figure 5.21** shows (a) partial pressure of oxygen, and (b) calculated anode potential, respectively, required to oxidize Ru under standard states. The anode potential needs to be as high as 0.6 V at 500 °C, which is not likely under fixed cell voltage of 0.7 V. Thus, the Ru oxidation needs to be attributed to the weak reducing activity of methane at this temperature [34], and to an ionic flow of oxygen from the cathode due to a potential difference in the cell, in addition to the moderate anode potential.

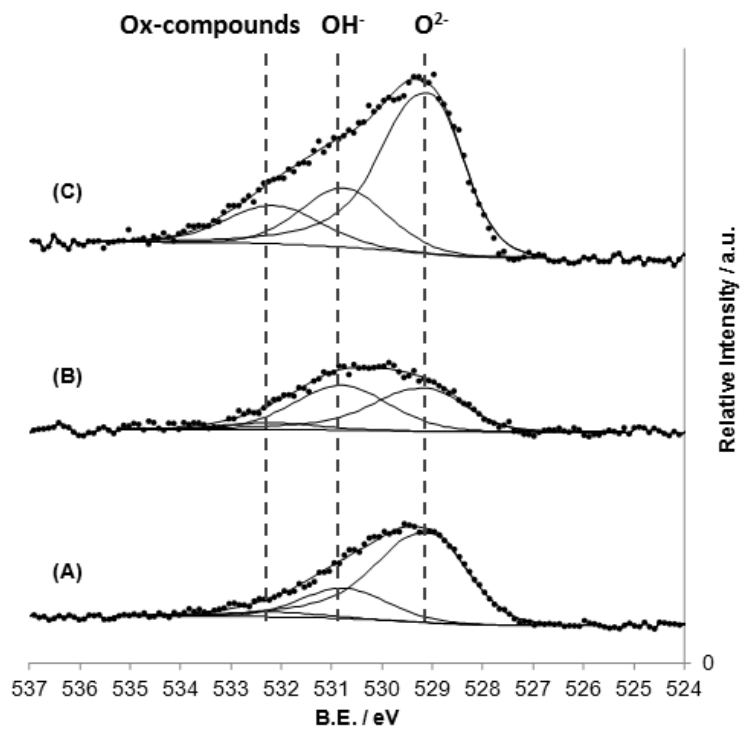


**Fig. 5.18** High resolution O 1s spectra recorded from  $\mu$ SOFC Ru anodes by XPS, (A) as prepared, (B) after operated with dry hydrogen at 455 °C, and (C) after operated with 3 % humidified methane at 455 °C. Intensity of O<sup>2-</sup> peak centered at 529.1 eV increased after methane operation with appearance of the third peak at 532.2 eV.

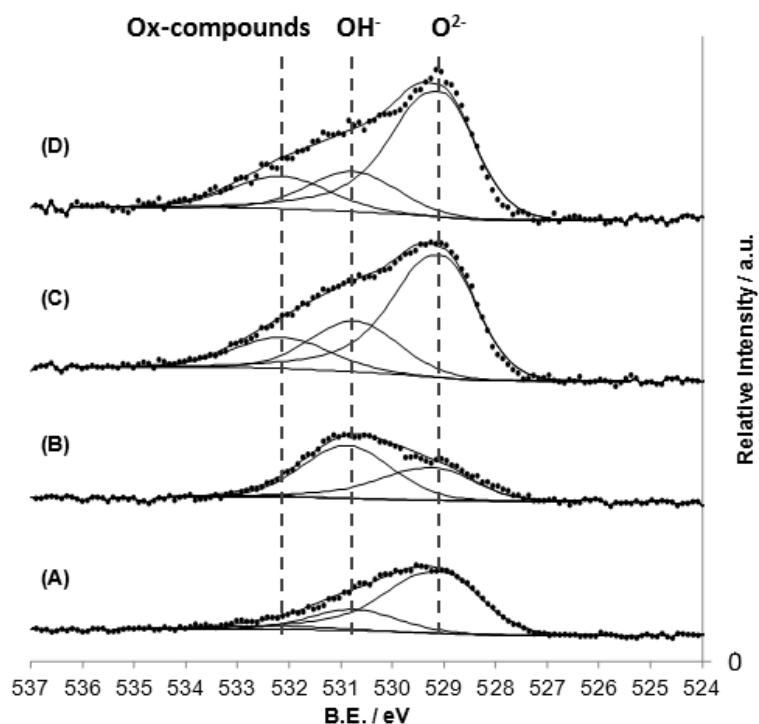


**Fig. 5.19** High resolution O 1s spectra recorded from  $\mu$ SOFC Ru anodes by XPS, (A) as prepared, (B) after operated with 3 % humidified hydrogen at 530 °C, (C) after operated with 3 % humidified methane at 530 °C, and (D) after operated with 3 % humidified natural gas at 530 °C. Increase of the O<sup>2-</sup> peak intensity at 529.1 eV and appearance of the third peak at 532.2 eV is observed with both methane and natural gas fuels, whereas increase in OH<sup>-</sup> peak at 530.8 eV was observed with humidified hydrogen.

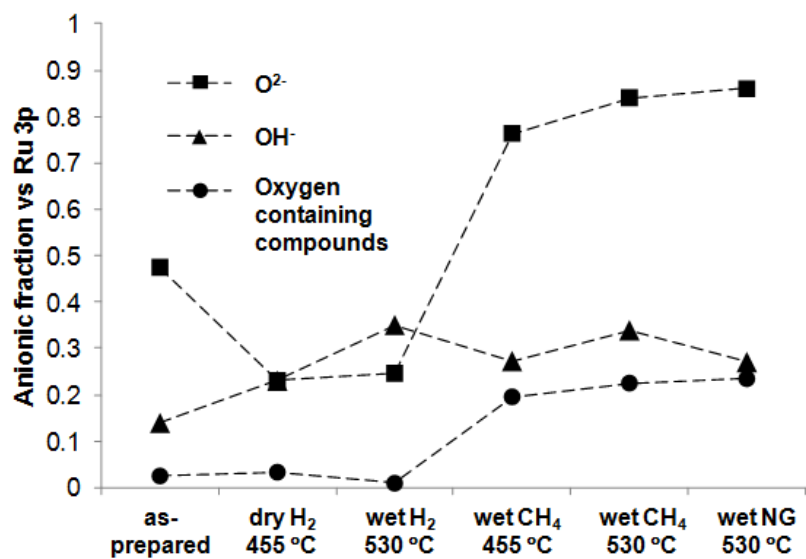
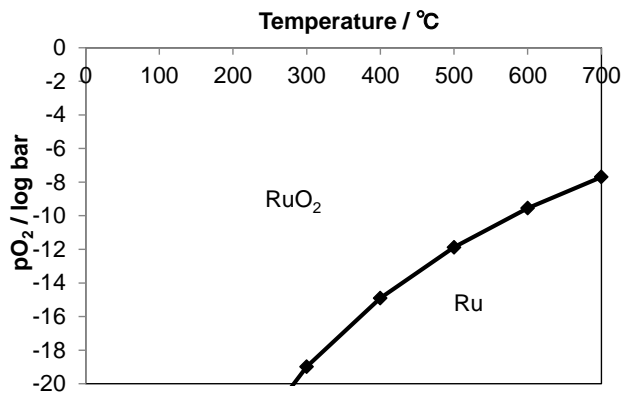
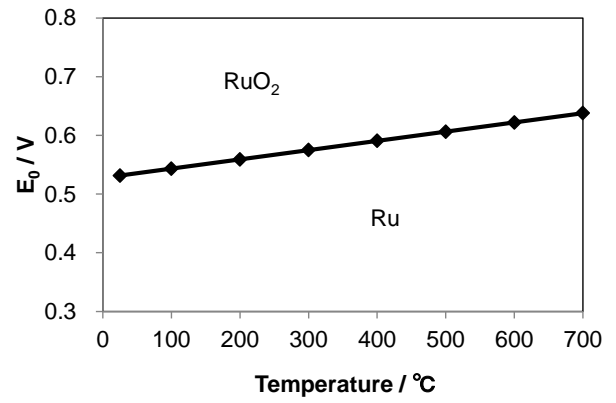


**Fig. 5.20** Relative intensity of oxidic species peaks on Ru anode relative to Ru 3p peak as a function of  $\mu$ SOFC operation condition. Peak intensities of  $O^{2-}$  and oxygen containing compounds show increase after methane and natural gas operation, while  $O^{2-}$  peak decreases after hydrogen operation.



(a)



(b)

**Fig. 5.21** (a) Partial pressure of oxygen, and (b) calculated anode potential, required for Ru oxidation under standard states.

### 5.3.4 Potential origin of the oscillatory behavior

Extensive oxygen coverage on the Ru anode surface and an appearance of the 3<sup>rd</sup> oxygen peak at higher B.E. after methane operation suggests that the oscillatory behaviors observed are due to the accumulation of an oxidized Ru layer and oxygen related intermediates. A current decay during an oscillation indicates a decrease in anode catalytic activities, and thus anode exchange current densities. In the following, only the effective exchange current density based on the geometric electrode area is discussed. In the Tafel region, the anode overvoltage and current density relationship for the reduced surface can be described as,

$$\eta_{an} = a_{Red} \ln \frac{j^{Red}}{j_{an0}^{Red}} \quad (5.7)$$

where  $\eta_{an}$  is the anode overvoltage,  $a_{Red}$  a constant,  $j_{an0}^{Red}$  the anode effective exchange current density and  $j^{Red}$  the fuel cell current density. For a surface covered with an oxidized layer or oxygen related intermediates, the relationship changes to the following:

$$\eta_{an} = a_{Ox} \ln \frac{j^{Ox}}{j_{an0}^{Ox}} \quad (5.8)$$

Here  $a_{Ox}$  is a constant,  $j_{an0}^{Ox}$  the anode effective exchange current density, and  $j^{Ox}$  the current density at the surface covered with oxidized layer or oxygen related intermediates. As the portion  $x$  ( $0 < x < 1$ ) of the Ru-YSZ interface becomes covered, the area averaged current density ( $j_{av}$ ) will change to,

$$j_{av} = (1 - x) j^{Red} + x j^{Ox} \quad (5.9)$$

$$j_{av} = (1 - x) \exp\left(\frac{\eta_{an}}{a_{Red}}\right) j_{an0}^{Red} + x \exp\left(\frac{\eta_{an}}{a_{Ox}}\right) j_{an0}^{Ox} \quad (5.10)$$

Since the catalytic performance of reduced metallic sites is significantly better than the oxygen covered sites [33, 34] we can expect  $j_{an0}^{Red} \gg j_{an0}^{Ox}$ . This indicates that increase in Ru surface oxygen coverage leads to approximately a linear reduction in average current density under fixed anode overvoltage. An area averaged exchange current density takes a value between  $j_{an0}^{Ox}$  and  $j_{an0}^{Red}$  depending on the surface coverage condition.

$$j_{ano}^{av} = (1 - x) j_{ano}^{Red} + x j_{ano}^{Ox} \quad (5.11)$$

In the Tafel region the fuel cell voltage  $E_{cell}$  at current  $j$  can be described as follows, where  $E_T^0$  is the theoretical OCV at temperature  $T$ ,  $\eta_{ca}$  the cathode overvoltage, and  $R_{ohm}$  the Ohmic resistance of the cell.

$$E_{cell}(j) = E_T^0 - \eta_{an}(j) - \eta_{ca}(j) - j R_{ohm} \quad (5.12)$$

The contribution from the ionic resistance of the YSZ electrolyte can be significantly high at this low operating temperature in conventional SOFCs. Representative ionic conductivity of YSZ electrolyte at 450 °C is  $\sim 0.0003 \text{ S cm}^{-1}$  [18, 112]. However, with a 110 nm electrolyte the contribution to the area specific resistance is minimum being  $\sim 0.04 \text{ } \Omega \text{ cm}^{-1}$ . Thus in case of  $\mu$ SOFCs with nano-meter scale electrolytes, the majority of losses comes from electrode polarizations. In the following, total overvoltages obtained at different anode oxygen coverage states are compared. A total overvoltage is described as,

$$\eta(j) = \eta_{an}(j) + \eta_{ca}(j) + j R_{ohm} \quad (5.13)$$

In the Tafel region, at certain anode oxygen coverage state total overvoltages at current density  $j$  can be describes as follows,

$$\eta^0(j) = a_{an} \ln \frac{j}{j_{ano}^0} + a_{ca} \ln \frac{j}{j_{cao}} + j R_{ohm} \quad (5.14)$$

$$\eta^1(j) = a_{an} \ln \frac{j}{j_{ano}^1} + a_{ca} \ln \frac{j}{j_{cao}} + j R_{ohm} \quad (5.15)$$

Superscripts 0 and 1 indicate different anode oxygen coverage states, and  $a_{an}$ ,  $a_{ca}$  are constants in Tafel equations. Here  $j_{cao}$  is the cathode exchange current density, and  $j_{ano}^x$  is the anode effective exchange current density at anode oxygen coverage state  $x$ . By comparing two I-V curves obtained at different anode oxygen coverage states 0 and 1 at a same fuel cell current  $j$ , equation (5.15) can be subtracted from equation (5.14). At the same fuel cell current point we can expect cathode overvoltage and Ohmic losses to be constant, between different anode oxidation states [113]. According to equation (5.12) this implies that  $\eta_{an}(j)$  must change

accordingly.

$$\eta_{an}^0(j) - \eta_{an}^1(j) = a_{an} \ln \frac{j}{j_{ano}^0} - a_{an} \ln \frac{j}{j_{ano}^1} \quad (5.16)$$

$$\eta_{an}^0(j) - \eta_{an}^1(j) = a_{an} \ln \frac{j_{ano}^1}{j_{ano}^0} \quad (5.17)$$

From definition of Tafel equation,  $a_{an}$  can be described as.

$$a_{an} = \frac{RT}{\alpha n F} \quad (5.18)$$

where R is the universal gas constant, T the cell temperature,  $\alpha$  the transfer coefficient, F the Faraday constant, and n the number of electrons transferred in each electrochemical event. Normalized area averaged exchange current densities can be obtained by the following relationship from equation (5.17).

$$\frac{j_{ano}^1}{j_{ano}^0} = \exp \frac{\eta_{an}^0(j) - \eta_{an}^1(j)}{a_{an}} \quad (5.19)$$

Current-voltage measurements obtained at different states during the fuel cell current oscillation are shown in **Fig. 5.22 (a)**. State 0 corresponds to the peak of the oscillation in **Fig. 5.23 (a)**, where other states are specified accordingly within the current decay. As the fuel cell current decays within the oscillation, the I-V curve shifts to the lower left direction indicating performance degradation. To obtain relative change in anode exchange current density from equation (5.19), a fuel cell current region corresponding to overvoltage of 100~300 mV was chosen assuming 1.05 V as the theoretical OCV [112]. **Figure 5.22 (b)** depicts difference of overvoltage between states within the current decay, plotted versus natural log of fuel cell current. As indicated in the figure, the flat portion to the left corresponds to the defined overvoltage regime and is used to calculate relative anode exchange current density with equation (5.19). Normalized exchange current densities derived from I-V measurements are shown with schematics of the Ru surface oxidation in **Fig. 5.23 (a)**, along with the fuel cell current oscillation. Indeed, the effective exchange current density decreases with the current decay, indicating a decrease in electrochemically active Ru-YSZ TPB interface. Note that the

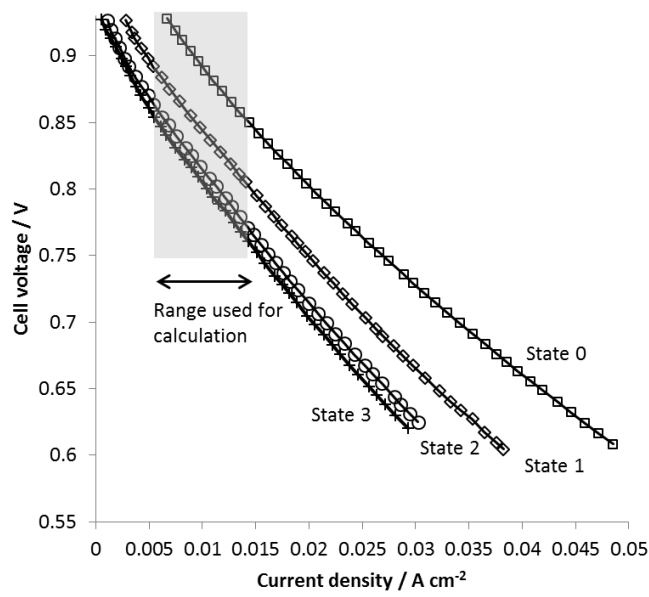
fuel cell current does not decay as much as the fraction of the anode exchange current density, due to the compensating increase in the anode overvoltage. This is due to a decrease in cathode overvoltage and Ohmic losses accompanied with the current decay as depicted in **Fig. 5.23 (b)**. The effective anode exchange current density drops for 98 % through the current decay, indicating nearly full coverage of the Ru active surface by oxygen and/or intermediates. **Figure 5.24** shows **(a)** I-V curves, **(b)** difference in overvoltages between the states, and **(c)** calculated effective anode exchange current densities during another current decay period observed in the oscillation. Similar to the previous analysis, extensive decay in effective anode exchange current density was observed.

As seen in **Fig. 5.17**, the fuel cell current shows a sudden recovery to its initial value after a gradual decay. This is possibly due to reduction of the Ru surface or removal of intermediates which restores its catalytic activity. The oscillatory behavior can therefore be attributed to a repeated transition between two surface states of Ru; namely metal exposed state with high catalytic activity and an oxidized or intermediates covered state with low catalytic activity. Very similar catalytic oscillation with a slow decay and a sudden recovery was observed in partial oxidation behavior of methane over Ru/Al<sub>2</sub>O<sub>3</sub> catalysts [114]. Along with the slow temperature drop in the catalyst bed, simultaneous decay of H<sub>2</sub> and CO concentration in the syngas was observed. The decay in partial oxidation catalytic activity and selectivity is reported to be due to gradual oxidation of the Ru surface. At the end of an oscillation cycle, the catalyst temperature recovers suddenly followed by increases in H<sub>2</sub> and CO concentrations. The rapid activity recovery was explained by an autonomous ignition of methane complete oxidation (or combustion) and consecutive Ru surface reduction induced by the temperature rise. Ru catalyst surface is more easily reduced at higher temperature [34]. As can be explained by the Ellingham diagram **Fig. 5.21 (a)**, at higher temperature Ru tends to be more in its metallic form under same oxygen partial pressure.

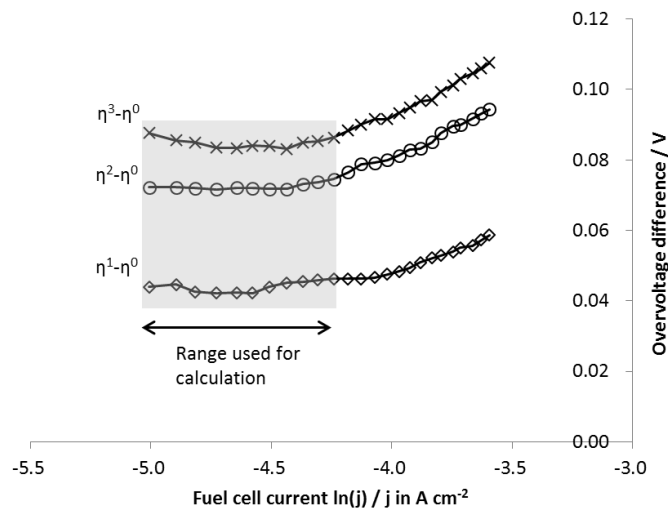
**Figure 5.25 (a)** shows high rate data acquisition results during the oscillation. Interestingly, the fuel cell current falls to 0 at the end of the current decay, indicating total activity loss of methane reforming and oxidation. However, the current recovers rapidly at the next moment and the whole cycle resumes again. A quantitative mechanism of the sudden recovery is not well understood, but it can be qualitatively explained from the viewpoint of the autonomous ignition observed in methane partial oxidation with Ru based catalysts [114], with an additional contribution from of a unique electrochemical mechanism in fuel cell anodes. **Fig. 5.25 (b)** schematically describes the transition of the anode surface states and resulting catalytic activities of reforming and partial oxidation against combustion. At point **a** in **Fig. 5.25 (a)** and **(b)**, methane reforming and partial oxidation dominantly takes place on the reduced Ru reaction sites. The Ru reaction sites are gradually oxidized at duration **b**, along with the decay in the reforming catalytic activity, hydrogen production and the fuel cell current. At point **c**, the reforming reaction and partial oxidation is quenched due to an extensive surface oxidation. It is interesting to note that in **Fig. 5.17 (a)** this quench occurred at approximately the same cell current point  $\sim 0.018 \text{ A cm}^{-2}$ , indicating that reforming is quenched at a certain anode overvoltage and thus a surface oxidation state. The fuel cell current falls to 0 at point **d** while cell voltage is maintained at 0.7 V, resulting in a steep increase in anode overvoltage. The overvoltage exceeds the oxidation limit in the Ellingham diagram **Fig.5.21 (b)**, leading to an accelerated electrochemical Ru surface oxidation, which in turn may ignite a complete methane oxidation reaction (or namely a combustion) at point **e**. The ignition results in an instantly high fuel cell current (point **f**) with a steep temperature rise. The temperature rise maybe enhanced due to limited thermal mass of a thin film  $\mu$ SOFC structure. The Ru surface is reduced to its metallic phase due to the temperature rise and decreased anode overvoltage, which activates the reforming and partial oxidation, and the overall cycle resumes. **Figure 5.26** schematically summarizes the proposed mechanism chain discussed above, focusing on reforming activity

affected by Ru surface oxidation, and ignition of complete oxidation that restores the activity.

Another possible mechanism of the oscillation is self-cleaning due to reaction between accumulated oxygen and methane reaction intermediates. Similar oscillation phenomenon was recently observed with Ni anodes with sulfur containing fuel under high fuel utilization condition [115]. The performance recovery in these oscillations was explained by the oxidation of adsorbed sulfur. Both Ru surface oxidation and adsorption of intermediates may lead to decrease in Ru catalytic activity. Analogous to the case of sulfur cleaning on Ni, performance recovery could be explained by Ru surface self-cleaning due to oxidation of adsorbed intermediate species. In order to further investigate and quantify the oscillation mechanism, in-operando studies such as utilizing synchrotron radiation X-ray absorption may be desirable.



(a)



(b)

**Fig. 5.22 (a)** Current-voltage measurements obtained at different states during the fuel cell current oscillation. The shaded region corresponds to overvoltage of 100~300 mV and is used for calculating relative change in anode exchange current density.

**(b)** Difference of overvoltage between states plotted versus natural log of fuel cell current.

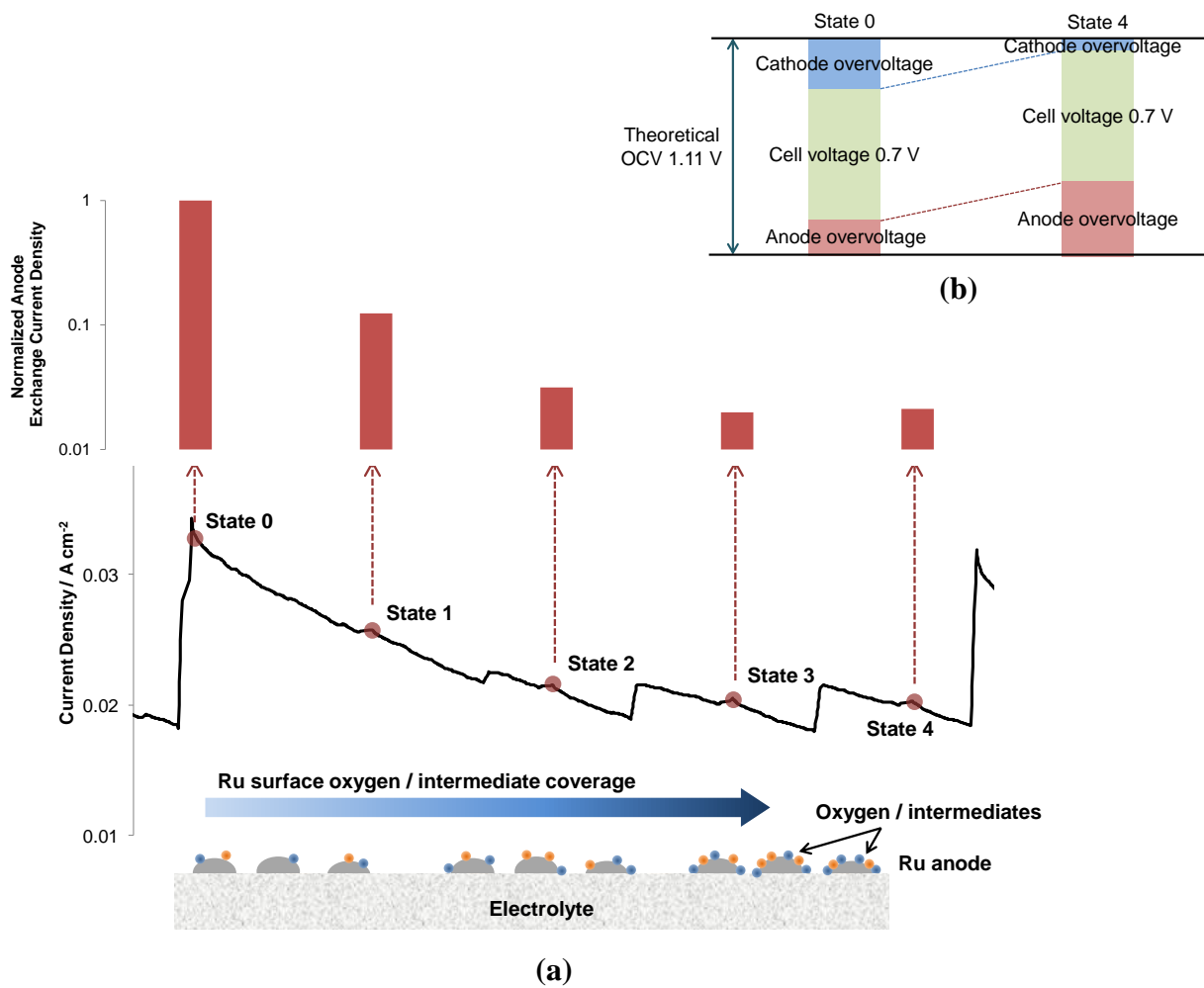


**Fig. 5.23 (a)** Fuel cell current history during test time of 70~120 min depicted in Fig. 5.7, with normalized effective anode exchange current density with respect to state 0 and a schematic of catalyst surface coverage states, and **(b)** a schematic of changes in anode and cathode overvoltage along the current decay.

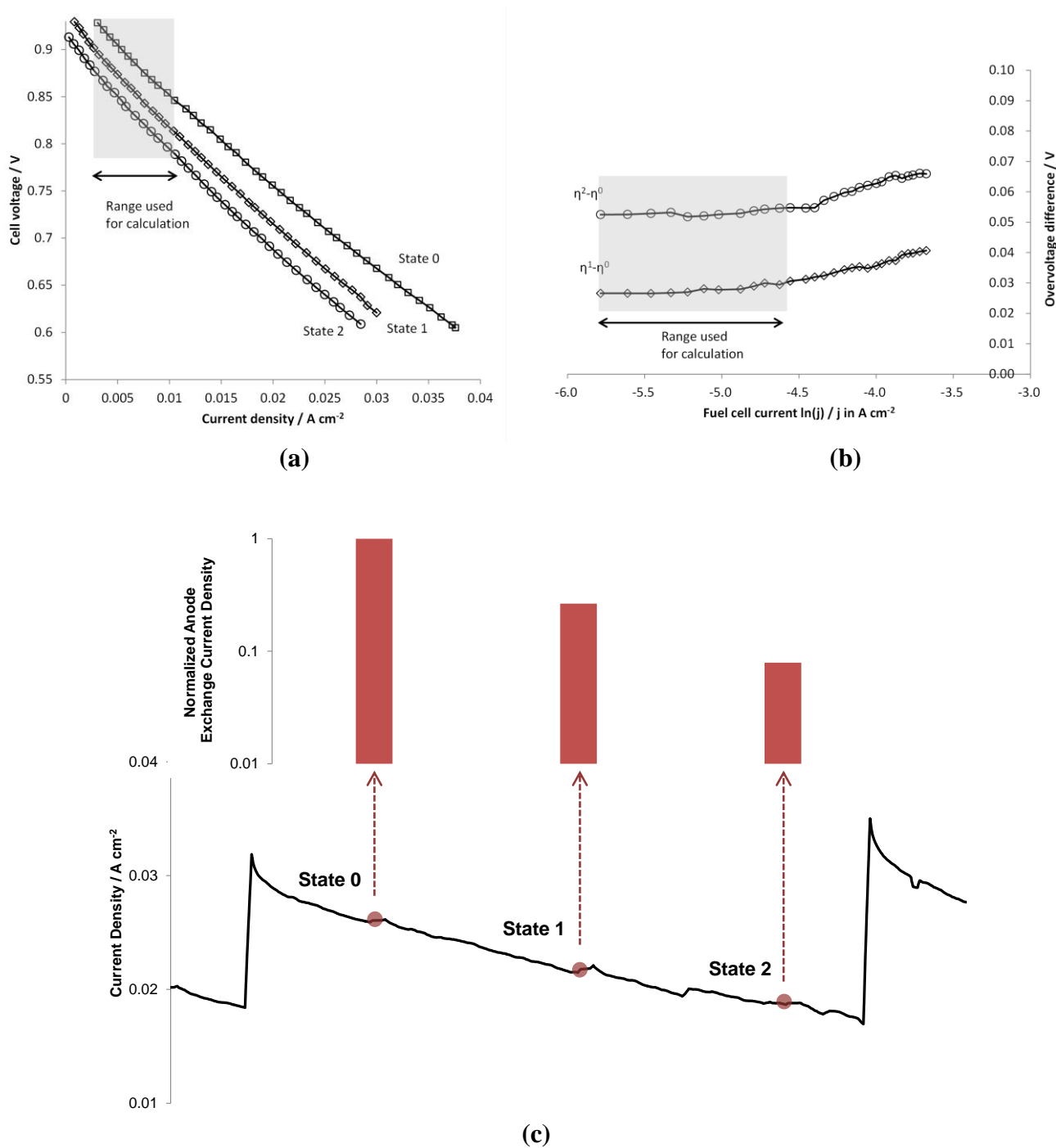
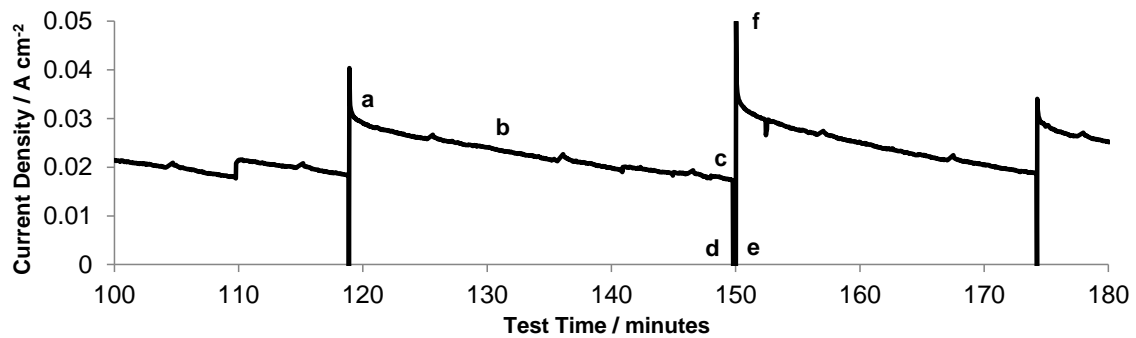
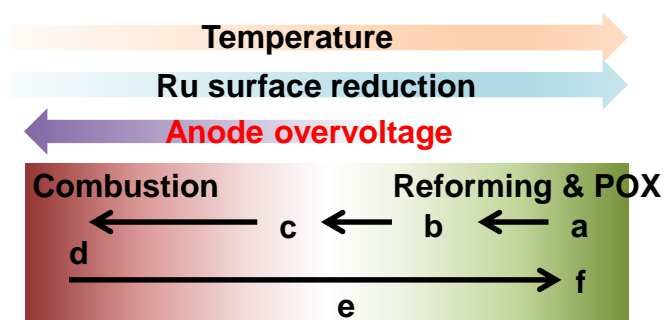


**Fig. 5.24** (a) Current-voltage measurements obtained during the fuel cell current oscillation, (b) difference of overvoltage between states plotted versus natural log of fuel cell current, (c) normalized effective anode exchange current density with respect to state 0 with fuel cell current history during test time of 115~155 min.



(a)



(b)

**Fig. 5.25 (a)** High rate acquisition of fuel cell current during the oscillation observed at 0.7 V constant voltage operation with methane fuel, cell temperature at 455 °C. **(b)** A schematic describing transition of temperature, oxidation states and catalytic activity at Ru anode surface. The alphabet symbols correspond to Ru anode surface states in **(a)**.

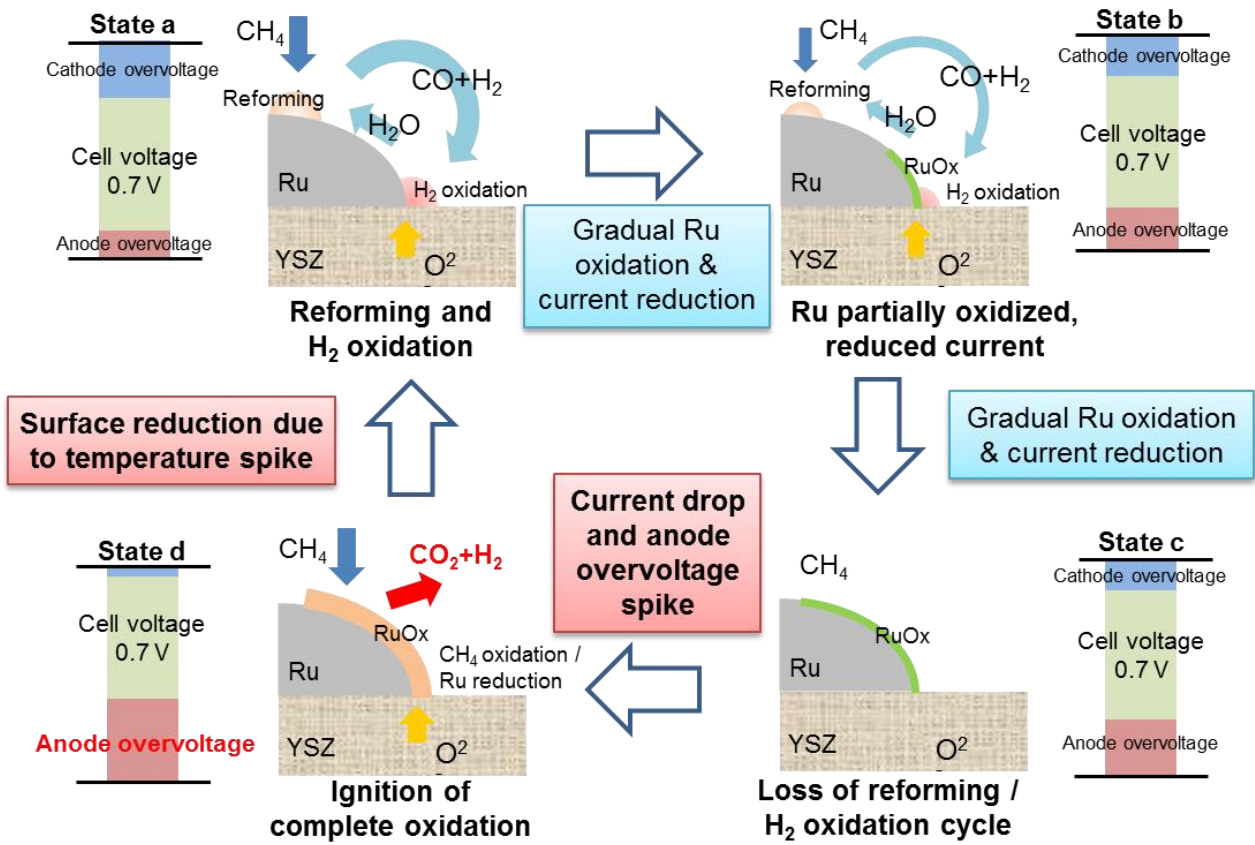


**Fig. 5.26** A schematic describing a proposed mechanism of current oscillations observed.

## 5.4 Conclusions

Thin film  $\mu$ SOFCs with nanoporous Ru anodes, YSZ electrolytes, and Pt cathodes have been fabricated and tested for direct methane utilization. The  $\mu$ SOFCs with Ru anodes showed a peak power density of  $450 \text{ mW cm}^{-2}$  and an OCV of  $0.71 \text{ V}$  at  $500 \text{ }^\circ\text{C}$  with methane and no apparent carbon deposition was observed after fuel cell tests. The morphology of Ru anodes after methane operation showed distinct difference from those of Pt electrode in hydrogen in the literature, exhibiting better structural stability leading to an excellent performance. It was also observed that the Ru anode morphology change was more suppressed under methane operation than under hydrogen operation.

With further optimization of the fabrication processes, the nano-porous Ru anode  $\mu$ SOFC exhibited peak power density of  $800 \text{ mW cm}^{-2}$  at  $530 \text{ }^\circ\text{C}$  with 3 % humidified natural gas as the fuel. The performance with dry methane and natural gas fuel was found to be comparable. Quasi-periodic oscillatory behavior of the cell current was observed when the  $\mu$ SOFC was continuously operated at constant voltage of  $0.7 \text{ V}$ . Through post-operation XPS analyses, it was found that oxidation states of Ru anode surfaces after operation significantly differ depending on the fuel. The oxygen peak was stronger with methane and natural gas fueled anodes compared to as-prepared and hydrogen fueled anodes. A third oxide species at  $532.2 \text{ eV}$  appears after operation with hydrocarbon fuels and was attributed to oxygen related intermediate products of the methane electrochemical reaction. Mechanisms leading to the oscillatory behavior are discussed based on Ru anode surface oxidation states, effective exchange current densities and transition of anode overvoltage. A gradual surface oxidation and decay in reforming reaction, coupled with a sudden activity restoration related to overvoltage-activated complete oxidation route is proposed as an origin of the oscillation, which is unique and only explainable by electrochemical / thermal interactions in  $\mu$ SOFCs.

## **Chapter 6: Characterization of Ruthenium – Gadolinia-Doped Ceria Nano-Composite Thin Films for Micro-Solid Oxide Fuel Cell Anodes**

### **6.1 Introduction**

In this chapter, Ru - gadolinia doped ceria (Ru-CGO) nano-composite thin films prepared by co-sputtering are investigated as anodes for  $\mu$ SOFCs. Following the results of chapter 5, Ru seems to be an excellent anode material for direct methane  $\mu$ SOFCs but its microstructural stability under operating condition remained as a concern. In attempt to stabilize Ru metal nano-structure in thin film electrodes, fabrication and characterization of Ru-CGO nano-composite thin films are investigated in this chapter. Detailed studies on electrical, crystal structural properties and microstructural stability of Ru-CGO thin films are discussed, prior to applying the thin film as  $\mu$ SOFC anodes.

### **6.2 Experimental Details**

#### **6.2.1 Growth and characterizations of pure gadolinia-doped-ceria thin films**

Before processing Ru-CGO composite films, properties of pure CGO thin films deposited on 0.5 mm thick single crystalline YSZ <100> (sc-YSZ) substrates (MTI Corp.) were investigated. CGO thin films were deposited by radio-frequency (RF) sputtering from a  $Gd_2O_3$  10 % :  $CeO_2$  90 % target (purity 99.99%, from Plasmaterials, Inc.) in an Ar environment without substrate heating. Morphology and film deposition rates were investigated by varying deposition pressures between 5 and 40 mTorr while target powers were varied between 100~150 W. Film thicknesses of CGO resulted in 25~80 nm range. Film deposition rates of Ru thin films were investigated to have them compared with those of CGO, varying deposition pressures between 10~75 mTorr while target powers were varied between 50~200 W. Ru film thicknesses resulted in 15~85 nm range. Film deposition rates were calculated from film thicknesses and duration

of depositions, where film thicknesses were estimated by XRR. Crystallinity of the films was investigated by X-ray diffraction (XRD). XRR and XRD measurements on thin film samples were carried out with a Bruker D8 X-ray Diffractometer using Cu K $\alpha$  radiation. Nano-scale morphology of the thin films were investigated using a Carl Zeiss Ultraplus Field Emission SEM.

### **6.2.2 Growth and characterizations of ruthenium - gadolinia-doped-ceria composite thin films**

Composite thin films of Ru and CGO were fabricated by co-deposition of DC-sputtering from metal Ru target and RF-sputtering from ceramic CGO target, as schematically shown in **Fig. 6.1**. Single crystal sapphire <0001>, single crystal YSZ (sc-YSZ), Si<sub>3</sub>N<sub>4</sub> coated Si (Si<sub>3</sub>N<sub>4</sub>/Si), and YSZ coated Si<sub>3</sub>N<sub>4</sub>/Si (YSZ/Si<sub>3</sub>N<sub>4</sub>/Si) were used as substrates. Films on sapphire substrates were used for electrical characterization and thickness calibration of the composite films, while those on YSZ/Si<sub>3</sub>N<sub>4</sub>/Si substrates were used for XRD studies to investigate film crystalline structure. For the YSZ/Si<sub>3</sub>N<sub>4</sub>/Si substrates, ~100 nm thick polycrystalline YSZ thin films were deposited on Si<sub>3</sub>N<sub>4</sub>/Si substrates to simulate the  $\mu$ SOFC electrolyte surface. Films on sc-YSZ and Si<sub>3</sub>N<sub>4</sub>/Si were used to compare substrate effects on the film morphology.

Different fractions of Ru in composite films were obtained by varying the DC power of Ru target, while RF power of CGO target was fixed at 100 or 150 W. Based on the deposition rates determined from individual Ru and CGO depositions, nominal volumetric Ru/CGO ratios were designed in the range of Ru/CGO = 2/3 to 3/1.

XRD, XRR, microstructure and room temperature in-plane electrical conductivity of as-deposited Ru-CGO films were characterized accordingly with the same methods for pure Ru and CGO films. Crystalline structure evolution of composite thin films on YSZ/Si<sub>3</sub>N<sub>4</sub>/Si substrates under annealing at 500 °C for 1 h in 5 % H<sub>2</sub>/Ar environment was investigated by

XRD. Deposition rates of the composite films were calculated based on film thicknesses obtained by XRR and deposition time. Chemical composition of the as-deposited samples were evaluated by analyzing X-ray Photoelectron Spectrometer (XPS) spectra acquired in a Surface Science SSX-100, after sputtering the samples for 20 min with Ar to remove surface contaminants. Surface morphology and roughness of composite films were measured by SEM and an Asylum Research MFP-3D Atomic Force Microscope (AFM) system.

In-plane conductivities of thin films deposited on sapphire substrates with 200 nm thick dense gold contacts was measured in an environmental chamber while heating the substrate. A representative view of a sample used for in-plane conductivity measurements with gold contact pads is shown in **Fig. 6.2**. Direct current conductivity measurements were performed between room temperature and 500 °C flowing 5 % H<sub>2</sub>-Ar gas through the chamber, while the sample temperature was ramped up at the rate of 10 °C min<sup>-1</sup>. Evolution of thin film morphology was studied with SEM before and after the test.

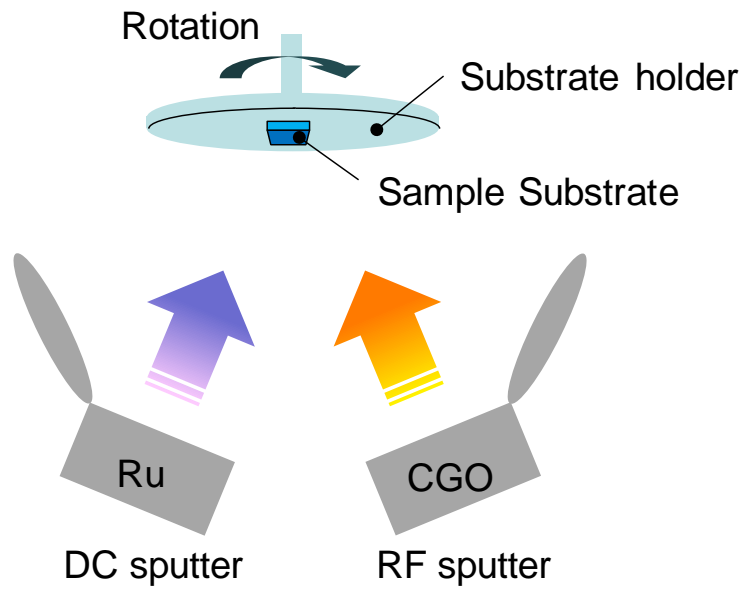


**Fig. 6.1** Schematic of co-sputtering from Ru metal target (DC sputter) and from CGO ceramic target (RF sputter).

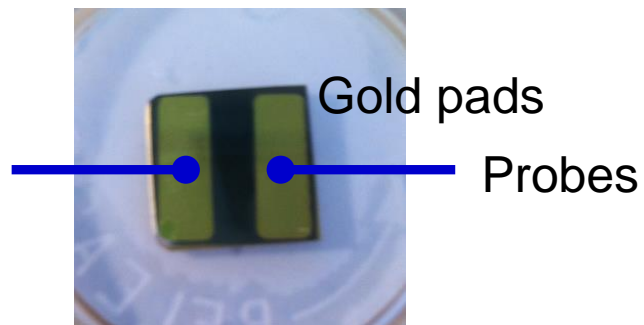


**Fig. 6.2** A representative view of a Ru-CGO composite film deposited sample used for in-plane conductivity measurements with gold contact pads.

## 6.3 Results and Discussion

### 6.3.1 Characterizations of gadolinia-doped-ceria thin films

**Figure 6.3** presents SEM images of as-deposited CGO thin films grown at different deposition pressures and powers. Smoother morphology was observed with CGO films compared to Ru films. The films were rougher when deposition pressure was 10~20 mTorr, but became featureless at 40 mTorr with no grain boundaries distinguishable. Typical grain sizes observed at deposition pressure of 10~20 mTorr were 10~20 nm. Growth rates of Ru and CGO films under various pressures and powers are summarized in **Fig. 6.4**. Since the deposition rate of CGO became extremely low at 75 mTorr, the maximum co-deposition pressure was limited to 40 mTorr. At 40 mTorr, the CGO target power was fixed to 150 W and Ru target power was adjusted to control the film composition. At 10 mTorr, the CGO target power was fixed to 100 W. The colored area (10~40 mTorr,  $\sim 4\text{nm min}^{-1}$ ) shows an operation window where deposition rates of Ru and CGO are in an equivalent range, giving controllability to tune the film composition to the desired ratio.

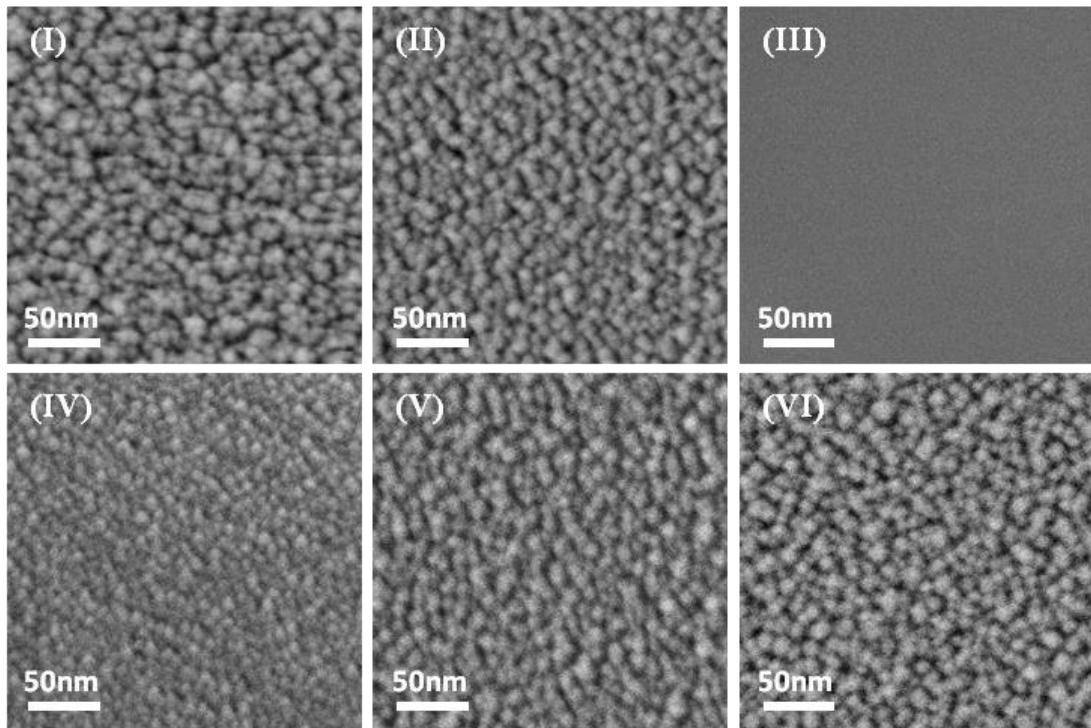


**Fig. 6.3** Surface morphology (SEM) of as-deposited CGO films on single crystal YSZ

substrates, at deposition pressures and powers of;

**(I)** 10 mTorr, 100 W, **(II)** 20 mTorr, 100 W, **(III)** 40 mTorr, 100 W,

**(IV)** 5 mTorr, 150 W, **(V)** 10 mTorr, 150 W, and **(VI)** 20 mTorr, 150 W.

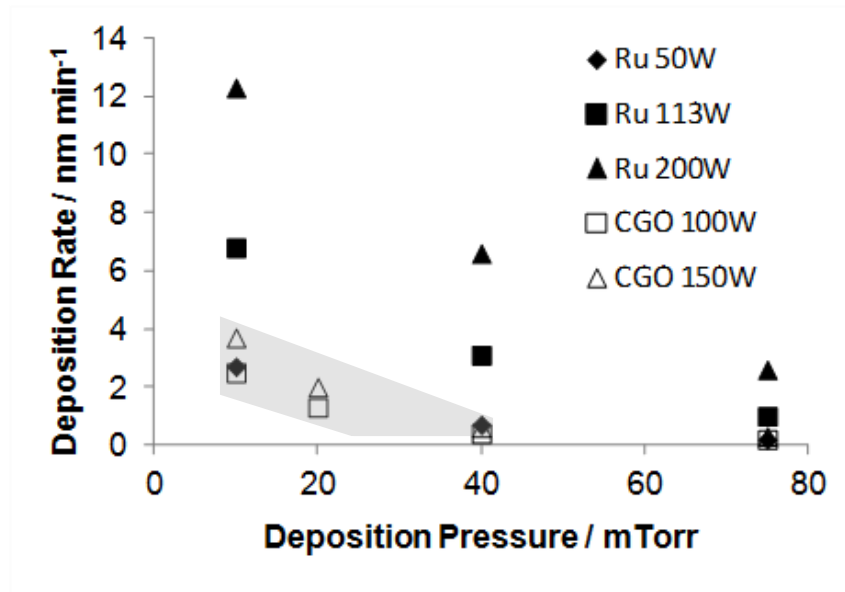


**Fig. 6.4** Dependence of Ru and CGO film deposition rates on deposition pressure and power.

### 6.3.2 Characterizations of ruthenium - gadolinia-doped-ceria composite thin films

#### Morphology, crystal structure and chemical compositions

Ruthenium - CGO composite films with nominal volumetric Ru/CGO ratio of 2/3, 1/1, 3/2 and 7/3 (namely, R2C3, R1C1, R3C2 and R7C3, respectively) were prepared with deposition parameters shown in **Table 6.1**. R3C2 composite films on single crystal sapphire, sc-YSZ and Si<sub>3</sub>N<sub>4</sub>/Si substrates showed smooth nano-crystalline morphology with grain sizes of ~10 nm as can be seen in **Fig. 6.5 (a)-(c)**. In contrast, the films on YSZ/Si<sub>3</sub>N<sub>4</sub>/Si substrate showed highly granular morphology with primary grain sizes of ~10 nm and secondary grains or pillars as large as 70~100 nm as shown in **Fig. 6.5 (d)**. This morphology may be due to the different surface textures of polycrystalline YSZ thin film from single crystal or amorphous substrates. Cross-sectional view of R1C1 film on YSZ/Si<sub>3</sub>N<sub>4</sub>/Si substrate is shown in **Fig. 6.6**. Pillar-like granular morphology can be observed, indicating that composite film growths are being strongly affected by the under-layer texture. Similar pillar-like morphology of secondary grains has been observed in Ni-YSZ co-sputtered films in the past study [63]. Morphology and surface

roughness measurements results of R7C3 composite films deposited on sc-YSZ and YSZ/Si<sub>3</sub>N<sub>4</sub>/Si substrates, by AFM, are shown in **Fig. 6.7 (a)** and **(b)**. As is consistent with the SEM results presented in **Fig. 6.5**, composite films on polycrystalline YSZ thin film showed an enhanced surface roughness. The root mean squared roughness of the films were 1.3 nm and 3.6 nm on sc-YSZ and YSZ/Si<sub>3</sub>N<sub>4</sub>/Si substrates, respectively. **Figure 6.8 (a)** shows XRD patterns of room temperature deposited composite films on YSZ/Si<sub>3</sub>N<sub>4</sub>/Si substrates with various Ru fractions. For pure CGO film, peaks from both CGO film and YSZ underlayer were observed and the peak positions were consistent with those of cubic fluorite lattice parameters of CGO and YSZ, respectively. Pure Ru film exhibited XRD pattern of hexagonal structure with a relatively weak <002> peak. Only YSZ related peaks were identified with R2C3 and R1C1 films indicating poor crystallization of Ru and CGO, possibly due to formation of amorphous phases or very-fine-grained polycrystalline structures [116]. With an increase of Ru content in the films, Ru related peaks appeared as presented in cases of R3C2 and R7C3 films. Within the range of the Ru/CGO ratio in this study, CGO related peaks were not apparent in as-deposited films. Co-deposition of Ru with CGO seems to hinder formation of Ru and CGO crystallites. Past studies on metal-ceramic co-deposited films also indicated similar effects [71, 73]. In order to investigate crystalline structure evolution in the composite electrode under fuel cell operating condition, R1C1, R3C2 and R7C3 thin films on YSZ/Si<sub>3</sub>N<sub>4</sub>/Si substrates were annealed at 500 °C in 5 % H<sub>2</sub>/Ar environment for 1 h. As shown in **Fig. 6.8 (b)**, annealed Ru-CGO composite thin films revealed fluorite CGO related peaks along with enhanced Ru peaks, indicating ionic transport capability of CGO in the composite anode under the fuel cell operating condition. As expected, CGO peaks grew stronger as CGO/Ru ratio was increased. It is interesting to note that CGO <200> peak were suppressed compared to <111> and <220> peaks, indicating preferential growth of CGO under metal-oxide co-deposition which was not observed in pure CGO growth as shown in **Fig. 6.8 (a)**. No secondary or

unidentified peak was observed.

In order to quantify atomic compositions of CGO and Ru in the composite films, XPS measurements were performed. Relative atomic molar ratio of Ru to (Ce + Gd) derived from XPS measurements and calculated volumetric ratio of Ru to CGO in R1C1, R3C2 and R7C3 samples are shown in **Table 6.1**, respectively. Clear dependency of Ru increase and (Ce + Gd) decrease in film compositions are observed by increasing Ru/CGO nominal deposition ratio from 1/1 to 7/3. The calculated volumetric ratio of Ru to CGO was in fair agreement with those designed from calibrated deposition rates.

**Table 6.1** Nominal compositions, deposition conditions, atomic ratios of Ru/(Ce + Gd), and corresponding volumetric ratios of Ru/CGO in composite thin films.

Sample ID	Nominal Ru/CGO Ratio by Deposition Rates	Ru Target DC Power [W] / CGO Target RF Power [W]	Deposition Pressure [mTorr]	Atomic Ratio of Ru/(Ce+Gd) Measured by XPS	Volumetric Ratio of Ru/CGO <sup>(a)</sup>
R2C3	2 / 3	31 / 100	10	N/A	N/A
R1C1	1 / 1	46 / 100	10	79 / 21	55 / 45
R3C2	3 / 2	69 / 100	10	84 / 16	65 / 35
R7C3	7 / 3	108 / 100	10	89 / 11	74 / 26

<sup>(a)</sup> Volumetric ratio is estimated under the assumption that CGO is in cubic fluorite phase

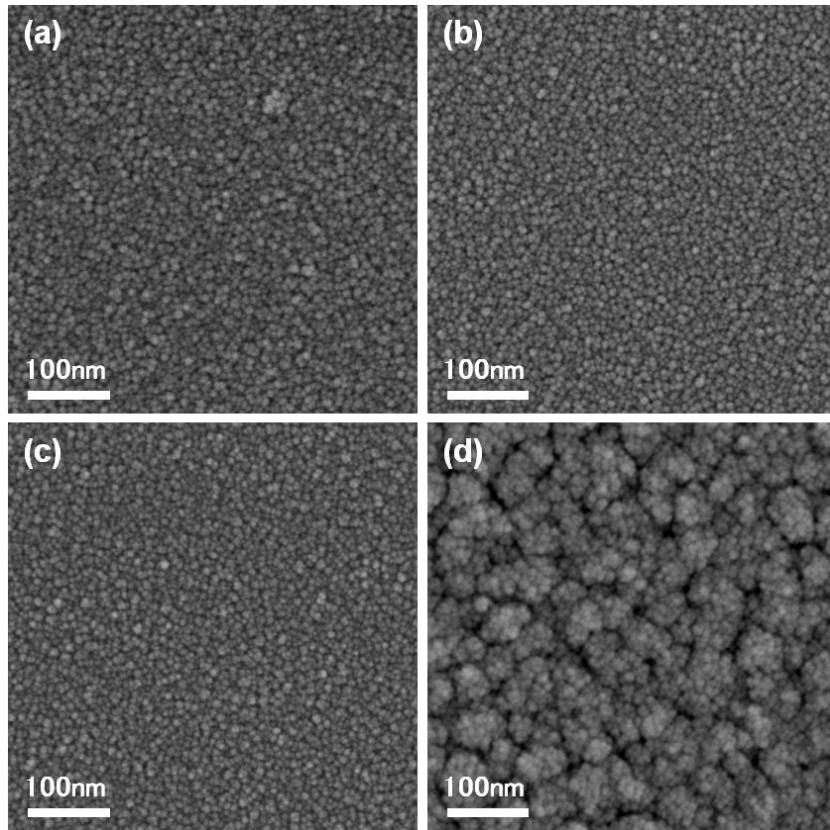


**Fig. 6.5** SEM micrographs of R3C2 composite films on (a)  $\text{Si}_3\text{N}_4/\text{Si}$ , (b) single crystal YSZ, (c) single crystal sapphire, and (d) YSZ/ $\text{Si}_3\text{N}_4/\text{Si}$  substrates. (R3C2 represents nominal volumetric ratio of Ru/CGO = 3/2)

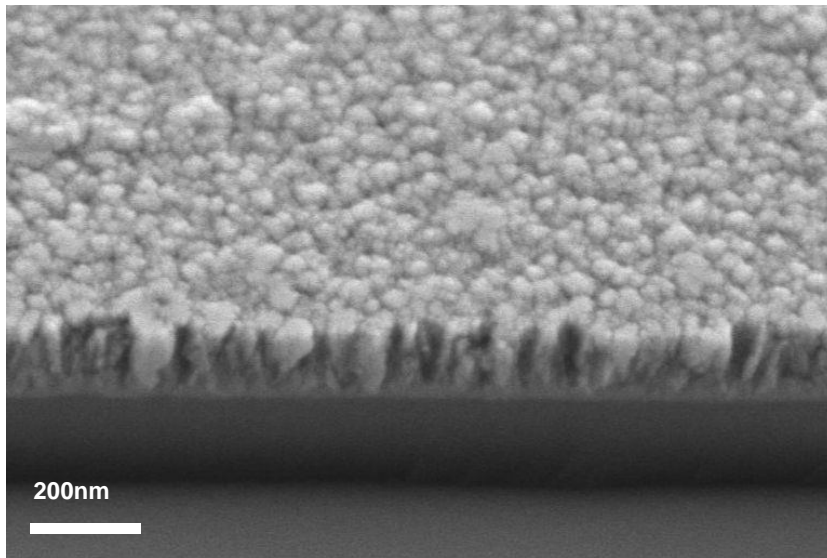


**Fig. 6.6** Cross-sectional SEM micrographs of a R1C1 composite film on YSZ/Si<sub>3</sub>N<sub>4</sub>/Si substrate. (R1C1 represents nominal volumetric ratio of Ru/CGO = 1/1)

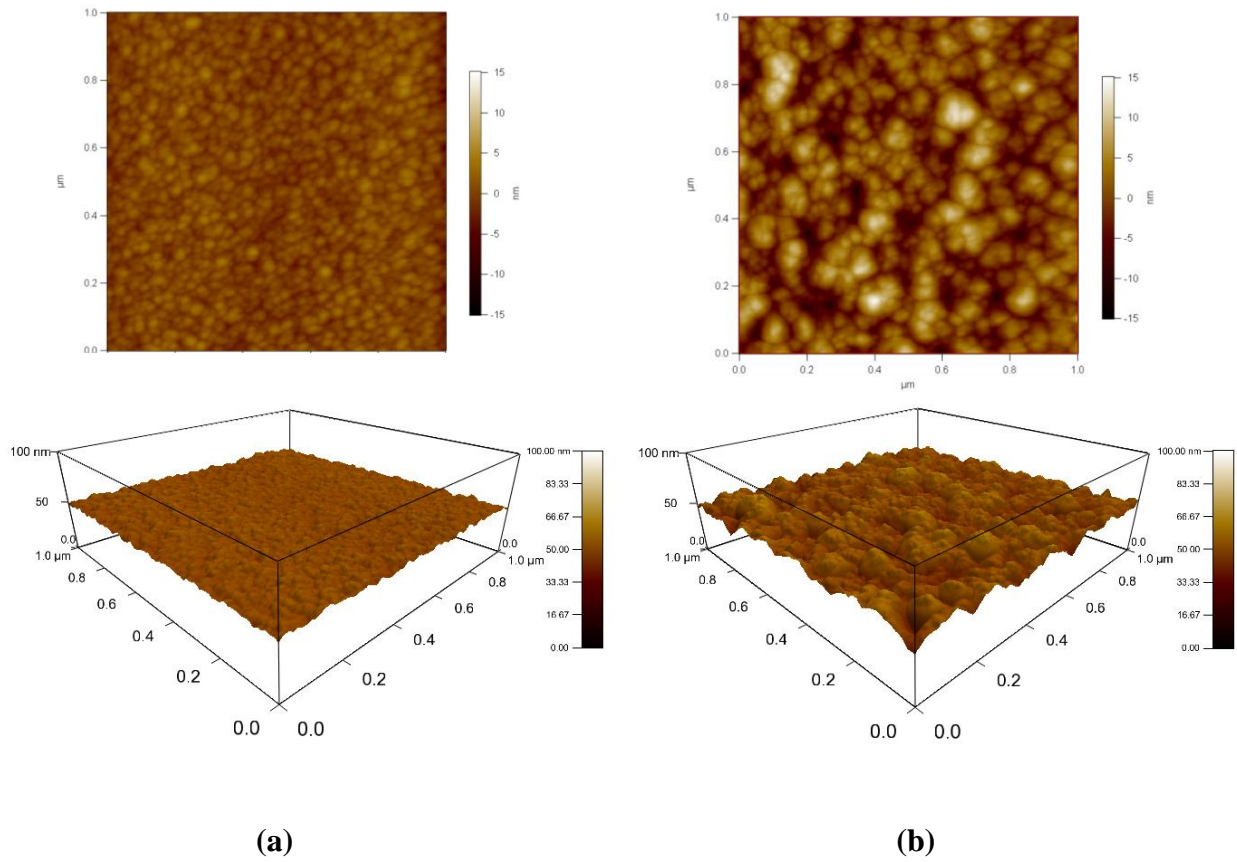
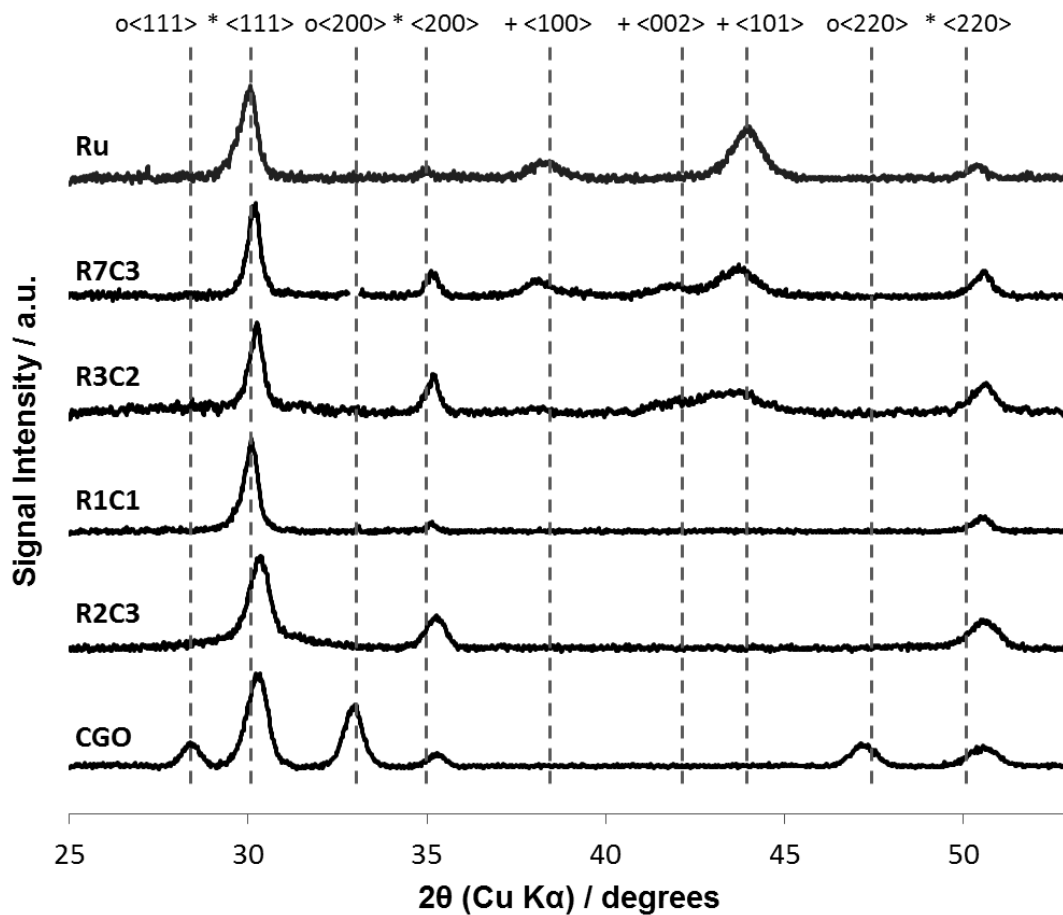


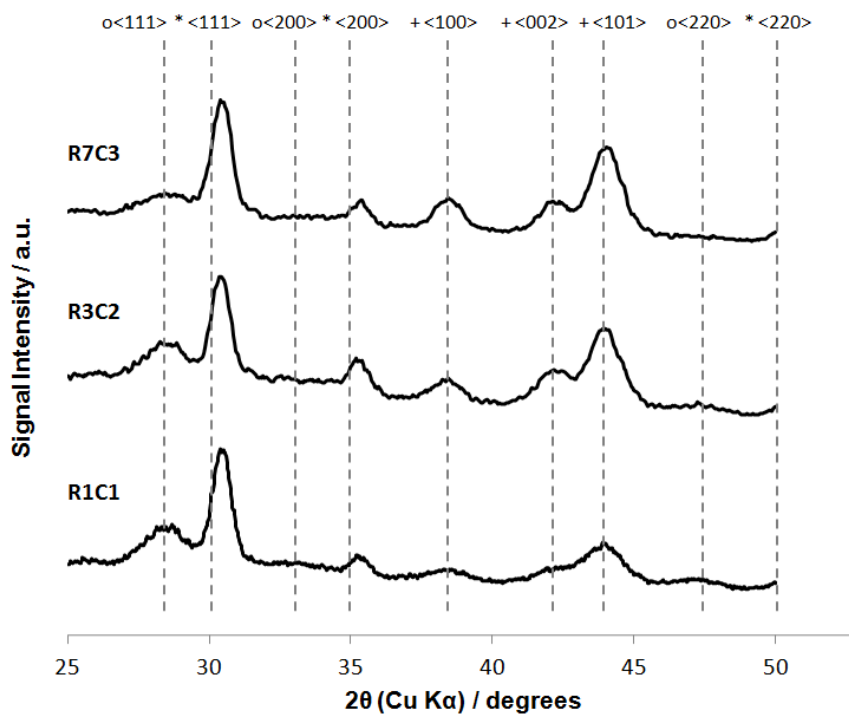
**Fig. 6.7** Atomic force microscope measurement results of R7C3 composite films deposited on (a) sc-YSZ substrate, and (b) YSZ/Si<sub>3</sub>N<sub>4</sub>/Si substrate. The root mean squared roughness of the films were 1.3 nm and 3.6 nm on sc-YSZ and YSZ/Si<sub>3</sub>N<sub>4</sub>/Si substrates, respectively.

(R7C3 represents nominal volumetric ratio of Ru/CGO = 7/3)



(a)

**Fig. 6.8 (a)** X-ray diffraction patterns of as-deposited pure Ru, R7C3, R3C2, R1C1, R2C3, and pure CGO films on YSZ/Si<sub>3</sub>N<sub>4</sub>/Si substrate. Peak positions of (\*) cubic YSZ indexed in JCPDS 00-030-1468, (+) hexagonal Ru indexed in JCPDS 01-073-7011, and (o) cubic CGO indexed in JCPDS 00-050-0201 are presented in the figures.



(b)

**Fig. 6.8 (b)** X-ray diffraction patterns of R7C3, R3C2, and R1C1 films on YSZ/Si<sub>3</sub>N<sub>4</sub>/Si substrates annealed at 500 °C in 5 % H<sub>2</sub>/Ar environment for 1 h. Peak positions of (\*) cubic YSZ indexed in JCPDS 00-030-1468, (+) hexagonal Ru indexed in JCPDS 01-073-7011, and (o) cubic CGO indexed in JCPDS 00-050-0201 are presented in the figures.

### Electrical conductivity and microstructural stability at elevated temperatures

In-plane electrical conductivities of Ru-CGO composite films on single crystal sapphire substrates with different Ru/CGO ratios are shown in **Fig. 6.9 (a)**. Deposition pressures were 10 mTorr for all samples, and conductivities were measured at room temperature. Strong dependence of conductivity on Ru fraction can be observed, as in-plane percolating conduction paths are being developed as Ru content is increased. The high volumetric Ru content of more than 50 % required for percolation indicates two-dimensional formation of conduction pathways [117]. Increasing deposition pressure of R7C3 films resulted in lower conductivity as depicted in **Fig. 6.9 (b)** indicating an increase in film porosity. Increase in deposition pressure is known to decrease the density of the film, due to decrease in kinetic energy of sputtered particles reaching the substrate after more frequent collisions with Ar molecules in the chamber environment. Conductivities of the composite films are more than two orders of magnitude lower than that of Ru bulk ( $1.3 \times 10^5 \text{ S cm}^{-1}$ ). This indicates that Ru grains are effectively separated by CGO grains, or that Ru grains are loosely bounded to each other with nano-pores.

In order to further investigate the effect of deposition pressure on film porosity, electron densities were evaluated by XRR analyses on R7C3 thin films with different deposition pressures. Electron density and thickness of a thin layer along the direction normal to the specimen surface can be determined by analyzing the XRR pattern, and a film porosity can be estimated. The XRR profiles taken from R7C3 thin films are shown in **Fig. 6.10**, where deposition pressures were **(a)** 10 mTorr, **(b)** 40 mTorr, and **(c)** 75 mTorr. The calculated film thicknesses were 63 nm, 59 nm, and 69 nm for films **(a)**, **(b)**, and **(c)**, respectively. Profiles contain a critical angle of incidence  $\alpha_C$  where its position gives the average electron density, and interference fringes where their periods give the film thickness. From the critical angle  $\alpha_C$ , the film porosity can be derived by comparing the value to the critical angle  $\alpha_{C0}$  for an ideally

dense substance. Here  $\rho_{e0}$  is the electron density of an ideally dense substance,  $\rho_e$  the electron density of a condensed matter, and  $\phi$  the film porosity calculated from the ideal and measured film electron densities.

$$\frac{\alpha_C}{\alpha_{C0}} = \sqrt{\frac{\rho_e}{\rho_{e0}}} \quad (6.1)$$

$$\phi = 1 - \frac{\rho_e}{\rho_{e0}} \quad (6.2)$$

Details of the above formula derivations are described in section 4.3. Electron density in Ru phase was calculated based on a hexagonal close-packed structure with lattice parameters listed on **Table 4.2**. Electron density in CGO phase was calculated assuming CeO<sub>2</sub> fluorite cubic structure with lattice parameters listed on **Table 6.2**. The critical angle  $\alpha_{C0}$  for an ideally dense composite film was derived based on nominal volumetric fractions of Ru and CGO. For R7C3 composite film,  $\alpha_{C0}$  is 0.454 deg. The measured critical angle  $2\alpha_C$  of 10 mTorr deposited film was 0.77 deg where that of 40 mTorr deposited film was 0.70 deg, and that of 75 mTorr deposited film was 0.63 deg. Calculated film porosities of R7C3 films from XRR measurements using equations (6.1) and (6.2) are plotted in **Fig. 6.11** with different deposition pressures, along with calculated film porosities of porous Ru films from section 4.3. The film porosity ranged from 27 % to 53 %, showing approximately linear dependence on the deposition pressure. Film porosities of composite thin films appeared to be lower compared to those of pure Ru films deposited at same pressure. The XRR measurements and analyses on critical angle of incidence revealed film porosities of composite films to be largely dependent on deposition pressure.

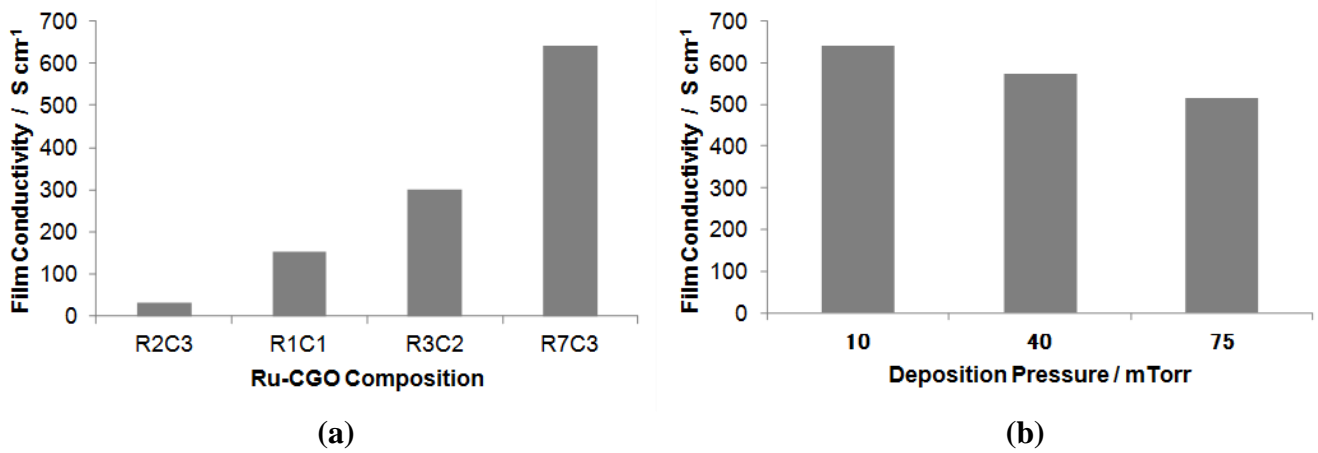
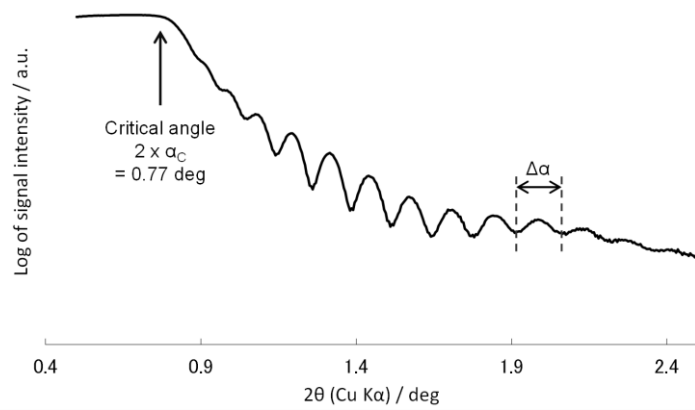


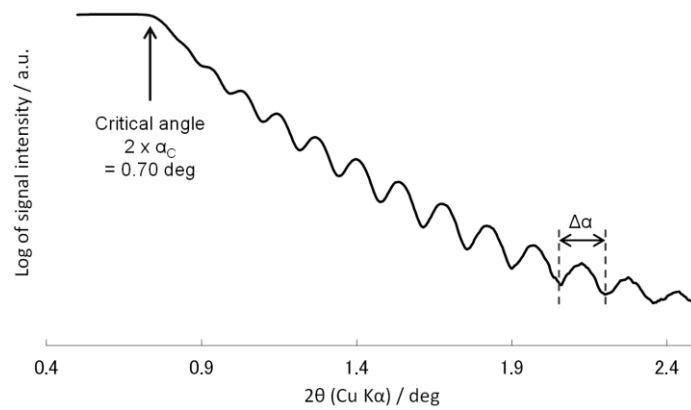
**Fig. 6.9 (a)** DC conductivity of 10 mTorr deposited films with different Ru/CGO ratios on single crystal sapphire substrates measured at room temperature. **(b)** DC conductivity of as-deposited R7C3 films with different deposition pressures, measured at room temperature.

**Table 6.2** Lattice parameter and electron densities of CeO<sub>2</sub> cubic fluorite crystalline structure.

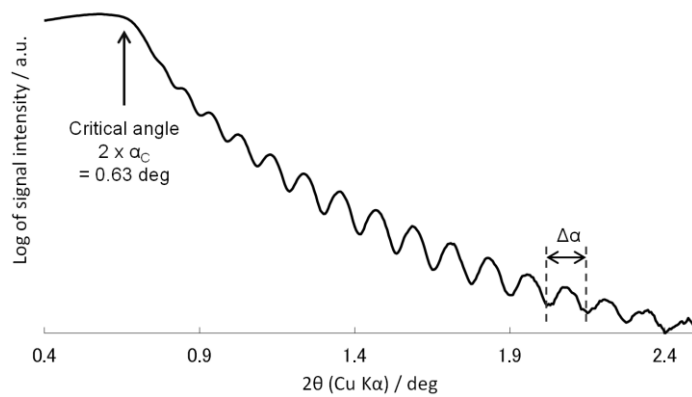
Cell parameter	
a	5.4112 Å
Cell volume	158.45 Å <sup>3</sup>
Number of atoms in one cell	4
Electron density $\rho_{e0}$	$2.27 \times 10^{30} \text{ m}^{-3}$
Critical Angle $\alpha_{C0}$	0.398 deg



(a)



(b)



(c)

**Fig. 6.10** XRR profiles measured from Ru-CGO composite thin films on single crystal sapphire substrates deposited at (a) 10 mTorr, (b) 40 mTorr, and (c) 75 mTorr.

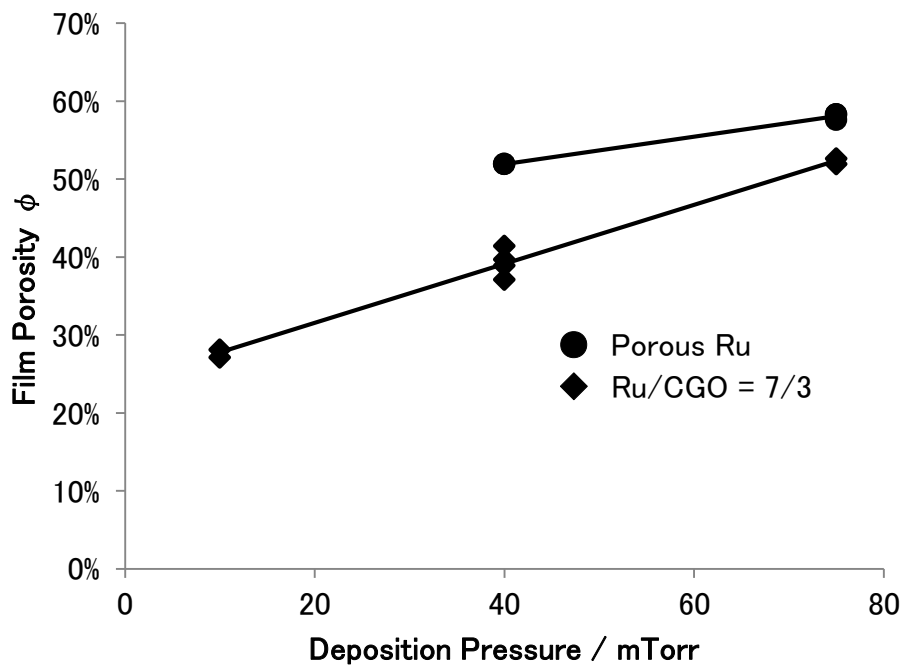
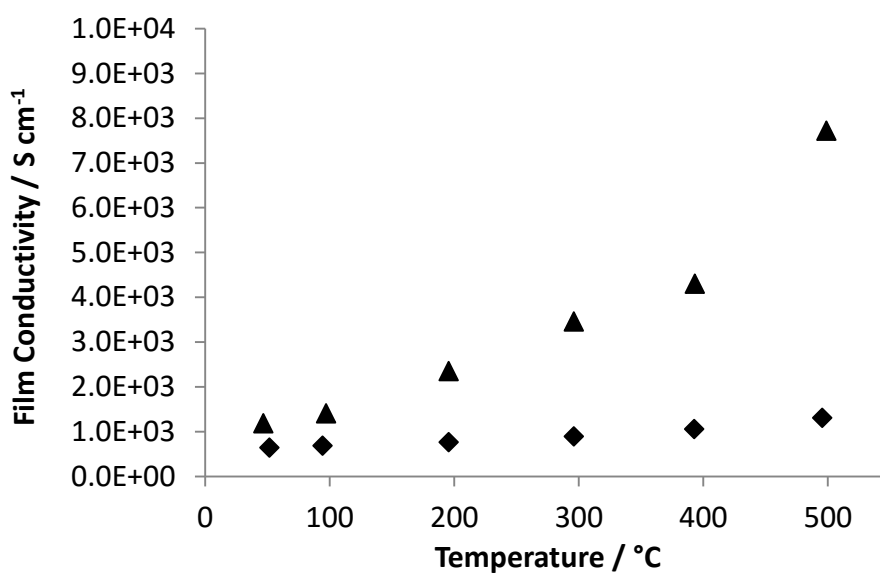
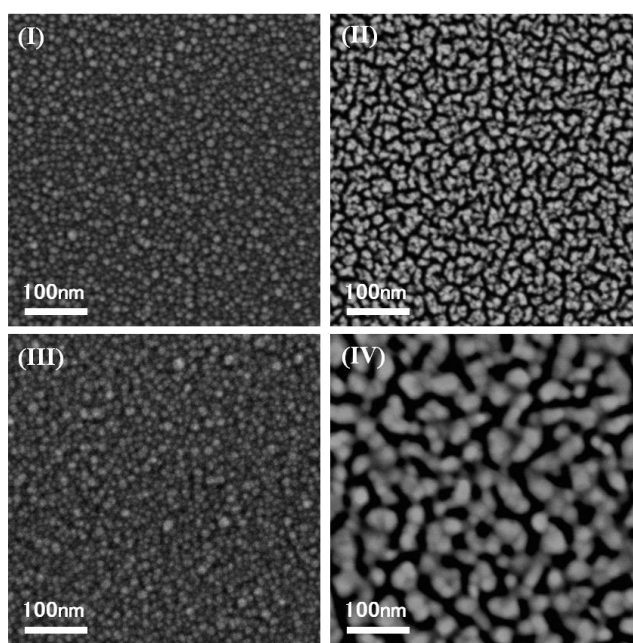


**Fig. 6.11** Calculated film porosities of R7C3 composite films deposited under different pressures, derived from XRR profiles. Calculated film porosities of pure porous Ru films with different deposition pressures are plotted in the figure as references.

Temperature dependent in-plane conductivities of a R7C3 film and a pure Ru film deposited on single crystal sapphire substrates were measured in an environmental chamber, flowing 5 % H<sub>2</sub>/Ar gas constantly to create a reducing environment. As shown in **Fig. 6.12 (a)**, the film conductivity increased from  $6.4 \times 10^2$  to  $1.3 \times 10^3$  S cm<sup>-1</sup> for the R7C3 film, and  $1.2 \times 10^3$  to  $7.7 \times 10^4$  S cm<sup>-1</sup> for the pure Ru film as temperature was increased from room temperature to 500 °C. The conductivity of the pure Ru film increased for 6.5 times from the initial state indicating enhanced interconnectivity in the metal film due to the morphology evolution. On the contrary, the increase in conductivity of the composite film was less than 1/10 compared to the pure metal film, suggesting that the metal-ceramic composite structure effectively restrained Ru coarsening driven by thermal annealing. In **Fig. 6.12 (b)**, SEM images before and after the in-situ heating tests are compared. As seen in images **(II)** and **(IV)**, coarsening and growth of Ru grains from <10 nm to 30~40 nm was observed for the pure metal film. The composite film showed no distinguishable change in the morphology as can be seen in images **(I)** and **(III)**. Grain growth was minor, if any, resulting in ~10 nm grain sizes. In-plane electrical conductivity changes and morphology evolutions of Ru and Ru-CGO films at elevated temperature suggest that co-sputtered Ru-CGO composite structure effectively stabilizes electrode microstructures.



(a)



(b)

**Fig. 6.12** (a) In-plane conductivity of the R7C3 and Ru metal films deposited on sapphire substrates, measured in-situ under heating from room temperature to 500 °C in 5 % H<sub>2</sub>/Ar condition. (b) Surface morphology of films before (I, II), and after (III, IV) the heating test; (I, III) R7C3, and (II, IV) Ru metal film.

## 6.4 Conclusions

Ru-CGO nano-composite thin films were fabricated and characterized targeting  $\mu$ SOFC anodes for direct methane utilization. Control window of Ru-CGO co-deposition was defined to be in the range of  $\text{Ru/CGO} = 2/3 \sim 3/1$ , where the deposition pressure was 10~40 mTorr. The composite film showed smooth nano-crystalline morphology with grain sizes of ~10 nm on single crystal sapphire, sc-YSZ and  $\text{Si}_3\text{N}_4/\text{Si}$  substrates, where the morphology was highly granular on polycrystalline YSZ thin films. Direct current in-plane conductivity and crystalline structure of the composite films were investigated for various relative fractions of the metal and the oxide. The CGO phase in the nano-composite film was crystalline after the annealing, indicating ionic transport capability in the electrode. It was found that the film porosity can be controlled by co-deposition pressure, where higher pressure leads to more porous (less dense) film. The Ru-CGO nano-composite thin film showed significantly improved microstructural stability compared to the nano-porous Ru thin film, where its in-plane electrical conductivity change during heating to 500 °C in  $\text{H}_2/\text{Ar}$  was 1/10 of that of nano-porous Ru film with no apparent morphological change observed in SEM.



## **Chapter 7: Micro-Solid Oxide Fuel Cells with Ruthenium – Gadolinia-Doped Ceria Nano-Composite Anodes**

### **7.1 Introduction**

In this chapter, Ru - gadolinia doped ceria (Ru-CGO) composite thin films prepared by co-sputtering are applied as anodes for  $\mu$ SOFCs and the fuel cell performance is investigated with methane as the fuel. Macroscopic structural integrity of Ru-CGO anode  $\mu$ SOFCs were achieved by developing stress-relaxed composite thin film anodes, and performance of the  $\mu$ SOFCs were optimized by varying Ru/CGO composition. To the best of our knowledge, this was the first attempt to explore metal-ceramic composite anodes for self-supported thin film SOFCs. Open circuit voltage of 0.97 V and peak power densities of 275 mW cm<sup>-2</sup> were achieved at 485 °C with 3 % humidified methane as the fuel. Morphological stability of nano-composite anodes are investigated through microstructural analysis following an extended operation of  $\mu$ SOFCs.

### **7.2 Experimental Details**

#### **7.2.1 Fabrication of thin film micro-solid oxide fuel cells with ruthenium - gadolinia-doped ceria composite anodes**

Thin film  $\mu$ SOFC platforms with YSZ electrolyte and Pt cathodes were fabricated following the processes described in chapter 2. Thin film Ru-CGO composite anodes were deposited on self-supported YSZ/Pt  $\mu$ SOFC structure by co-deposition of DC-sputtering from metal Ru target and RF-sputtering from ceramic CGO target in Ar without substrate heating. Several deposition conditions varying chamber pressure and Ru / CGO target power were investigated.

## 7.2.2 Performance measurement of thin film micro-solid oxide fuel cells with ruthenium - gadolinia-doped ceria composite anodes

Electrochemical performance tests on  $\mu$ SOFCs were performed following the procedure specified in section 2.4. Room temperature humidified 5 %  $H_2/Ar$  gas was supplied to the anodes of  $\mu$ SOFCs at a flow rate of  $50 \text{ ml min}^{-1}$  during temperature ramp from 250 to 400 °C. At 400 °C the  $H_2/Ar$  gas was turned off and room temperature humidified pure methane gas was fed at a flow rate of  $50 \text{ ml min}^{-1}$ . The cathodes were exposed to laboratory air. Electrical current collection was done through deposited electrodes without extra current collectors. Programmed current-voltage (I-V) measurements were carried out periodically during the temperature ramp to obtain fuel cell performance. Morphology of Ru-CGO composite anodes were investigated with SEM before and after the fuel cell measurements.

## 7.3 Results and Discussion

### 7.3.1 Fabrication and performance evaluation of ruthenium - gadolinia-doped ceria composite anode micro-solid oxide fuel cells

Ruthenium-CGO composite thin films were deposited on  $\mu$ SOFC platforms as anodes with various relative fractions. A typical optical micrograph of a Ru-CGO anode  $\mu$ SOFC is show in **Fig. 7.1**. A typical size of the self-supported  $\mu$ SOFC membranes were 200  $\mu\text{m}$  square. Characteristic buckling of  $\mu$ SOFC membranes were observed as a result of compressive film stresses in deposited dense YSZ film, which is typically seen. **Figure 7.2 (a)** and **(b)** shows SEM micrographs of R7C3 and Ru/CGO = 3/1 (namely, R3C1) anodes on  $\mu$ SOFC thin film electrolytes before fuel cell measurements. Ru-CGO anode films deposited on self-supported electrolytes exhibited a smooth feature, similar to films deposited on single crystal substrates.

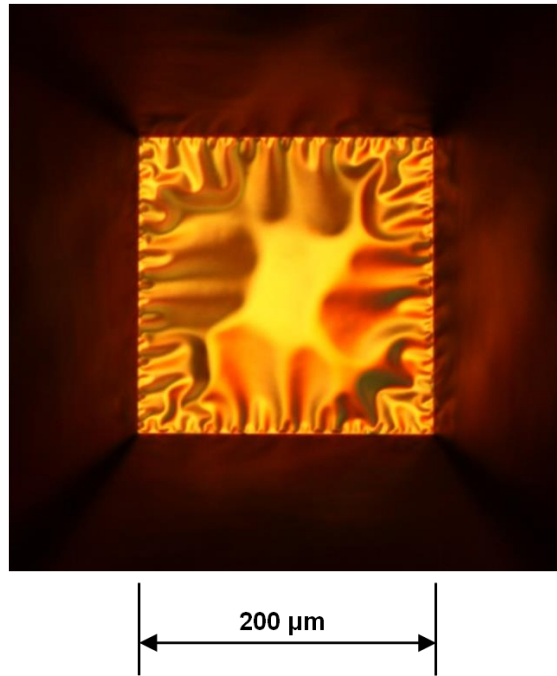


**Fig. 7.1** Optical micrograph of self-supported  $\mu$ SOFC with Ru-CGO composite anode, taken from the anode side. Buckling is due to the compressive stress typical in such membranes.

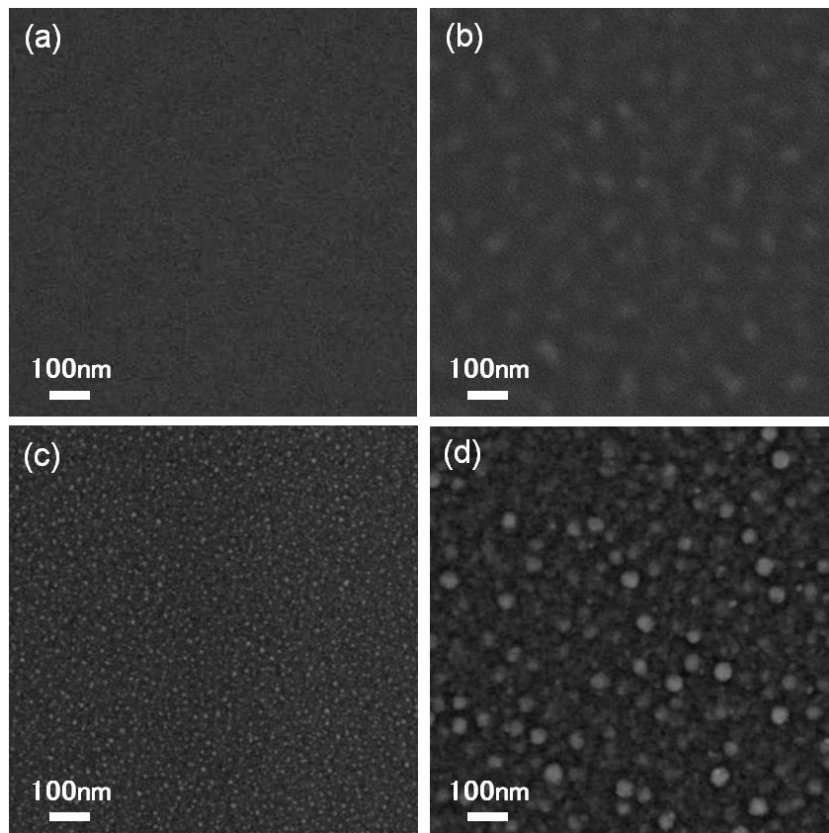


**Fig. 7.2** SEM micrographs of Ru-CGO composite anodes on  $\mu$ SOFCs, as-deposited (**a, b**), and after fuel cell operations (**c, d**); (**a, c**) FC4 with R7C3 anodes, and (**b, d**) FC5 with R3C1 anodes.

**Table 7.1** Anode compositions, deposition pressures and fuel cell test results of  $\mu$ SOFCs with Ru-CGO composite anodes.

Fuel Cell ID	Anode Composition *	Deposition Pressure [mTorr]	OCV with H <sub>2</sub> fuel [V]	OCV with CH <sub>4</sub> fuel [V]	Maximum Power with CH <sub>4</sub> fuel [mW cm <sup>-2</sup> ]
FC1	R1C1	10	0.14	Not Measurable	Not Measurable
FC2	R3C2	10	0.88	Not Measurable	Not Measurable
FC3	R7C3	10	0.98	Not Measurable	Not Measurable
FC4	R7C3	40	1.0	0.96	31
FC5	R3C1	40	0.93	0.99	275

\* R1C1 represents Ru:CGO = 1:1 in volumetric ratio.

**Table 7.1** summarizes deposition parameters and performance test results of fabricated Ru-CGO anode  $\mu$ SOFCs. Increasing Ru/CGO ratio from 1/1 to 7/3 lead to improvement of OCV under hydrogen fuel, as seen in the test results of FC1, FC2 and FC3. However when cell temperatures were ramped up to ~400 °C and fuel gas was switched to methane, fuel cells with anodes deposited at 10 mTorr mechanically failed by membrane fractures. A SEM image of a broken fuel cell (FC3) is shown in **Fig. 7.3 (a)** exhibiting fractures through the entire membrane. Ceria based electrolytes are known to have mechanical instabilities due to the lattice expansion arising from the transition of Ce<sup>4+</sup> to Ce<sup>3+</sup> under reducing conditions [18, 75, 76, 83]. The failures of thin films we have observed may be attributed to this expansion in the anode electrodes. Another possible source of membrane failures can be volume expansion of the anode electrode caused by oxidation of ruthenium. **Table 7.2** shows lattice parameters and unit volume of RuO<sub>2</sub> rutile crystalline structure [118]. Comparing the unit volume per single Ru atom in rutile RuO<sub>2</sub> structure (31.34 Å<sup>3</sup>) to that of hexagonal Ru structure (13.57 Å<sup>3</sup>) as listed in **Table 4.2**, there is a ~130 % increase. In case of conventional fuel cell electrodes, it is likely

that only atoms those are close to the electrode surfaces are oxidized and the resulting total volume expansion can be negligible from mechanical integrity point of view. However in case of nano-crystalline thin film electrodes, surface area compared to particle volume is relatively large and volume expansion related to surface oxidation may induce a significant internal stress. In order to investigate the effect of fuel cell operation with methane on the surface oxidation states of R7C3 anodes, XPS measurements were carried out on the anodes before and after the operation. R7C3 anodes were deposited at 40 mTorr. **Figure 7.4** shows oxygen peaks from XPS measurements on **(a)** as-deposited R7C3 anode, and **(b)** R7C3 anode after fuel cell operation with 3 % humidified methane at 450 °C. Oxygen peaks were deconvoluted into three oxygen species,  $O^{2-}$ ,  $OH^-$ , and oxygen related compounds. Details of the deconvolution process are discussed in chapter 5. The peak areas were normalized against Ru 3d 5/2 peak intensity, in order to compare the amount of oxygen on the surface relative to Ru. **Figure 7.4 (b)** shows clear growths in peaks associated to  $O^{2-}$  and oxygen related compounds after methane operation. **Figure 7.4 (c)** depicts the total oxygen fraction on Ru surface of R7C3 anode measured by XPS, after fuel cell operation with methane relative to the as-deposited anode. A clear increase in total oxygen species of ~150 % was observed. Oxidation mechanism of Ru during methane operation is investigated in chapter 5 in more detail. Addition to the possible volume change of ceria due to its transition of the valence state, Ru oxidation and related volume expansion is likely to be playing a role in the macroscopic mechanical integrity of Ru-CGO anode  $\mu$ SOFCs.

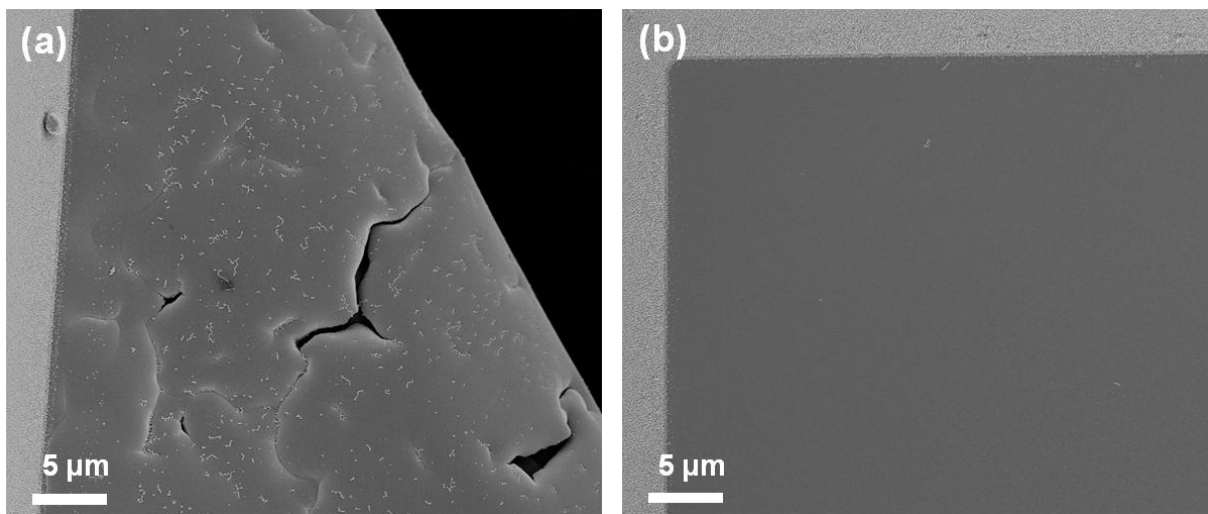


**Fig. 7.3** SEM micrographs of  $\mu$ SOFCs after operation, (a) FC3; anode deposited at 10 mTorr, and (b) FC4; anode deposited at 40 mTorr.

**Table 7.2** Lattice parameters and unit volume of  $\text{RuO}_2$  rutile crystalline structure.

Cell parameters		
	a	4.4919 Å
	b	3.1066 Å
Cell volume		62.68 Å <sup>3</sup>
Number of Ru atoms in one cell		2
Volume per single Ru atom		31.34 Å <sup>3</sup> / atom

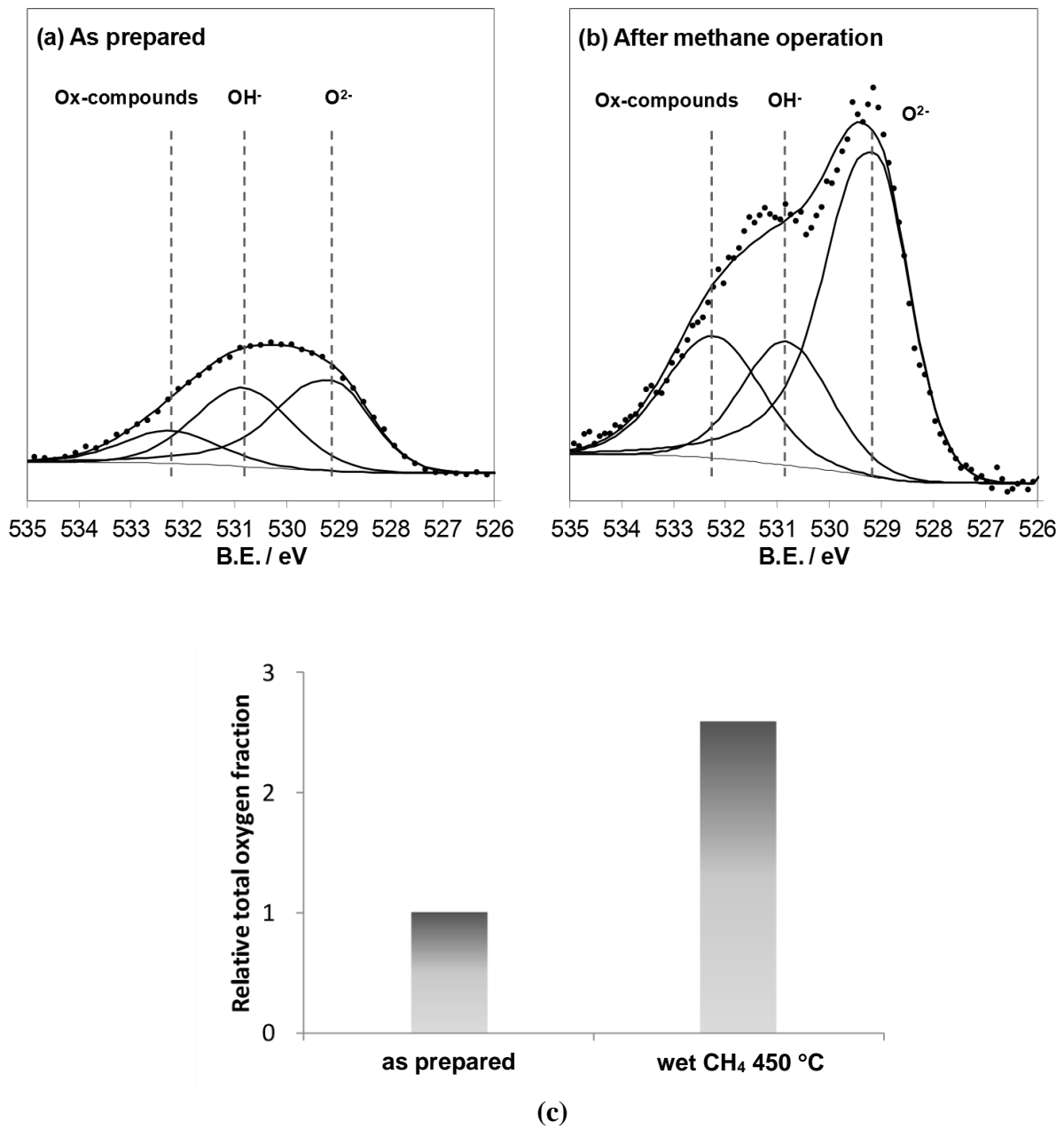
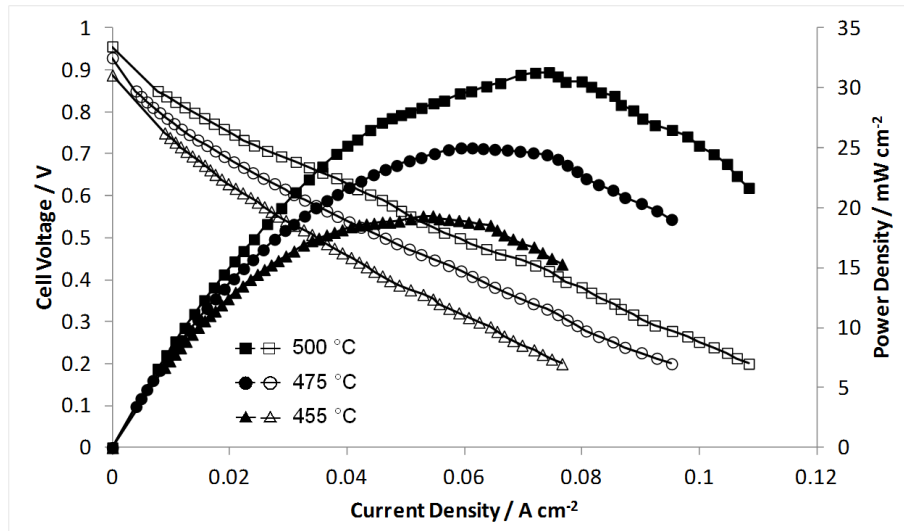


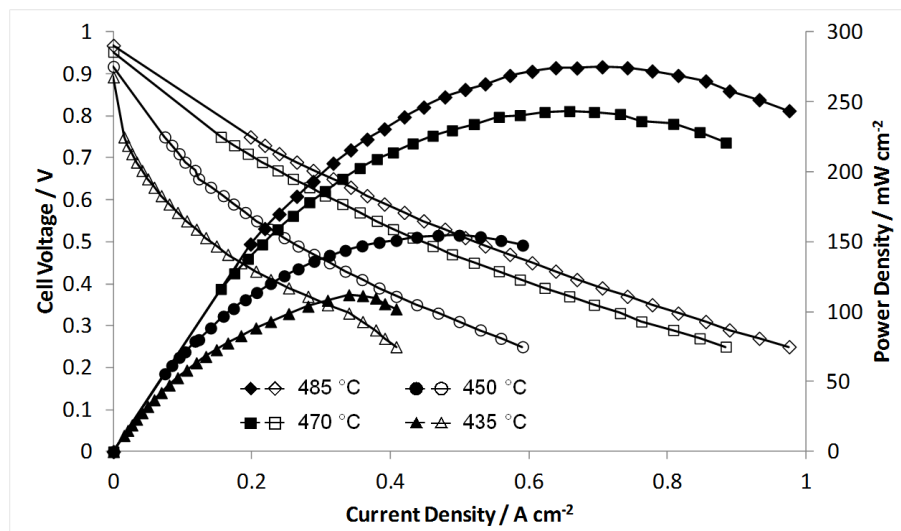
**Fig. 7.4** Oxygen peaks from XPS measurement results of (a) as-deposited R7C3 anode, and (b) R7C3 anode after fuel cell operation with 3 % humidified methane at 450 °C. (c) Relative intensity of total oxide peak area on R7C3 anode after fuel cell operation with methane fuel, with relative to the as-deposited R7C3 anode.

Changing the deposition pressure from 10 mTorr to 40 mTorr improved the thermal-mechanical stability of  $\mu$ SOFCs. As previously discussed in section 6.3, increased deposition pressure is expected to decrease the density of the film, which can in turn relax compressive stresses induced during temperature ramp. Our electrical and microstructural measurement results shown in sections 4.3 and 6.3 indicate that Ru and Ru-CGO films deposited at 40 mTorr are less dense compared to the films deposited at 10 mTorr. From XRR analyses results, the Ru-CGO films deposited at 40 mTorr (film porosity ~40 %) can be 40 % more porous compared to the 10 mTorr deposited films (film porosity ~28 %). FC4 and FC5 having anodes deposited at 40 mTorr both survived the temperature ramp followed by fuel switching and generated power with methane fuel. Both fuel cells exhibited mechanically intact membranes without cracks or fractures after fuel cell operations, as shown in **Fig. 7.3 (b)**. Fuel cell performance measurement results of FC4 and FC5 are shown in **Fig. 7.5 (a)** and **(b)**. FC4 exhibited maximum power of 31 mW cm<sup>-2</sup> with OCV of 0.96 V at 500 °C, while those at 455 °C were 19 mW cm<sup>-2</sup> and 0.89 V, respectively. With higher Ru content, FC5 exhibited maximum power of 275 mW cm<sup>-2</sup> and an OCV of 0.97 V at 485 °C, while those at 450 °C were 155 mW cm<sup>-2</sup> and 0.92 V, respectively. To the best of authors' knowledge, these are the first reports of functional self-supported thin film SOFCs with metal-ceramic composite electrodes, and moreover, with direct methane fuel feed. The power density at 485 °C is lower than what we have previously observed with nano-porous Ru metal anode  $\mu$ SOFCs [39], but still comparable to the high performance reported to date for methane-fueled fuel cells operated at equivalent temperatures [16]. Increase in OCV observed with operating temperature suggests improved catalytic activity of the electrodes. Improved performance of FC5 compared to FC4 is likely due to the increased catalytic activity due to increased amount of Ru and improved in-plane conductivity for current collection. As shown in **Fig. 6.9 (a)**, in-plane conductivity of the composite electrode is highly sensitive to the metal fraction. In fact, the Ru/CGO ratio of FC5

anodes (R3C1) is 30 % higher than FC4 (R7C3), and R3C1 films deposited at 40 mTorr exhibited 40 % higher conductivity than R7C3 films as shown in **Fig. 7.6**. These fuel cell test results also indicate that the crystallized CGO in the composite anodes offers ionic transport paths in composite electrodes, and are consistent with the XRD results of post annealed composite films discussed in section 6.3.



(a)



(b)

**Fig. 7.5** Performance of Ru-CGO composite anode/YSZ electrolyte/Pt cathode  $\mu$ SOFCs, (a) FC4 and (b) FC5, with room temperature humidified methane as the fuel. The composite anodes are R7C3 for FC4 and R3C1 for FC5. Open and closed symbols represent voltage and power density, respectively.

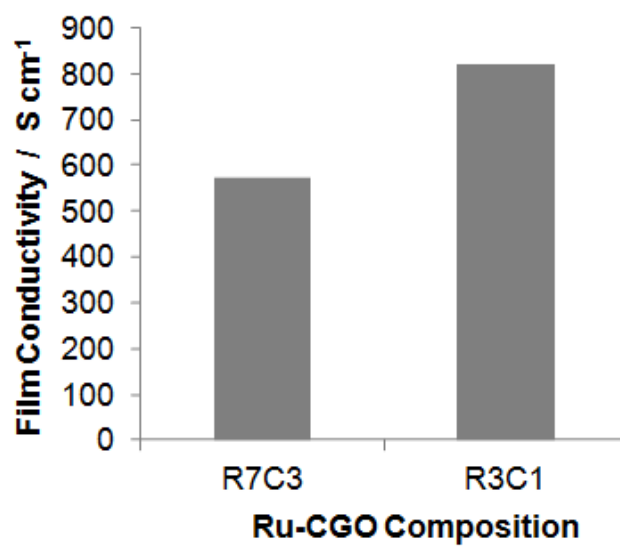


**Fig. 7.6** DC conductivity of 40 mTorr deposited films with different Ru/CGO ratios on single crystal sapphire substrates measured at room temperature.

### 7.3.2 Extended operation of micro-solid oxide fuel cells and microstructural investigations

In order to investigate microstructural stability of the Ru-CGO composite electrode, FC5 was tested over 3 h by keeping fuel cell at 500 °C under OCV condition, while I-V measurements were carried out every 15 min sweeping the cell voltage from 0.85 to 0.35 V and measuring the current. While the length of the test may seem relatively short, the results are expected to provide new insights into the field of thin film  $\mu$ SOFCs, where very limited studies exist on stability to date. For instance, Kerman et al. performed 12 h test of Pt/YSZ/Pt  $\mu$ SOFCs with hydrogen fuel at 400 °C under OCV condition, and found that the power density decreased by 50 % [57]. Degradation was attributed to instability in electrode microstructures. As presented in **Fig. 7.7 (a)**, peak power densities of the fuel cell (FC5) showed good stability for the first 2 h, and decreased to 62 % of the initial value after 3 h. **Fig. 7.7 (b)** shows the current density evolution in the voltage range of 0.6~0.75 V, where SOFCs are expected to operate in order to efficiently convert chemical energy to electrical energy. It is interesting to note that the current decrease at these operating voltages was relatively moderate (~25 %) compared to the decrease at peak power.

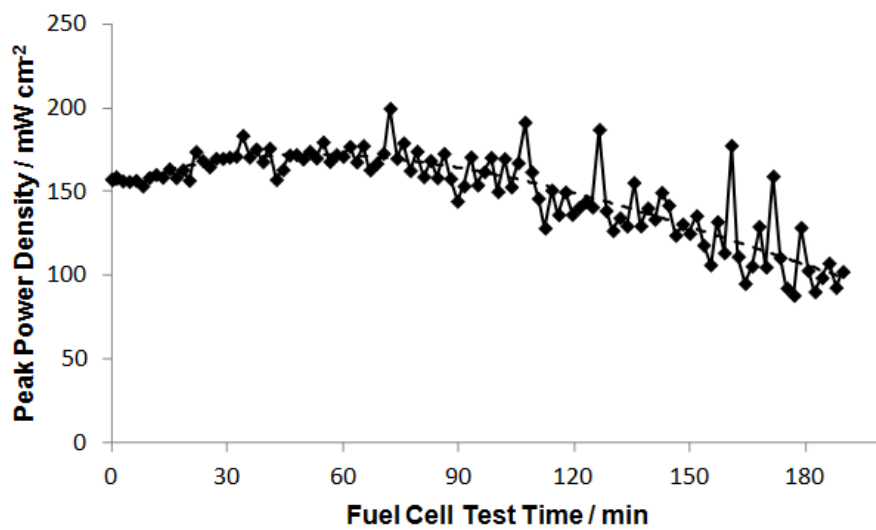
The SEM cross-sectional views of fractured  $\mu$ SOFC (FC5) after extended methane operation were studied to investigate structural integrity of the  $\mu$ SOFC and morphological evolution of the electrodes. **Figure 7.8 (a)** focuses on electrolyte, **(b)** on cathode, and **(c)** on anode. Note that the thin films are curled after membranes were fractured due to compressive internal stresses in Ru-CGO anodes. Good adhesions among Pt cathodes, YSZ electrolytes and Ru-CGO composite anodes were observed. The thickness of YSZ electrolyte was ~100 nm, Ru-CGO anodes and Pt cathodes were 30~40 nm. From the images, it is clearly observed that Ru-CGO anodes maintain finer morphology than Pt cathodes, suggesting better microstructural stability. Pure Pt electrodes may experience sintering at temperature as low as 400 °C and lead

to decrease in active area [85, 95]. As shown in **Fig. 7.9**, Pt cathodes after operation showed morphological deformation and decrease in triple phase boundary length, likely being the cause of performance decay observed.

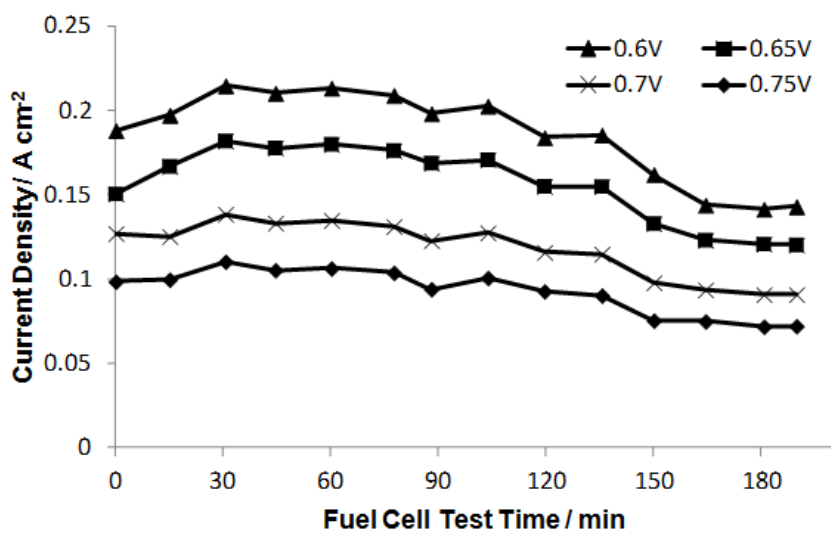
To take a closer look of morphologies and possible carbon depositions, planar SEM micrographs of composite anodes after the fuel cell tests are shown in **Fig. 7.2 (c)** for FC4 and **(d)** for FC5. No visible sign of carbon depositions, such as filaments, sheets or crystals was observed, as consistent with previous results with pure Ru metal anodes as shown in section 5.3. Trace carbon existence on the electrode surface may not be captured by SEM, however, if carbon deposition at the level that degrades fuel cell performance exists, microscopic evidence would be expected. Ruthenium is known to be catalytically active for steam and dry reforming [26, 27, 32], and also highly resistant to carbon depositions. The local coupling of these reforming reactions and its characteristics allow electrochemical reaction products, H<sub>2</sub>O and CO<sub>2</sub>, to be utilized in chemically converting methane to H<sub>2</sub> and CO. These species may be consumed as fuels and generate H<sub>2</sub>O and CO<sub>2</sub>, which can further aid reforming and accelerate the overall number of reactions [41]. Compared to the SEM micrographs of the anodes before fuel cell tests (**Fig. 7.2 (a)** and **(b)** for FC4 and FC5, respectively), the grain boundaries became clearer in both FC4 and FC5 anodes. Grain sizes after fuel cell operation were ~10 nm for FC4 and ~40 nm for FC5, not noticeably different from the initial sizes. This indeed indicates improved microstructural stability of Ru-CGO composite anodes compared to pure Ru metal anodes [39] and composite thin film anodes studied to date. It has been reported that in co-deposited Ni-YSZ composite electrodes, Ni particles can grow from <50 nm to the order of 300~500 nm in reducing atmosphere at elevated temperatures [68, 70]. The microstructural stability of the Ru-CGO composite anodes can be attributed to following reasons; the Ru-CGO electrodes are designed to be less porous, whereas Ni-ceramic electrodes in previous studies are intended to be porous by reduction of NiO to Ni. Denser composite films likely have more

stable nanostructure, inhibiting agglomeration of metal particles in open pores. Moreover, denser electrodes have less stress transfer to electrolytes during volume shrinkage accompanied by reduction of oxidized metal, which is a critical factor when fabricating composite electrodes on self-supported thin film electrolytes. Additionally, Ru is expected to have better microstructural stability compared to Ni due to its higher melting point (Ru: 2334 °C, Ni: 1455 °C). Finally, thin film electrolytes in  $\mu$ SOFCs allow reduced operation temperature, which suppresses metal agglomeration in the electrode.

**Figure 7.10** shows fuel cell current density evolution of a Ru-CGO composite anode  $\mu$ SOFC (FC5, anode composition Ru/CGO = 3/1) during constant voltage operation at 0.7 V, tested for more than 3 hours. The  $\mu$ SOFC temperature was kept constant at 455 °C while 3 % humidified methane was supplied as the fuel. Similar to the porous Ru anode  $\mu$ SOFC, intermittent oscillation of the fuel cell current was observed. The period of the oscillation was roughly 3 to 5 min, being shorter than that of the Ru anode  $\mu$ SOFC. Mechanism of the oscillation is discussed in detail in chapter 5.

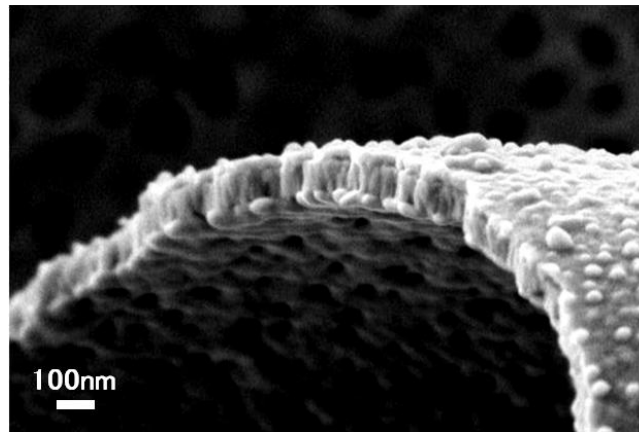


(a)

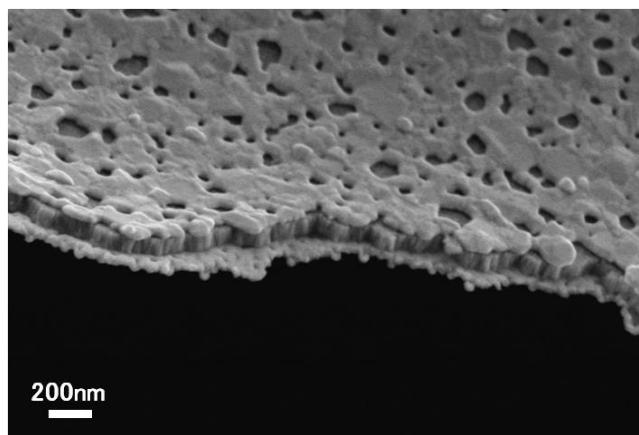


(b)

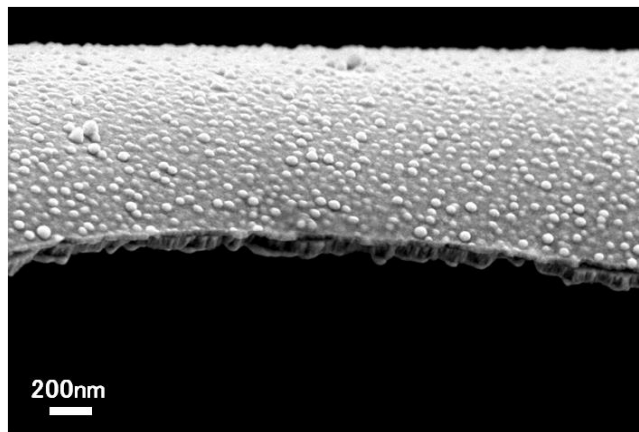
**Fig. 7.7** (a) Evolution of maximum power density during extended operation of FC5 at 500 °C. (b) Current density evolution at different cell voltages during the extended operation.



(a)



(b)



(c)

**Fig. 7.8** SEM cross-sectional views of FC5 after extended fuel cell operation focused on (a) YSZ electrolyte, (b) Pt cathode, and (c) Ru-CGO composite anode.

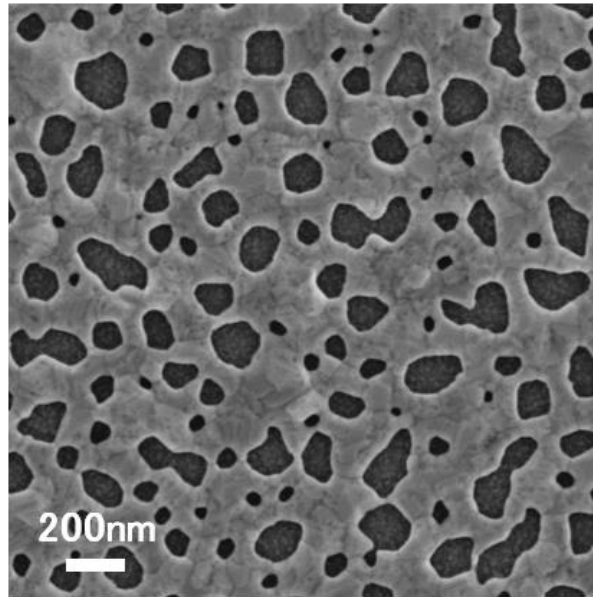


**Fig. 7.9** SEM micrograph of Pt cathode on FC5 after extended fuel cell operation.

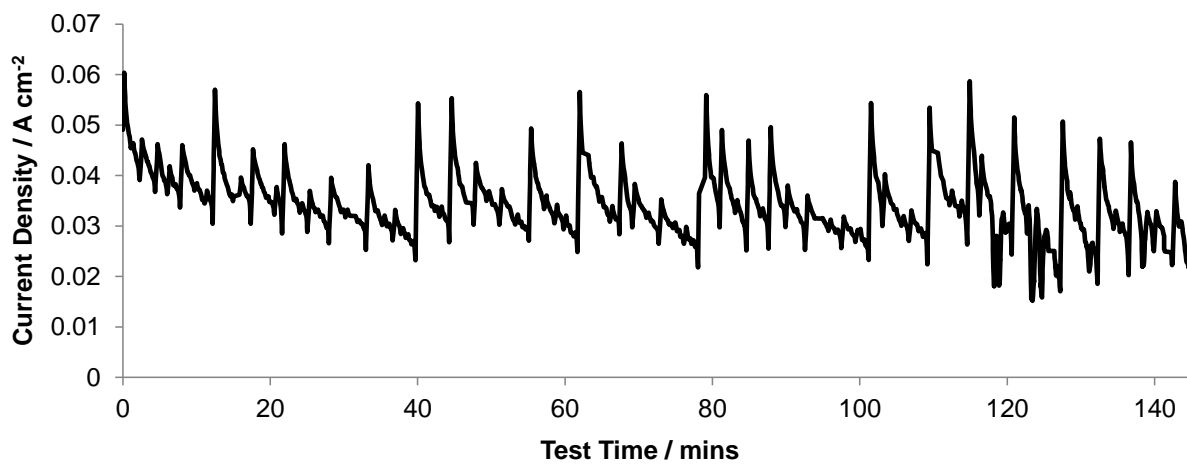


**Fig. 7.10** Current density evolution of a Ru-CGO nano-composite anode  $\mu$ SOFC (FC5, Ru/CGO = 3/1), during extended operation with 3 % humidified methane as fuel, at cell temperature of 455 °C and cell voltage of 0.7 V.

## 7.4 Conclusions

Thin film  $\mu$ SOFCs with Ru-CGO nano-composite thin film anodes, YSZ electrolytes, and Pt cathodes have been fabricated and tested for direct methane utilization. A thermal-mechanically stable  $\mu$ SOFC structure was achieved by relaxing internal residual stresses in the Ru-CGO composite anodes. This was achieved through tuning thin film deposition pressure and increasing film porosities. Morphology of the composite anodes were found to be smooth nano-crystalline. Fuel cells with stress-relaxed Ru-CGO composite anodes were successfully operated with 3 % humidified methane as fuel and air as the oxidant. OCV under hydrogen fuel increased from 0.14V to 0.98V by increasing Ru/CGO ratio from 1/1 to 7/3. After optimizing the Ru/CGO ratio to 3/1, an open circuit voltage of 0.97 V and a peak power density of 275 mW cm<sup>-2</sup> were achieved at 485 °C. An extended fuel cell operation at OCV was performed at 500 °C and the fuel cell retained a 62% of the initial peak power density. Analysis following the extended fuel cell operation indicated improved microstructural stability of Ru-CGO nano-composite anodes relative to nano-porous metal Ru anodes and Pt cathodes.



## Chapter 8: Conclusions

In this work, characteristics and performance of nano-porous Ru thin films and Ru-CGO nano-composite thin films as anodes for direct hydrocarbon fueled  $\mu$ SOFCs is explored. Detailed material characterizations on Ru and Ru-CGO thin films were investigated as well as performance and electrochemical behavior of Ru and Ru-CGO anode  $\mu$ SOFCs.

In chapter 1, general introduction to solid oxide fuel cell technologies were made, followed by showing specific examples of the past works towards direct hydrocarbon utilization, and referring superior characteristics of ruthenium as a SOFC anode material. Next, general overview of thin film micro-SOFCs were made and previous works on direct hydrocarbon utilization along with trials on development of nano-composite anodes were depicted. At the end, the aim of this entire work has been stated in details.

In chapter 2, microfabrication processes developed for thin film  $\mu$ SOFCs based on silicon technology were reported and discussed in detail based on previous reports, to apply them on direct hydrocarbon  $\mu$ SOFCs with Ru thin film anodes. Properties of YSZ electrolyte films deposited at 550 °C and without substrate heating were compared. It was found that 550 °C deposited electrolytes showed more buckled geometry, and was more thermal-mechanically stable under heating to fuel cell operation temperature. The 550 °C deposited electrolytes showed polycrystalline structure by XRD where those deposited without heating showed no distinct peak. The room temperature deposited YSZ film experiences grain growths during temperature ramp at fuel cell test, and tend to break with the increase of tensile stress within the membrane. It was decided to use 550 °C deposited electrolytes for further studies in this work.

In chapter 3, a thermal-electrochemical integrated one dimensional simulation model was newly developed for disc geometry  $\mu$ SOFCs to evaluate their operation conditions. With regard to heat transfer models, heat radiation to the ambient from Pt cathode surface, lateral heat conduction to the substrates along multi-layered thin films, heat convection between anode electrodes and the fuel flow were considered. Temperature dependent I-V characteristics, heat generation due to electrochemical overvoltage losses, through-plane and in-plane IR losses were considered in the electrochemical model. Impact of fuel cell operation voltage, wall temperature, radiation factor, a closed system and electrode degradation were investigated using the constructed simulation model. Results are summarized as follows;

- Impact of fuel cell operation voltage (terminal voltage): Due to a strong radiation cooling effect, temperature close to the center of the cell was lower than the wall temperature at terminal voltages of 0.5~0.9 V. At 0.3 V, heat generation within the cell overcame heat radiation.
- Impact of wall temperature: Average cell temperatures were always lower than the controlled wall temperature for 4~5 °C, due to dominant heat radiation effect.
- Impact of emissivity: Fuel cell temperature distribution was strongly sensitive to the emissivity  $\varepsilon$ . At  $\varepsilon = 0.6$ , the cell center temperature dropped ~10 °C from the wall temperature where at  $\varepsilon = 0.1$ , the drop was ~1 °C when operated at 0.7 V. This indicates that in an open system, radiation is a dominant heat transfer mechanism that determines the fuel cell temperature.
- Impact of a closed system: With heat loss due to radiation removed, the cell temperature is always higher than the wall temperature. The maximum cell temperature was about 11 °C higher than the wall temperature at cell voltage of 0.3 V. In-plane heat conduction to the wall removes the heat generated by electrochemical reactions.
- Degradation of electrode electrochemical performance: Exchange current density was

reduced to 57 % to simulate degraded condition. At 450 °C wall temperature and cell terminal voltage of 0.7 V, effect of change in heat generation to the cell temperature distribution was minor due to dominant heat radiation and conduction.

Overall, temperature distributions within a thin film  $\mu$ SOFC was rather uniform regardless of operation conditions, being in the range of +/- 10 °C. This is mainly due to dominant contributions of surface radiation to environment and lateral heat conduction to the wall.

In chapter 4, basic properties of nano-porous Ru thin films on substrates were investigated targeting  $\mu$ SOFC anodes for direct methane utilization. Effects of annealing on the sheet resistance and surface morphology of Ru thin films were investigated, and synthesis protocols were optimized for fuel cell fabrication. Following characteristics were revealed.

- Control window for Ru thin film deposition: Ru thin film deposition rates ranged from 0.2 to 12.3 nm min<sup>-1</sup> resulting in a control range of two orders of magnitude, by varying target power from 50 to 200 W and deposition pressure from 10 to 75 mTorr.
- In-plane electrical conductivity path formation: For 75 mTorr deposited Ru films, sheet resistance drops significantly between film thicknesses of 24 and 48 nm, indicating critical thickness for in-plane conduction path formation.
- Film porosities of Ru thin films: 10 mTorr deposited films showed significantly higher in-plane conductivity compared to 40 and 75 mTorr deposited films, indicating deposition pressure above 40 mTorr results in more porous morphology. Analysis on critical angles derived from XRR measurements revealed that 75 mTorr deposited films are even more porous (or less dense) compared to 40 mTorr deposited films.
- Thin film microstructure and stability: Deposited Ru films showed highly granular and porous texture. After 500 °C annealing in vacuum, the porous films showed extensive grain growths from 10~20 nm to 30~40 nm range. Highly granular textures were retained.

- Microstructure of Ru thin films at electrolyte interface: TEM cross-sectional analysis of Ru thin films on YSZ substrates revealed nano-scale columnar structures with longitudinal lengths of ~40 nm and widths of ~10 nm. Dense Ru layer with thickness of ~2 nm exists covering the YSZ surface. After annealed in vacuum, triple phase boundaries were formed with an exposure of YSZ to gas phase due to agglomeration and dewetting of Ru columns, still maintaining nm scale morphologies.

In chapter 5, thin film  $\mu$ SOFCs with nano-porous Ru anodes, YSZ electrolytes, and Pt cathodes have been fabricated based on the insights obtained in chapter 4, and its performance with direct methane supply was evaluated. The porous Ru anode  $\mu$ SOFCs were successfully operated with 3 % humidified methane as the fuel with peak power density of 450 mW cm<sup>-2</sup>. The performance of  $\mu$ SOFCs with dry methane and natural gas was comparable, and peak power density of 800 mW cm<sup>-2</sup> at 530 °C with 3 % humidified natural gas as the fuel was achieved. Following related characteristics were revealed.

- ◆ Morphology of Ru anodes in  $\mu$ SOFC platform: Ru anodes deposited on self-supported  $\mu$ SOFC structure showed an isolated island-like structure with a nano-scale granular morphology at the electrolyte interface. This nano-scale morphology at the electrolyte interface was similar to those seen with films deposited on substrates in chapter 4.
- ◆ Fuel cell performance with direct supply of 3 % humidified methane: At 500 °C, the fuel cell with Ru anodes at 15 minutes deposition time exhibited peak power density of 450 mW cm<sup>-2</sup> with an OCV of 0.71 V. Micro-SOFCs with thinner and thicker electrodes (7.5 and 25 min depositions) resulted in 25 % and 60 % reduction in peak power densities.
- ◆ Microscopic integrity of Ru anode  $\mu$ SOFCs: Good adhesion among the electrolytes and electrodes were observed after fuel cell operation, based on cross-sectional FIB-SEM studies.

- ◆ Ru anode microstructural stability under fuel cell operation: Microstructures of Ru anodes after methane operation showed distinct difference from those of Pt electrode in hydrogen in the literature, exhibiting better stability. Ru anode morphology change was more suppressed under methane operation than under hydrogen operation.
  - ◆ Possible risk of carbon depositions: No visible carbon formation was observed after methane operation thorough SEM. However, increase of carbon signal was observed in AES and XPS analyses. Increase in oxygen signal was also observed, indicating existence of carbon containing methane reaction intermediates on the Ru anode surface.
  - Fuel cell performance with various fuels: Ru anode  $\mu$ SOFCs showed comparable performance under dry methane and natural gas fuels. At 500 °C, the  $\mu$ SOFC with methane fuel performed peak power density of 440 mW cm<sup>-2</sup>, where with natural gas fuel it was 410 mW cm<sup>-2</sup>. The fuel cell had a peak power density of 635 mW cm<sup>-2</sup> at 525 °C with dry methane, and 800 mW cm<sup>-2</sup> at 530 °C with 3 % humidified natural gas. There was no noticeable difference in Ru anode morphology after methane and natural gas operation.
- Quasi-periodic oscillatory behavior of the cell current was observed when the  $\mu$ SOFC was continuously operated at constant voltage of 0.7 V. Mechanisms leading to the oscillatory behavior are discussed based on Ru anode surface coverage states, change in effective exchange current densities, change in anode overvoltage, and ignition of methane combustion that cleans the oxidized Ru surface.
- ◆ Behavior of fuel cell current under constant voltage operation: Micro-SOFCs showed quasi-periodic oscillatory behavior of fuel cell current under constant voltage (0.7 V) operation with 3 % humidified methane fuel. The oscillation period was 20~40 minutes, where total test-time extended over 180 minutes.
  - ◆ Changes in surface oxidation states of Ru anodes: It was found that oxidation states of Ru anode surfaces after operation strongly depends on the fuel. The oxygen peak was stronger

with methane and natural gas fueled anodes compared to as-prepared and hydrogen fueled anodes. A third oxide species at 532.2 eV appears after operation with hydrocarbon fuels and was attributed to oxygen-carbon related intermediate products of the methane electrochemical reaction.

- ◆ Potential origin of the oscillation: The mechanism of the oscillation is discussed based on enhanced surface oxidation states of methane operated Ru anodes identified by change in effective exchange current densities, and self-cleaning due to reaction between absorbed intermediates and oxygen. From detailed current measurements, Ru surface cleaning mechanism was further discussed. Sudden activity loss at the end of an oscillation cycle leads to a spike increase in anode overvoltage, which may lead to methane combustion ignition and a subsequent Ru surface reduction due to a temperature increase.

In chapter 6, basic properties of Ru-CGO composite thin films were investigated targeting  $\mu$ SOFC anodes for direct methane utilization. Ru-CGO thin films were found to have improved microstructural stability compared to porous Ru thin films. Following characteristics were revealed.

- Control window of Ru-CGO co-depositions and thin film composition: The nominal control window for Ru-CGO co-deposition based on deposition rates was defined to be in the range of  $\text{Ru/CGO} = 2/3 \sim 3/1$ , where the deposition pressure was 10~40 mTorr. Calculated volumetric ratios of Ru/CGO in composite films from XPS measurements were in a fair agreement with targeted values.
- Thin film morphology: Deposition on single crystal sapphire, sc-YSZ and  $\text{Si}_3\text{N}_4/\text{Si}$  substrates showed smooth nano-crystalline morphology with grain sizes of ~10 nm. Composite films on polycrystalline YSZ thin film showed highly granular morphology with primary grain sizes of ~10 nm and secondary pillars as large as 70~100 nm, as

identified by cross-sectional SEM analysis.

- Crystalline phases in composite thin films: Hexagonal Ru and cubic fluorite CGO phases were confirmed after annealing the composite films in H<sub>2</sub>/Ar. The existence of crystalline CGO phase indicates ionic transport capability in the composite electrode. No secondary phases were observed, indicating formation of cermet like structure of Ru and CGO grains. Intensity of Ru and CGO peaks were strongly dependent on designed Ru/CGO ratios.
- In-plane electrical conduction path formation: Increasing Ru content lead to exponential increase in in-plane conductivity. The high volumetric Ru content of more than 50% was required for conduction path formation, indicating gradual two dimensional percolation.
- Porosity of Ru-CGO thin films: Increasing deposition pressure from 10, 40 and to 75 mTorr lead to a decrease in film conductivity, indicating more porous or loose structure in the thin film. Analysis on critical angles derived from XRR measurements revealed that the film porosity linearly increased from 27 to 53 % by increasing the deposition pressure from 10 to 75 mTorr.
- Microstructural stability under elevated temperature: Increase in in-plane conductivity of Ru-CGO nano-composite film was 1/10 of nano-porous Ru films under thermal annealing in H<sub>2</sub>/Ar environment at 500 °C, indicating improved microstructural stability of the composite film. The superior microstructural stability was also confirmed by investigating morphology evolution of the films by SEM. Morphology changes were negligible for Ru-CGO films, where significant grain growths and coarsening were observed for nano-porous Ru films.

In chapter 7, thin film  $\mu$ SOFCs with Ru-CGO nano-composite thin film anodes, YSZ electrolytes, and Pt cathodes have been fabricated and tested for direct methane utilization, based on the insights obtained from the characterizations done in chapter 6. Stress-relaxed Ru-

CGO thin film anodes were fabricated on  $\mu$ SOFC platforms by controlling deposition pressures, and lead to fabrication of thermal-chemically stable  $\mu$ SOFC structures. The Ru-CGO anode  $\mu$ SOFCs were successfully operated with 3 % humidified methane as the fuel with peak power density of  $275 \text{ mW cm}^{-2}$ , with improved nano-structural stability of the anode in operation. Following characteristics were revealed.

- ◆ Morphology of Ru-CGO anodes on  $\mu$ SOFC platform: Ru-CGO anodes deposited in  $\mu$ SOFC platform showed smooth nano-crystalline morphology, being similar to the morphology of films deposited on smooth substrates in chapter 6.
- ◆ Thermal-mechanical microscopic structural integrity of the Ru-CGO anode  $\mu$ SOFC: Micro-SOFCs with 10 mTorr deposited Ru-CGO anodes failed due to membrane fractures upon methane supply and heating to operating temperature. The failures may be attributed to chemical volume change of Ru due to changes in redox conditions at the anode. Increasing deposition pressure to 40 mTorr relaxed the compressive stress of the anode and improved the thermal-mechanical integrity of  $\mu$ SOFCs.
- ◆ Fuel cell performance with direct supply of 3 % humidified methane: The OCV under hydrogen fuel increased from 0.14 V to 0.98 V with increasing Ru/CGO ratio from 1/1 to 7/3. The fuel cell with Ru-CGO anode (Ru/CGO = 7/3) exhibited peak power density of  $31 \text{ mW cm}^{-2}$  with an OCV of 0.96 V at  $500 \text{ }^\circ\text{C}$ , with direct supply of 3 % humidified methane. By increasing Ru/CGO ratio to 3/1, the peak power density improved to  $275 \text{ mW cm}^{-2}$  with an OCV of 0.97 V at  $485 \text{ }^\circ\text{C}$ .
- ◆ Long term stability: The peak power density of the fuel cell decreased to 62 % of the initial value after three hours of extended OCV run with methane fuel at  $500 \text{ }^\circ\text{C}$ . Pt cathodes showed significant morphological deformation and decrease in triple boundary length, while grain sizes in Ru-CGO anodes were not noticeably different from their initial states. No visible sign of carbon deposition was observed.

As a recapitulation of the main results, nano-porous Ru and Ru-CGO nano-composite thin films were investigated as  $\mu$ SOFC anodes for direct hydrocarbon utilizations. Thermal-electrochemical integrated one dimensional simulation model was developed and temperature, current distribution under different operating conditions were discussed, revealing rather consistent temperature distribution in  $\mu$ SOFCs due to dominant radiation and conduction effects. Based on microstructure investigation and property analyses results on the thin films,  $\mu$ SOFCs with Ru based anodes were fabricated and demonstrated high power density of  $\sim 800$  mW cm<sup>-2</sup> at 500 °C range. Quasi-periodic oscillations were observed under constant voltage operation and potential mechanisms were discussed based on transitions of electrode surface coverage states, changes in electrochemical overvoltage and related reaction activities. Microstructural stability of thin film anodes were investigated and newly developed Ru-CGO nano-composites proved to have improved stability compared to porous metal counterparts, both on substrates and as  $\mu$ SOFC anodes. Further studies are desired for advancing development in the area of low temperature direct hydrocarbon  $\mu$ SOFCs, such as in-situ analysis on the oscillatory behavior, development in processes of enlarging the active area and investigation in high performance thin film cathodes.



## References

- [1] E.P. Murray, T. Tsai, S.A. Barnett, "A direct-methane fuel cell with a ceria-based anode", *Nature*, 400 (1999) 649-651.
- [2] Z.P. Shao, S.M. Haile, J. Ahn, P.D. Ronney, Z.L. Zhan, S.A. Barnett, "A thermally self-sustained micro solid-oxide fuel-cell stack with high power density", *Nature*, 435 (2005) 795-798.
- [3] T. Hibino, A. Hashimoto, M. Yano, M. Suzuki, M. Sano, "Ru-catalyzed anode materials for direct hydrocarbon SOFCs", *Electrochim. Acta*, 48 (2003) 2531-2537.
- [4] S. McIntosh, J.M. Vohs, R.J. Gorte, "Effect of precious-metal dopants on SOFC anodes for direct utilization of hydrocarbons", *Electrochem. Solid-State Lett.*, 6 (2003) A240-A243.
- [5] S. McIntosh, R.J. Gorte, "Direct hydrocarbon solid oxide fuel cells", *Chem. Rev.*, 104 (2004) 4845-4865.
- [6] A. Atkinson, S. Barnett, R.J. Gorte, J.T.S. Irvine, A.J. McEvoy, M. Mogensen, S.C. Singhal, J. Vohs, "Advanced anodes for high-temperature fuel cells", *Nat. Mater.*, 3 (2004) 17-27.
- [7] J.B. Goodenough, Y.H. Huang, "Alternative anode materials for solid oxide fuel cells", *J. Power Sources*, 173 (2007) 1-10.
- [8] S.D. Park, J.M. Vohs, R.J. Gorte, "Direct oxidation of hydrocarbons in a solid-oxide fuel cell", *Nature*, 404 (2000) 265-267.
- [9] J. Mermelstein, M. Millan, N. Brandon, "The impact of steam and current density on carbon formation from biomass gasification tar on Ni/YSZ, and Ni/CGO solid oxide fuel cell anodes", *J. Power Sources*, 195 (2010) 1657-1666.
- [10] O.A. Marina, M. Mogensen, "High-temperature conversion of methane on a composite gadolinia-doped ceria-gold electrode", *Appl. Catal. a-Gen.*, 189 (1999) 117-126.

- [11] M. Mogensen, K. Kammer, "Conversion of hydrocarbons in solid oxide fuel cells", *Annu. Rev. Mater. Res.*, 33 (2003) 321-331.
- [12] J.W. Fergus, R. Hui, X. Li, D.P. Wilkinson, J. Zhang, in: *Green Chemistry and Chemical Engineering*, CRC Press, 2009.
- [13] S. Yoon, Y. Kim, S. Kim, J. Bae, "Effects of low hydrocarbons on the solid oxide fuel cell anode", *J. Solid State Electr.*, 14 (2010) 1793-1800.
- [14] T. Hibino, A. Hashimoto, K. Asano, M. Yano, M. Suzuki, M. Sano, "An intermediate-temperature solid oxide fuel cell providing higher performance with hydrocarbons than with hydrogen", *Electrochem. Solid St.*, 5 (2002) A242-A244.
- [15] B.K. Lai, K. Kerman, S. Ramanathan, "Methane-fueled thin film micro-solid oxide fuel cells with nanoporous palladium anodes", *J. Power Sources*, 196 (2011) 6299-6304.
- [16] T. Suzuki, T. Yamaguchi, K. Hamamoto, Y. Fujishiro, M. Awano, N.M. Sammes, "A functional layer for direct use of hydrocarbon fuel in low temperature solid-oxide fuel cells", *Energy Environ. Sci.*, 4 (2011) 940-943.
- [17] B.C.H. Steele, "Fuel-cell technology - Running on natural gas", *Nature*, 400 (1999) 619-621.
- [18] D.J.L. Brett, A. Atkinson, N.P. Brandon, S.J. Skinner, "Intermediate temperature solid oxide fuel cells", *Chem. Soc. Rev.*, 37 (2008) 1568-1578.
- [19] R.J. Gorte, S. Park, J.M. Vohs, C.H. Wang, "Anodes for direct oxidation of dry hydrocarbons in a solid-oxide fuel cell", *Adv. Mater.*, 12 (2000) 1465-1469.
- [20] L. Yang, S.Z. Wang, K. Blinn, M.F. Liu, Z. Liu, Z. Cheng, M.L. Liu, "Enhanced sulfur and coking tolerance of a mixed ion conductor for SOFCs:  $\text{BaZr}_{0.1}\text{Ce}_{0.7}\text{Y}_{0.2-x}\text{Yb}_x\text{O}_{3-\text{delta}}$ ", *Science*, 326 (2009) 126-129.

- [21] X.J. Chen, Q.L. Liu, S.H. Chan, N.P. Brandon, K.A. Khor, "High performance cathode-supported SOFC with perovskite anode operating in weakly humidified hydrogen and methane", *Electrochem. Commun.*, 9 (2007) 767-772.
- [22] Y.B. Lin, Z.L. Zhan, J. Liu, S.A. Barnett, "Direct operation of solid oxide fuel cells with methane fuel", *Solid State Ionics*, 176 (2005) 1827-1835.
- [23] J.A. Liu, S.A. Barnett, "Operation of anode-supported solid oxide fuel cells on methane and natural gas", *Solid State Ionics*, 158 (2003) 11-16.
- [24] K. Wang, R. Ran, Z.P. Shao, "Methane-fueled IT-SOFCs with facile in situ inorganic templating synthesized mesoporous  $\text{Sm}_{0.2}\text{Ce}_{0.8}\text{O}_{1.9}$  as catalytic layer", *J. Power Sources*, 170 (2007) 251-258.
- [25] P. Vernoux, J. Guindet, M. Kleitz, "Gradual internal methane reforming in intermediate-temperature solid-oxide fuel cells", *J. Electrochem. Soc.*, 145 (1998) 3487-3492.
- [26] M.J. Saeki, H. Uchida, M. Watanabe, "Noble-metal catalysts highly-dispersed on Sm-doped ceria for the application to internal reforming solid oxide fuel-cells operated at medium-temperature", *Catal. Lett.*, 26 (1994) 149-157.
- [27] D. Qin, J. Lapszewicz, "Study of mixed steam and  $\text{CO}_2$  reforming of  $\text{CH}_4$  to syngas on MgO-supported metals", *Catal. Today*, 21 (1994) 551-560.
- [28] I.I. Bobrova, N.N. Bobrov, V.V. Chesnokov, V.N. Parmon, "Catalytic steam reforming of methane: New data on the contribution of homogeneous radical reactions in the gas phase: II. A ruthenium catalyst", *Kinet. Catal.*, 42 (2001) 805-812.
- [29] K. Takehira, T. Ohi, T. Miyata, M. Shiraga, T. Sano, "Steam reforming of  $\text{CH}_4$  over Ni-Ru catalysts supported on Mg-Al mixed oxide", *Top. Catal.*, 42-43 (2007) 471-474.
- [30] J.X. Chen, C.C. Yao, Y.Q. Zhao, P.H. Jia, "Synthesis gas production from dry reforming of methane over  $\text{Ce}_{0.75}\text{Zr}_{0.25}\text{O}_2$ -supported Ru catalysts", *Int. J. Hydrogen Energy*, 35 (2010) 1630-1642.

- [31] D. Ding, Z.B. Liu, L. Li, C.R. Xia, "An octane-fueled low temperature solid oxide fuel cell with Ru-free anodes", *Electrochem. Commun.*, 10 (2008) 1295-1298.
- [32] M.J. Hei, H.B. Chen, J. Yi, Y.J. Lin, Y.Z. Lin, G. Wei, D.W. Liao, "CO<sub>2</sub>-reforming of methane on transition metal surfaces", *Surf. Sci.*, 417 (1998) 82-96.
- [33] S. Bebelis, S. Neophytides, N. Kotsionopoulos, N. Triantafyllopoulos, M.T. Colomer, J. Jurado, "Methane oxidation on composite ruthenium electrodes in YSZ cells", *Solid State Ionics*, 177 (2006) 2087-2091.
- [34] C. Elmasides, D.I. Kondarides, S.G. Neophytides, X.E. Verykios, "Partial oxidation of methane to synthesis gas over Ru/TiO<sub>2</sub> catalysts: Effects of modification of the support on oxidation state and catalytic performance", *J. Catal.*, 198 (2001) 195-207.
- [35] M.G. Poirier, J. Trudel, D. Guay, "Partial oxidation of methane over ruthenium catalysts", *Catal. Lett.*, 21 (1993) 99-111.
- [36] A.V. Simakov, S.N. Pavlova, N.N. Sazanova, V.A. Sadykov, O.I. Snegurenko, V.A. Rogov, V.N. Paramon, I.A. Zolotarskii, V.A. Kuzmin, E.M. Moroz, "Oscillations in partial oxidation of methane to syngas over supported mixed oxides promoted with Pt", *Chem. Sustain. Dev.*, 11 (2003) 263-270.
- [37] M. Lo Faro, D. La Rosa, G. Monforte, V. Antonucci, A.S. Arico, P. Antonucci, "Propane conversion over a Ru/CGO catalyst and its application in intermediate temperature solid oxide fuel cells", *J. Appl. Electrochem.*, 37 (2007) 203-208.
- [38] Y. Takagi, S. Adam, S. Ramanathan, "Nanostructured ruthenium – gadolinia-doped ceria composite anodes for thin film solid oxide fuel cells", *J. Power Sources*, 217 (2012) 543-553.
- [39] Y. Takagi, B.K. Lai, K. Kerman, S. Ramanathan, "Low temperature thin film solid oxide fuel cells with nanoporous ruthenium anodes for direct methane operation", *Energy Environ. Sci.*, 4 (2011) 3473-3478.

- [40] M. Chai, M. Machida, K. Eguchi, H. Arai, "Promotion of methane steam reforming using ruthenium-dispersed microporous alumina membrane reactor", *Chem. Lett.*, (1993) 41-44.
- [41] J.T.S. Irvine, A. Sauvet, "Improved oxidation of hydrocarbons with new electrodes in high temperature fuel cells", *Fuel Cells*, 1 (2001) 205-210.
- [42] J.R. Rostrupnielsen, J.H.B. Hansen, "CO<sub>2</sub>-reforming of methane over transition-metals", *J. Catal.*, 144 (1993) 38-49.
- [43] B.C.H. Steele, A. Heinzl, "Materials for fuel-cell technologies", *Nature*, 414 (2001) 345-352.
- [44] X. Chen, N.J. Wu, L. Smith, A. Ignatiev, "Thin-film heterostructure solid oxide fuel cells", *Appl. Phys. Lett.*, 84 (2004) 2700-2702.
- [45] A. Ignatiev, X. Chen, N.J. Wu, Z.G. Lu, L. Smith, "Nanostructured thin solid oxide fuel cells with high power density", *Dalton Trans.*, (2008) 5501-5506.
- [46] A. Evans, A. Bieberle-Hutter, J.L.M. Rupp, L.J. Gauckler, "Review on microfabricated micro-solid oxide fuel cell membranes", *J. Power Sources*, 194 (2009) 119-129.
- [47] T. Ishihara, M. Honda, T. Shibayama, H. Minami, H. Nishiguchi, Y. Takita, "Intermediate temperature solid oxide fuel cells using a new LaGaO<sub>3</sub> based oxide ion conductor - I. Doped SmCoO<sub>3</sub> as a new cathode material", *J. Electrochem. Soc.*, 145 (1998) 3177-3183.
- [48] T. Ishihara, H. Matsuda, Y. Takita, "Doped LaGaO<sub>3</sub> perovskite-type oxide as a new oxide ionic conductor", *J. Am. Chem. Soc.*, 116 (1994) 3801-3803.
- [49] A.J. Jacobson, "Materials for solid oxide fuel cells", *Chem. Mater.*, 22 (2010) 660-674.
- [50] E.D. Wachsman, K.T. Lee, "Lowering the temperature of solid oxide fuel cells", *Science*, 334 (2011) 935-939.

- [51] J.S. Ahn, H. Yoon, K.T. Lee, M.A. Camaratta, E.D. Wachsman, "Performance of IT-SOFC with  $\text{Ce}_{0.9}\text{Gd}_{0.1}\text{O}_{1.95}$  functional layer at the interface of  $\text{Ce}_{0.9}\text{Gd}_{0.1}\text{O}_{1.95}$  electrolyte and Ni- $\text{Ce}_{0.9}\text{Gd}_{0.1}\text{O}_{1.95}$  anode", *Fuel Cells*, 9 (2009) 643-649.
- [52] C.W. Sun, U. Stimming, "Recent anode advances in solid oxide fuel cells", *J. Power Sources*, 171 (2007) 247-260.
- [53] C. Peters, A. Weber, E. Ivers-Tiffée, "Nanoscaled  $(\text{La}_{0.5}\text{Sr}_{0.5})\text{CoO}_{3-\text{delta}}$  thin film cathodes for SOFC application at  $500 \text{ degrees C} < T < 700 \text{ degrees C}$ ", *J. Electrochem. Soc.*, 155 (2008) B730-B737.
- [54] J. Hayd, L. Dieterle, U. Guntow, D. Gerthsen, E. Ivers-Tiffée, "Nanoscaled  $\text{La}_{0.6}\text{Sr}_{0.4}\text{CoO}_{3-\text{delta}}$  as intermediate temperature solid oxide fuel cell cathode: Microstructure and electrochemical performance", *J. Power Sources*, 196 (2011) 7263-7270.
- [55] C.D. Baertsch, K.F. Jensen, J.L. Hertz, H.L. Tuller, S.T. Vengallatore, S.M. Spearing, M.A. Schmidt, "Fabrication and structural characterization of self-supporting electrolyte membranes for a micro solid-oxide fuel cell", *J. Mater. Res.*, 19 (2004) 2604-2615.
- [56] H. Huang, M. Nakamura, P.C. Su, R. Fasching, Y. Saito, F.B. Prinz, "High-performance ultrathin solid oxide fuel cells for low-temperature operation", *J. Electrochem. Soc.*, 154 (2007) B20-B24.
- [57] K. Kerman, B.K. Lai, S. Ramanathan, "Pt/ $\text{Y}_{0.16}\text{Zr}_{0.84}\text{O}_{1.92}$ /Pt thin film solid oxide fuel cells: Electrode microstructure and stability considerations", *J. Power Sources*, 196 (2011) 2608-2614.
- [58] P.C. Su, C.C. Chao, J.H. Shim, R. Fasching, F.B. Prinz, "Solid oxide fuel cell with corrugated thin film electrolyte", *Nano Lett.*, 8 (2008) 2289-2292.
- [59] S. Guerrero, P. Araya, E.E. Wolf, "Methane oxidation on Pd supported on high area zirconia catalysts", *Appl. Catal. a-Gen.*, 298 (2006) 243-253.

- [60] U.P. Muecke, D. Beckel, A. Bernard, A. Bieberle-Hutter, S. Graf, A. Infortuna, P. Muller, J.L.M. Rupp, J. Schneider, L.J. Gauckler, "Micro solid oxide fuel cells on glass ceramic substrates", *Adv. Func. Mat.*, 18 (2008) 3158-3168.
- [61] H.S. Spacil, "Electrical device including nickel-containing stabilized zirconia electrode", US patent 3558360, 1970.
- [62] E. Rezugina, A.L. Thomann, H. Hidalgo, P. Brault, V. Dolique, Y. Tessier, "Ni-YSZ films deposited by reactive magnetron sputtering for SOFC applications", *Surf. Coat. Tech.*, 204 (2010) 2376-2380.
- [63] S. Jou, T.H. Wu, "Thin porous Ni-YSZ films as anodes for a solid oxide fuel cell", *J. Phys. Chem. Solids*, 69 (2008) 2804-2812.
- [64] G.J. La, J. Hertz, H. Tuller, Y. Shao-Horn, "Microstructural. features of RF-sputtered SOFC anode and electrolyte materials", *J. Electroceram.*, 13 (2004) 691-695.
- [65] L.S. Wang, S.A. Barnett, "Sputter-deposited medium-temperature solid oxide fuel-cells with multilayer electrolytes", *Solid State Ionics*, 61 (1993) 273-276.
- [66] T. Tsai, S.A. Barnett, "Increased solid-oxide fuel cell power density using interfacial ceria layers", *Solid State Ionics*, 98 (1997) 191-196.
- [67] H.S. Noh, J.W. Son, H. Lee, H.S. Song, H.W. Lee, J.H. Lee, "Low temperature performance improvement of sofc with thin film electrolyte and electrodes fabricated by pulsed laser deposition", *J. Electrochem. Soc.*, 156 (2009) B1484-B1490.
- [68] H.S. Noh, J.W. Son, H. Lee, H.I. Ji, J.H. Lee, H.W. Lee, "Suppression of Ni agglomeration in PLD fabricated Ni-YSZ composite for surface modification of SOFC anode", *J. Eur. Ceram. Soc.*, 30 (2010) 3415-3423.
- [69] U.P. Muecke, K. Akiba, A. Infortuna, T. Salkus, N.V. Stus, L.J. Gauckler, "Electrochemical performance of nanocrystalline nickel/gadolinia-doped ceria thin film anodes for solid oxide fuel cells", *Solid State Ionics*, 178 (2008) 1762-1768.

- [70] U.P. Muecke, S. Graf, U. Rhyner, L.J. Gauckler, "Microstructure and electrical conductivity of nanocrystalline nickel- and nickel oxide/gadolinia-doped ceria thin films", *Acta Mater.*, 56 (2008) 677-687.
- [71] A. Infortuna, A.S. Harvey, U.P. Muecke, L.J. Gauckler, "Nanoporous Ni-Ce<sub>0.8</sub>Gd<sub>0.2</sub>O<sub>1.9-x</sub> thin film cermet SOFC anodes prepared by pulsed laser deposition", *Phys. Chem. Chem. Phys.*, 11 (2009) 3663-3670.
- [72] G.J. La O, J. Hertz, H. Tuller, Y. Shao-Horn, "Microstructural. features of RF-sputtered SOFC anode and electrolyte materials", *J. Electroceram.*, 13 (2004) 691-695.
- [73] J.L. Hertz, H.L. Tuller, "Nanocomposite platinum-yttria stabilized zirconia electrode and implications for Micro-SOFC operation", *J. Electrochem. Soc.*, 154 (2007) B413-B418.
- [74] H. Timmermann, D. Fouquet, A. Weber, E. Ivers-Tiffée, U. Hennings, R. Reimert, "Internal reforming of methane at Ni/YSZ and Ni/CGO SOFC cermet anodes", *Fuel Cells*, 6 (2006) 307-313.
- [75] V.V. Kharton, F.M.B. Marques, A. Atkinson, "Transport properties of solid oxide electrolyte ceramics: a brief review", *Solid State Ionics*, 174 (2004) 135-149.
- [76] W.Z. Zhu, S.C. Deevi, "A review on the status of anode materials for solid oxide fuel cells", *Mat. Sci. Eng. a-Struct.*, 362 (2003) 228-239.
- [77] D.J.L. Brett, A. Atkinson, D. Cumming, E. Ramirez-Cabrera, R. Rudkin, N.P. Brandon, "Methanol as a direct fuel in intermediate temperature (500-600 degrees C) solid oxide fuel cells with copper based anodes", *Chem. Eng. Sci.*, 60 (2005) 5649-5662.
- [78] B.K. Lai, A.C. Johnson, M. Tsuchiya, S. Ramanathan, "Towards wafer-scale fabrication and 3-D integration of micro-solid oxide fuel cells for portable energy", *Proc. SPIE*, 7679 (2010).
- [79] E. Traversa, "Toward the miniaturization of solid oxide fuel cells ", *Electrochem. Soc. Interface*, 18 (2009) 4.

- [80] A. Bieberle-Hutter, D. Beckel, A. Infortuna, U.P. Muecke, J.L.M. Rupp, L.J. Gauckler, S. Rey-Mermet, P. Muralt, N.R. Bieri, N. Hotz, M.J. Stutz, D. Poulikakos, P. Heeb, P. Muller, A. Bernard, R. Gmur, T. Hocker, "A micro-solid oxide fuel cell system as battery replacement", *J. Power Sources*, 177 (2008) 123-130.
- [81] T. Ryll, H. Galinski, L. Schlagenhauf, P. Elser, J.L.M. Rupp, A. Bieberle-Hutter, L.J. Gauckler, "Microscopic and nanoscopic three-phase-boundaries of platinum thin-film electrodes on YSZ electrolyte", *Adv. Func. Mat.*, 21 (2011) 565-572.
- [82] H. Seidel, L. Csepregi, A. Heuberger, H. Baumgartel, "Anisotropic etching of crystalline silicon in alkaline-solutions. 1. Orientation dependence and behavior of passivation layers", *J. Electrochem. Soc.*, 137 (1990) 3612-3626.
- [83] M. Mogensen, S. Primdahl, M.J. Jorgensen, C. Bagger, "Composite electrodes in solid oxide fuel cells and similar solid state devices", *J. Electroceram.*, 5 (2000) 141-152.
- [84] N. Shikazono, D. Kanno, K. Matsuzaki, H. Teshima, S. Sumino, N. Kasagi, "Numerical assessment of SOFC anode polarization based on three-dimensional model microstructure reconstructed from FIB-SEM images", *J. Electrochem. Soc.*, 157 (2010) B665-B672.
- [85] A.C. Johnson, B.K. Lai, H. Xiong, S. Ramanathan, "An experimental investigation into micro-fabricated solid oxide fuel cells with ultra-thin  $\text{La}_{0.6}\text{Sr}_{0.4}\text{Co}_{0.8}\text{Fe}_{0.2}\text{O}_3$  cathodes and yttria-doped zirconia electrolyte films", *J. Power Sources*, 186 (2009) 252-260.
- [86] J. Daillant, A. Gibaud, in: *X-ray and Neutron Reflectivity: Principles and Applications*, Springer, 1999.
- [87] Y. Takagi, K. Kerman, C. Ko, S. Ramanathan, "Operational characteristics of thin film solid oxide fuel cells with ruthenium anode in natural gas", *J. Power Sources*, 243 (2013) 1-9.
- [88] K. Kerman, T. Tallinen, S. Ramanathan, L. Mahadevan, "Elastic configurations of self-supported oxide membranes for fuel cells", *J. Power Sources*, 222 (2013) 359-366.

- [89] B.K. Lai, K. Kerman, S. Ramanathan, "Nanostructured  $\text{La}_{0.6}\text{Sr}_{0.4}\text{Co}_{0.8}\text{Fe}_{0.2}\text{O}_3/\text{Y}_{0.08}\text{Zr}_{0.92}\text{O}_{1.96}/\text{La}_{0.6}\text{Sr}_{0.4}\text{Co}_{0.8}\text{Fe}_{0.2}\text{O}_3$  (LSCF/YSZ/LSCF) symmetric thin film solid oxide fuel cells", *J. Power Sources*, 196 (2011) 1826-1832.
- [90] A. Bonakdarpour, M.D. Fleischauer, M.J. Brett, J.R. Dahn, "Columnar support structures for oxygen reduction electrocatalysts prepared by glancing angle deposition", *Appl. Catal. a-Gen.*, 349 (2008) 110-115.
- [91] V. Matolin, I. Matolinova, M. Vaclavu, I. Khalakhan, M. Vorokhta, R. Fiala, I. Pis, Z. Sofer, J. Poltiero-va-Vejpravova, T. Mori, V. Potin, H. Yoshikawa, S. Ueda, K. Kobayashi, "Platinum-doped  $\text{CeO}_2$  thin film catalysts prepared by magnetron sputtering", *Langmuir*, 26 (2010) 12824-12831.
- [92] K. Robbie, G. Beydaghyan, T. Brown, C. Dean, J. Adams, C. Buzea, "Ultrahigh vacuum glancing angle deposition system for thin films with controlled three-dimensional nanoscale structure", *Rev. Sci. Instrum.*, 75 (2004) 1089-1097.
- [93] D.W. Goodman, J.M. White, "Measurement of active-carbon on ruthenium(110) - relevance to catalytic methanation", *Surf. Sci.*, 90 (1979) 201-203.
- [94] M.J. Vanstaden, J.P. Roux, "The superposition of carbon and ruthenium Auger-spectra", *Appl. Surf. Sci.*, 44 (1990) 259-262.
- [95] X.H. Wang, H. Huang, T. Holme, X. Tian, F.B. Prinz, "Thermal stabilities of nanoporous metallic electrodes at elevated temperatures", *J. Power Sources*, 175 (2008) 75-81.
- [96] J.P. Ye, C.V. Thompson, "Anisotropic edge retraction and hole growth during solid-state dewetting of single crystal nickel thin films", *Acta Mater.*, 59 (2011) 582-589.
- [97] S. Horch, H.T. Lorenzen, S. Helveg, E. Laegsgaard, I. Stensgaard, K.W. Jacobsen, J.K. Nørskov, F. Besenbacher, "Enhancement of surface self-diffusion of platinum atoms by adsorbed hydrogen", *Nature*, 398 (1999) 134-136.

- [98] G.L. Kellogg, "Hydrogen promotion of surface self-diffusion on Rh(100) and Rh(311)", *Phys. Rev. B*, 55 (1997) 7206-7212.
- [99] A. Evans, M. Prestat, R. Tölke, M.V.F. Schlupp, L.J. Gauckler, Y. Safa, T. Hocker, J. Courbat, D. Briand, N.F. de Rooij, D. Courty, "Residual stress and buckling patterns of free-standing yttria-stabilized-zirconia membranes fabricated by pulsed laser deposition", *Fuel Cells*, 12 (2012) 614-623.
- [100] B. Kimmerle, A. Baiker, J.D. Grunwaldt, "Oscillatory behaviour of catalytic properties, structure and temperature during the catalytic partial oxidation of methane on Pd/Al<sub>2</sub>O<sub>3</sub>", *Phys. Chem. Chem. Phys.*, 12 (2010) 2288-2291.
- [101] Y.J. Kim, Y. Gao, S.A. Chambers, "Core-level X-ray photoelectron spectra and X-ray photoelectron diffraction of RuO<sub>2</sub>(110) grown by molecular beam epitaxy on TiO<sub>2</sub>(110)", *Appl. Surf. Sci.*, 120 (1997) 250-260.
- [102] L. Atanasoska, W.E. Ogrady, R.T. Atanasoski, F.H. Pollak, "The surface-structure of RuO<sub>2</sub> - a LEED, Auger and XPS study of the (110) and (100) faces", *Surf. Sci.*, 202 (1988) 142-166.
- [103] R. Schafranek, J. Schaffner, A. Klein, "In situ photoelectron study of the (Ba,Sr)TiO<sub>3</sub>/RuO<sub>2</sub> contact formation", *J. Eur. Ceram. Soc.*, 30 (2010) 187-192.
- [104] D. Rochefort, P. Dabo, D. Guay, P.M.A. Sherwood, "XPS investigations of thermally prepared RuO<sub>2</sub> electrodes in reductive conditions", *Electrochim. Acta*, 48 (2003) 4245-4252.
- [105] S. Doniach, M. Sunjic, "Many-electron singularity in X-ray photoemission and X-ray line spectra from metals", *Journal of Physics Part C: Solid State Physics*, 3 (1970) 285-291.
- [106] P. Van der Heide, "X-ray Photoelectron Spectroscopy - An Introduction to Principles and Practices", John Wiley & Sons, Inc., New Jersey, 2012.

- [107] A. Foelske, O. Barbieri, M. Hahn, R. Kotz, "An X-ray photoelectron spectroscopy study of hydrous ruthenium oxide powders with various water contents for supercapacitors", *Electrochem. Solid-State Lett.*, 9 (2006) A268-A272.
- [108] C. Mun, J. Ehrhardt, J. Lambert, C. Madic, "XPS investigations of ruthenium deposited onto representative inner surfaces of nuclear reactor containment buildings", *Appl. Surf. Sci.*, 253 (2007) 7613-7621.
- [109] W.E. Ogrady, L. Atanasoska, F.H. Pollak, H.L. Park, "Single-crystal RuO<sub>2</sub> (110) - surface-structure", *J. Electroanal. Chem.*, 178 (1984) 61-68.
- [110] S.P. Sharma, L.L. Hines, "Oxidation of ruthenium", *IEEE Transactions on Components Hybrids and Manufacturing Technology*, 6 (1983) 89-92.
- [111] J.Y. Shen, A. Adnot, S. Kaliaguine, "An ESCA study of the interaction of oxygen with the surface of ruthenium", *Appl. Surf. Sci.*, 51 (1991) 47-60.
- [112] R. O'Hayre, S.W. Cha, W. Colella, F.B. Prinz, in: *Fuel Cell Fundamentals*, Wiley, 2009.
- [113] Z. Cheng, J.H. Wang, Y.M. Choi, L. Yang, M.C. Lin, M.L. Liu, "From Ni-YSZ to sulfur-tolerant anode materials for SOFCs: electrochemical behavior, in situ characterization, modeling, and future perspectives", *Energy Environ. Sci.*, 4 (2011) 4380-4409.
- [114] M. Wang, W. Weng, H. Zheng, X. Yi, C. Huang, H. Wan, "Oscillations during partial oxidation of methane to synthesis gas over Ru/Al<sub>2</sub>O<sub>3</sub> catalyst", *J. Natural Gas Chem.*, 18 (2009) 300-305.
- [115] T. Yoshizumi, S. Taniguchi, Y. Shiratori, K. Sasaki, "Sulfur poisoning of SOFCs: Voltage oscillation and Ni oxidation", *J. Electrochem. Soc.*, 159 (2012) F693-F701.
- [116] T. Tsai, S.A. Barnett, "Sputter-deposition of cermet fuel electrodes for solid oxide fuel-cells", *J. Vac. Sci. Technol. A*, 13 (1995) 1073-1077.

[117] P. Sotta, D. Long, "The crossover from 2D to 3D percolation: Theory and numerical simulations", *Eur. Phys. J. E*, 11 (2003) 375-387.

[118] J.H. Xu, T. Jarlborg, A.J. Freeman, "Self-consistent band-structure of the rutile dioxides NbO<sub>2</sub>, RuO<sub>2</sub>, and IrO<sub>2</sub>", *Phys. Rev. B*, 40 (1989) 7939-7947.

[119] J.D. Baek, C.C. Yu, P.C. Su, "A silicon-based nanothin film solid oxide fuel cell array with edge reinforced support for enhanced thermal mechanical stability", *Nano Lett.*, 16 (2016), 2413-2417.

[120] W.C. Jung, J.J. Kim, H.L. Tuller, "Investigation of nanoporous platinum thin films fabricated by reactive sputtering: Application as micro-SOFC electrode", *J. Power Sources*, 275 (2015), 860-865.

## **Acknowledgements**

The author would like to thank Professor Naoki Shikazono for supervising the process of preparing this doctoral dissertation, and for a financial support on TEM cross-section analyses.

The author is grateful to Professor Shriram Ramanathan for the support and supervision on the research direction during the research project at Harvard University School of Engineering and Applied Sciences.

The author would also like to thank Professor Harumi Yokokawa, Professor Yuji Suzuki, Professor Ryuji Kikuchi, and Professor Keisuke Nagato for their advice and guidance through the qualification process and at the thesis defense.

The author appreciates Dr. Lai, Dr. VanOvermeere, and Dr. Kerman's support on experimental methodologies and fruitful discussions at Harvard University.

The author would like to acknowledge SONY Corporation for a financial support on micro-SOFC research project at Harvard University.